

UNIVERSITY OF TECHNOLOGY SYDNEY
Faculty of Engineering and Information Technology

**Measurement, Modelling and State Estimation
Techniques for Lithium-ion batteries**

by

Qi Yao

A THESIS SUBMITTED
IN PARTIAL FULFILLMENT OF THE
REQUIREMENTS FOR THE DEGREE

Doctor of Philosophy

Sydney, Australia

2021

Certificate of Authorship/Originality

I, Qi Yao, declare that this thesis, is submitted in fulfilment of the requirements for the award of Doctor of Philosophy in the Faculty of Engineering and Information Technology at the University of Technology Sydney.

This thesis is wholly my own work unless otherwise referenced or acknowledged. In addition, I certify that all information sources and literature used are indicated in the thesis.

This document has not been submitted for qualifications at any other academic institution.

This research is supported by the Australian Government Research Training Program.

Production Note:

Signature: Qi Yao Signature removed prior to publication.

Date: 27/02/2021

Dedication

My Uncle, Chengjin Yao

Acknowledgements

First, I would like to express my gratitude to my supervisor, Professor Dylan Dah-Chuan Lu, for providing tremendous support and encouragement throughout these years. I appreciate for his mentoring and cultivating for my research work and my research habits that he told me no matter how we focus on current research work, it is important to keep reading latest papers. His persistent interest in research inspire me a lot. I convey my gratitude to my co-supervisor, Dr. Gang Lei, for his help and advises during this research.

I am grateful for all my colleagues and teammates in Dylan's Group. I feel so lucky to met Tian Cheng and Kaixin Wei that we share lots of happiness together. In particular, Tian Cheng is my colleague, my roommate and my friend. Moreover, it is important to express my thanks to Yang He, who provides me lots of help.

I want to express my appreciation to my parents and my grandmother, who give me endless love, help, and encouragement in my life. You always try to solve difficulties before I know them. How lucky to be your child.

Finally, I want to dedicate my most sincere miss and thanks to my uncle, Chengjin Yao, who passed away in 2018. During my study and growth, he has always given me selfless help, love and unreserved support. He is a reliable and heartwarming person, who respects his parents, loves his wife, and cares for younger generations in our family. One of my biggest regrets in my life is that I don't have a chance to share all my happiness and sadness in my PhD journey with him. Dear uncle, I hope you live happily in another world without suffering.

Qi Yao

Sydney, Australia, 2021.

List of Publications

Accepted Journal Papers

- J-1. **Q. Yao**, D. D. -C. Lu and G. Lei, "Rapid Open-Circuit Voltage Measurement Method for Lithium-ion Batteries Using One-cycle Bipolar-current Pulse," in IEEE Journal of Emerging and Selected Topics in Industrial Electronics, doi: 10.1109/JESTIE.2020.3041711.
- J-2. **Q. Yao**, D. D. -C. Lu and G. Lei, "Accurate Online Battery Impedance Measurement Method with Low Output Ripples on Power Converters," in Energies, doi: <https://doi.org/10.3390/en14041064>

Accepted Conference Papers

- C-1. **Q. Yao**, D. Lu and G. Lei, "Battery Impedance Measurement Using Fast Square Current Perturbation," 2019 IEEE 4th International Future Energy Electronics Conference (IFEEEC), Singapore, 2019, pp. 1-5.
- C-2. **Q. Yao**, D. D. Lu and G. Lei, "A Simple Internal Resistance Estimation Method Based on Open Circuit Voltage Test Under Different Temperature Conditions," 2018 IEEE International Power Electronics and Application Conference and Exposition (PEAC), Shenzhen, 2018, pp. 1-4.

Under Process Journal Papers

- J-3. **Q. Yao**, D. D. -C. Lu and G. Lei, "A Sensorless Temperature Estimation Method For Lithium-ion Battery Using Recurrent Neural Network With Gated Recurrent Unit"
- J-4. **Q. Yao**, D. D. -C. Lu and G. Lei, " An Empirical Comparison of Different Recurrent Neural Networks for Battery State of Charge Estimation

Contents

Certificate	ii
Dedication	iii
Acknowledgments	iv
List of Publications	v
List of Figures	xi
List of Tables	xv
Abbreviation	xvi
Abstract	xviii
1 Introduction	1
1.1 Background	1
1.2 Introduction of Lithium-ion Batteries	4
1.2.1 Working Principle	4
1.2.2 Different Types of Lithium-ion Batteries	5
1.2.3 Models	5
1.2.3.1 Equivalent electric circuit models	6
1.2.3.2 Physics-based electrochemical models	7
1.2.3.3 Data-driven models	9
1.3 Introduction of Battery Management of System	9
1.3.1 Signal Measurement	10
1.3.2 States Estimation	11

1.3.2.1	State of Charge (SOC)	11
1.3.2.2	State of Health (SOH)	11
1.3.3	Balancing	12
1.4	Research Objectives	13
1.5	Thesis Organization	14
2	A Rapid OCV Measurement Method for Battery Modelling	16
2.1	Introduction	16
2.2	Related Works and Research Gap	17
2.3	Proposed Rapid OCV Measurement Method Using OCBCP	20
2.3.1	Physical Description of the Battery Model	22
2.3.2	Second-Order Relaxation Model Analysis	24
2.3.3	Experimental Setup	26
2.3.3.1	Experimental Platform	26
2.3.3.2	Battery Information	27
2.3.3.3	Battery Relaxation Test	27
2.3.4	OCBCP based OCV acceleration measurement method	28
2.3.4.1	Battery Relaxation Model Parameters Identification	30
2.3.4.2	OCBCP Acceleration Method	33
2.3.4.3	Improved Current Pulses Considering Hysteresis Voltage	36
2.4	Discussion of Results	38
2.4.1	Verifying the Experiment Procedure	38
2.4.2	Validation Results	39

2.4.2.1	Validation Results at Incremental OCV Tests	39
2.4.2.2	Validation Results at Dynamic Conditions	43
2.5	Summary	43
3	Battery Impedance Measurement Method	46
3.1	Introduction	46
3.2	EIS Measurement Techniques	46
3.2.1	Single-Frequency Measurement	47
3.2.2	Multi-Frequency Measurement	48
3.3	Related Works and Research Gap	48
3.4	Review of Converter Normal Operation	51
3.5	Review Converter-Based Duty-Cycle Perturbation Battery Impedance Measurement Method	52
3.6	Proposed Switched Resistor Circuit Perturbation Method for Output Voltage Ripples Reduction	54
3.6.1	Principle of the SRC Perturbation Method	54
3.6.2	SRC Parameter Selection	55
3.6.3	Theoretical Verification of Output Voltage Ripple Reduction in Proposed SRC Perturbation Method	56
3.6.4	Simulation Verification of Output Voltage Ripple Reduction in Proposed SRC Perturbation Method	60
3.6.5	Experimental Verification of Output Voltage Ripples Reduction in Proposed SRC Method	65
3.7	Battery Impedance Measurement Validation	66
3.7.1	Battery Multi-frequencies Impedance Calculation Algorithm .	66

3.7.2	Online Battery Impedance Test at 50% SOC, 1C Discharge Current Rate	68
3.7.3	Online Battery Impedance Tests at Various Battery SOC . . .	71
3.7.4	Online Battery Impedance Tests at Various Discharge Current Rate	71
3.8	Summary	72
4	Sensorless Battery Surface Temperature Estimation	73
4.1	Introduction	73
4.1.1	Related Works and Research Gap	74
4.2	Battery Temperature Distribution is a Time-Sequence Task (Theoretical Analysis)	75
4.3	Proposed GRU-RNN Sensorless Battery Temperature Estimation Method	77
4.4	Experiment and Result Discussion	80
4.4.1	Platform for Data Collection	80
4.4.2	Data Preparation and Experimental Procedure	81
4.4.3	Experiment: GRU-RNN Model Training and Evaluation . . .	81
4.4.4	Experimental Result Discussion	84
4.5	Summary	84
5	Recurrent neural network based online SOC estimation	87
5.1	Introduction	87
5.1.1	Related Works for RNN-based SOC Estimation	88
5.2	Models	90
5.2.1	Traditional RNN	90

5.2.2	LSTM-RNN	92
5.2.3	GRU-RNN	94
5.2.4	Bidirectional RNN	95
5.3	Experimental Setup	96
5.3.1	Experimental Platform	96
5.3.2	Experimental Data	97
5.3.3	Experimental Procedure	98
5.4	Experimental Results and Discussion	100
5.4.1	Different Numbers of The Hidden Nodes	100
5.4.2	Different Numbers of The Layers	104
5.4.3	Different Numbers of Mini-Batch	104
5.4.4	Result Discussion	104
5.5	Summary	105
6	Conclusion	106
6.1	Conclusion	106
6.2	Future Work	108
	Bibliography	110

List of Figures

1.1	Global greenhouse gas emissions [1]	2
1.2	EV sale data (x axis: year, y axis: sale number (million)) [2]	3
1.3	Schematic of P2D model and SP model [3]	8
1.4	Illustration of data driven model procedure	9
1.5	Key functions of the BMS	10
1.6	Energy and capacity loss of the lithium-ion batteries under imbalance	12
1.7	Battery balancing methods [4]	13
2.1	Online SOC estimation process, problem of the conventional incremental OCV test method and the contribution of this work. . . .	21
2.2	The second-order battery model. (a) The operation mode model when the switch is on; (b) The relaxation model model when the switch is off.	23
2.3	Battery experimental platform.	27
2.4	Terminal voltage during discharging by 12 mins under C/2 and measured open circuit voltage after stopping discharge for different times. (a) After 2 hour; (b) After 8 hour.	29
2.5	Polarization voltage variations with time.	30
2.6	The relationship between current pulse amplitude and duration of the polarization voltage zero-crossing point.	31

2.7	The measured terminal voltage of battery by discharging 10% SOC followed by the calculated one-cycle bipolar-current pulse (1C,880s). . .	33
2.8	Comparison of the polarization voltage curves after the proposed three sets of OCBCPs and the reference. (a) The measured voltage; (b) The polarization voltage (measured voltage minus the OCV). . .	37
2.9	Comparisons of polarization voltage curves of INR-18650 battery between the conventional incremental OCV method and the rapid OCV method under different settings.	41
2.10	Comparisons of polarization voltage curves of NRC-18650 battery between the conventional incremental OCV method and the rapid OCV method under different settings.	42
2.11	Comparison of the conventional OCV performance (reaches to OCV at 1800s) and rapid OCV method performance (reaches OCV at 1100s) after the same dynamic current profile	44
3.1	EIS acquired at healthy and weak batteries [5]	47
3.2	Illustration diagrams for battery impedance measurement methods: conventional duty-cycle perturbation method [6] (left), the proposed SRC perturbation method (right)	53
3.3	Small-signal model of boost converter operating in CCM (Reproduced with permission from [7],IEEE, 2019)	57
3.4	(a) Step response of $v_{o,ac}$ due to $\frac{d_{ac}}{2}=0.02$ (b) Step response of $v_{o,ac}$ due to $v_{B,ac}=0.015$	62
3.5	(a) Waveforms of converter under normal power delivery mode (no perturbation) (b) Waveforms of the converter under impedance measurement mode with duty-cycle perturbation (c) Waveforms of the converter under impedance measurement mode with the proposed SRC perturbation method.	63

3.6	Experimental bench.	65
3.7	The experimental waveforms of the proposed SRC perturbation method.	65
3.8	Online battery impedance under 50% SOC, 1C discharge current rate.	68
3.9	Online battery impedance results (50Hz to 500Hz) under different SOC values (a) under 1C, 20% SOC (b) under 1C, 30% SOC (c) under 1C, 50% SOC.	69
3.10	Online battery impedance results (50Hz to 500Hz) under different discharge current rates (a) under 0.5C, 50% SOC (b) under 1C, 50% SOC (c) under 1.5C, 50% SOC.	70
4.1	Conventional battery surface measurement method (left), which has four sensors: voltage sensor, current sensor, battery surface temperature sensor, and ambient temperature sensor; the proposed sensorless surface temperature estimation method (right), which only has three sensors: voltage sensor, current sensor, and ambient temperature sensor	76
4.2	(a) Battery equivalent electric model. (b) Battery equivalent thermal model.	77
4.3	Illustration diagram of GRU-RNN principle: x is the input vector, GRU is the GRU cell, h is the hidden state, and y is the output vector	78
4.4	(a) GRU cell structure. (b) Overall structure of the proposed GRU-RNN model	79
4.5	Experimental procedure for GRU-RNN model training and temperature estimation.	80

4.6	Temperature estimation with GRU-RNN under different different loading profiles and temperature from: (a) US06 at -10°C ; (b) US06 at 25°C ; (c) US06 at 50°C ; (d) FUDS at -10°C ; (d) FUDS at 25°C ; (f) FUDS at 50°C	86
5.1	(a)Illustration diagram of RNN working principle; (b) Traditional RNN cell.	91
5.2	LSTM cell structure	92
5.3	GRU cell structure	94
5.4	Internal structure of BiRNN	96
5.5	FUDS drive cycle recorded at 45°C . The data are shown from the top to bottom: current, terminal voltage and SOC.	98

List of Tables

1.1	Several commercial EVs and employed lithium-ion batteries	6
1.2	The list of different ECMs	7
2.1	Specifications of the batteries in the experiment	27
2.2	Battery Identification Results (OCV from 3.662V to 3.619V)	32
2.3	Relaxation Time Comparison	44
3.1	Parameters of the theoretical analysis and simulation for ripple analysis	59
3.2	Battery perturbation signals and output voltage ripples comparison .	64
3.3	Main Specification of the Experimental Prototype	66
4.1	Hyperparameter setting.	83
4.2	Temperature estimation results with the proposed GRU-RNN and FNN	85
5.1	Specifications of the batteries in the experiment	97
5.2	Comparison results using different numbers of hidden nodes	102
5.3	Comparison results using different numbers of layers	102
5.4	Comparison results using different numbers of mini-batch	103

Abbreviation

BMS - Battery Storage System

EV - Electric Vehicle

BMS - Battery Management System

SOC - State of Charge

SOH - State of Health

LMO - LiMn_2O_4

NCM - $\text{LiCo}_x\text{Ni}_y\text{Mn}_z\text{O}_2$

NCA - $\text{LiNi}_{0.8}\text{Co}_{0.15}\text{Al}_{0.05}\text{O}_2$

LFP - LiFePO_4

ECM - Electric Circuit Model

RC - Resistor Capacitor

OCV - Open Circuit Voltage

RNN - Recurrent Neural Network

AI - Artificial Intelligence

EIS - Electrochemical Impedance Spectroscopy

RMSE - Root Means Square Error

MAE - Mean Absolute Error

PDE - Partial Differential Equations

P2D - Pseudo-Two-Dimensional

SPM - Single Particle Model

OCBCP - One Cycle Biopolar Current Pulse

SRC - Switched Resistor Circuit

ESR - Equivalent Series Resistance

DC - Direct Current

AC - Alternating Current

DAQ - Data Acquisition

DTF - Discrete-time Fourier transform

PWM -Pulse Width Modulation

CCM -Continuous Conduction Mode

FNN - Feedforward Neural Network

AHC - Ampere Hour Counting

DD - Data Driven

MB - Model-Based

LSTM - Long Short-Term Memory

GRU - Gated Recurrent Unit

BiRNN - Bidirectional Recurrent Neural Network

LSTM-RNN - Long Short-Term Memory Recurrent Neural Network

GRU-RNN - Gated Recurrent Unit Recurrent Neural Network

BiLSTM-RNN - Bidirectional Long Short-Term Memory Recurrent Neural Network

ABSTRACT

Measurement, Modelling and State Estimation Techniques for Lithium-ion batteries

by

Qi Yao

Lithium-ion batteries have been widely adopted in energy storage systems for electric vehicles (EVs), electric portable devices, smart grid, and renewable energy systems because of their high energy density, long lifetime, and low self-release rate. When lithium-ion batteries are used in real applications such as EVs, they normally work with power converters, which can deliver power from the batteries to the load and regulate the system output voltage. However, Lithium-ions batteries also have a critical safety concern. As chemical products, the battery states such as state of charge (SOC) cannot be directly measured by sensors; the only directly measurable signals of lithium-ion batteries during battery operation are terminal voltage, operational current and temperature. Some models have been established to calculate information of the battery states using measured signals. However, the inherent chemical characteristics of lithium-ion batteries mean that it is difficult to achieve a highly accurate online battery state monitoring or estimation. When the battery state is estimated inaccurately, it will waste the available capacities, reduce battery lifetime, and could even lead to fire or explosion. To avoid these issues, lithium-ion batteries should be well-monitored and managed by a battery management system (BMS).

This thesis focuses on improving the efficiency, reliability and estimation accuracy for the BMS of lithium-ion batteries from signals measurement, battery modelling and state estimation perspectives. First, this thesis develops an improved battery modelling techniques by proposing a rapid and accurate open circuit volt-

age (OCV) measurement method. Second, this thesis develops practical battery impedance measurement techniques, which can be used for offline battery modelling and online states monitoring. Third, a sensorless battery surface temperature estimation has been proposed to improve the reliability and reduce the cost of the BMS. Fourth, as artificial intelligence (AI) technology has developed, more recurrent neural network (RNN) based battery SOC estimation methods have been proposed. This thesis comprehensively evaluates previous methods from theoretical and experimental perspectives and proposes a RNN model with suitable hyper-parameter setting for online SOC estimation with high accuracy and low computational burden.

Chapter 1

Introduction

1.1 Background

Since the start of the industrial revolution, the greenhouse gas emissions, primarily from the combustion of the fossil energy, have dramatically increased. In order to solve the greenhouse effect and pollution crisis, around 200 countries have signed the Paris Climate Agreement, which set created an ambitious global plan to fight with the temperature rise and climate change. The United States, China, and the European Union, which are the three largest emitters of the greenhouse gases, have set their goals for achieving net zero emissions by the middle of the century [8]. Global greenhouse gas emissions can be categorised by human activities [1], which are from electricity, heat, and transportation, as shown in Figure 1.1.

As shown in Figure 1.1, 25% of the greenhouse gas emissions are generated by electricity/heat production due to the coal or oil. These emissions can be dramatically reduced with the development of renewable and clean energy such as solar and wind. Transportation is responsible for 14% of greenhouse gas emissions from traditional internal combustion engine based vehicles. Facing the transportation emission challenge, electric vehicles (EVs) can be a potential solution. To solve these two problems, renewable energy and EV are being developed with the effort from governments, industry and academia. Australia is a world leader in renewable energy sources, based on the fact that renewable energy accounted for 24% of Australia's total electricity generation in 2019 [9]. One important point that should be noted is that solar energy accounts for more than 30% of clean energy. Since solar

Global Greenhouse Gas Emissions by Economic Sector

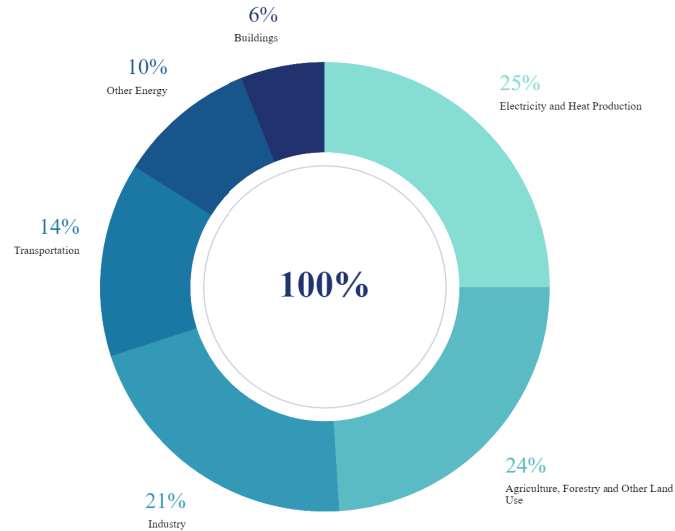


Figure 1.1 : Global greenhouse gas emissions [1]

is not a stable energy source, it cannot provide electricity without sunlight. Therefore, a battery storage system (BSS), which can store and deliver energy based on the requirements of the customers, plays an important role in the renewable energy field [2]. EVs have attracted increasing attention from customers and researchers, and the market for EVs is promising based on the fact that the sales of EVs climbed 2.1 million globally in 2019, exceeding those in 2018 to boost stock to 7.2 million [2], as shown in Figure 1.2. There is no doubt that the BSS is one of the most important components of EV. With the rapid growth in EV over the past decades, there are huge improvements in BSS both in the performance of batteries and the functions of battery management system (BMS).

Compared with other types of batteries such as lead acid batteries, nickel-metal hydride batteries, and nick-cadmium batteries [10], lithium-ion batteries have higher energy density, and higher power density. Therefore, lithium-ion batteries are widely

Global EV Sale Data

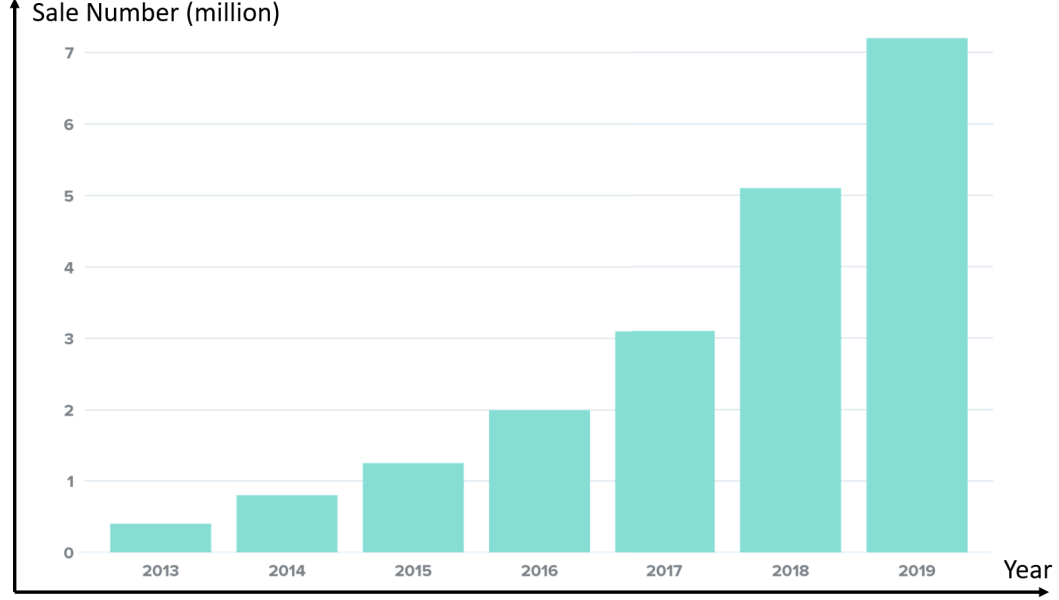


Figure 1.2 : EV sale data (x axis: year, y axis: sale number (million)) [2]

used in energy storage systems including electric vehicles, portable devices, and energy storage devices in micro-grid or renewable energy systems. Currently, most electric vehicles use lithium-ion batteries as their power source [11]. In addition, more than 90% of large-scale energy storage systems adopted lithium-ion batteries by the end of the 2017 [12].

In parallel with development of lithium-ion batteries, the performance of the BMS is also an important factor enabling these batteries to be widely adopted, because BMS ensure the safe, reliable and efficient battery pack operation.

The main technical obstacles restricting the application of lithium-ion batteries can be seen in the following three aspects: (1) the lithium-ion battery system is highly nonlinear and it is difficult to accurately model. (2) the inner states of the battery cannot be directly measured by physical sensors and the states are easily

influenced by external environment such as temperature. As the size of the BSS increases, it is even more difficult to accurately estimate the internal states. (3) the inconsistencies of the battery cells influence the efficiency of the pack, which increases the risk of the battery pack. Some safety measures are effective on small battery systems but ineffective on large-scale BSSs such as electric vehicles. Therefore, the BMS should be improved to solve the problems above[4,5].

In this chapter, lithium-ion batteries are introduced and reviewed from chemical materials, characteristics, and equivalent models, respectively. The BMS is reviewed from signal measurement, states estimation, and balancing methods perspectives.

1.2 Introduction of Lithium-ion Batteries

As one of the most important components of the present storage system, lithium-ion batteries have attracted much research interest. This section provides an introduction to the working principle, major types, and equivalent models of lithium-ion batteries.

1.2.1 Working Principle

The cylindric lithium-ion batteries consist of positive/negative electrodes, separators, and current collectors. The active materials in the positive and negative electrodes are porous, which allow the lithium ions to intercalate or deintercalate. Normally, in the positive electrode (anode), the active material consists of one or more metal oxides, and the negative electrode (cathode) contains graphite. During discharging, the lithium ions flow from the positive electrode to the negative electrode through the electrolyte and separator. Charging reverses the direction of discharge, and lithium ions flow from the negative electrode to the positive electrode [13].

During continuous charging or discharging, lithium ion diffusion occurs, and this

will result in the concentration gradient of the battery. The concentration gradient is the root for the energy storage of a battery because the free energy of lithium ions is higher in the negative electrode as compared with the the positive electrode [14]. For any given material in the electrode, the free energy is decided by its electric potential [14]. The difference of the electric potentials between two electrodes is the terminal voltage. Once the battery is fully relaxed after charging or discharging, the terminal voltage is referred to the open circuit voltage, which has a correlation with the state of charge of the battery.

1.2.2 Different Types of Lithium-ion Batteries

The main differences among the types of lithium-ion batteries are the material of the positive electrode. Although the overall operational voltage of these batteries is 1.5-4.2V, the different materials determine that their operational voltage range are slightly different. For example, the operational voltage range of graphite/LiMn₂O₄ (C/LMO) batteries, graphite/LiCo_xNi_yMn_zO₂ (C/NCM) batteries, and graphite/LiNi_{0.8}Co_{0.15}Al_{0.05}O₂ (C/NCA) batteries are 2.5-4.2V. The operational voltage range of graphite/LiFePO₄ (C/LFP) batteries is 2.0-3.7V. Moreover, different electrode materials have their advantages and disadvantages. For example, NCA has higher power and energy density but also have a higher risk. LFP has a lower energy density and lower nominal voltage but is safer. Different types of lithium-ion batteries are adopted in commercial EVs. Some of the current commercial EVs and the batteries they use are listed in Table 1.1.

1.2.3 Models

Since the lithium-ion batteries are chemical products which have some inner states that cannot be directly measured by physical sensors, it is important to build an accurate model using available signals to estimate the inner states so as to ensure a safe and efficient operation. The battery models presented in chapter mainly cat-

Table 1.1 : Several commercial EVs and employed lithium-ion batteries

EV Brand	Battery Company	Positive Electrode	Negative Electrode
Tesla Roadster	Panasonic	NCA	Graphite
BYD E6	BYD	LFP	Graphite
Nissan Leaf EV	Nissian	LMO	Graphite
BWM iX3	CATL	NCM	Graphite

egorised into the following three types: the electrical equivalent circuit models [15], the physics-based electrochemical models [16], and the data-driven models established by artificial intelligence algorithms [17].

1.2.3.1 *Equivalent electric circuit models*

Equivalent electric circuit models (ECMs) normally consist of a voltage source corresponding to SOC, a resistor representing the instantaneous polarization effect, one or more resistor-capacitor (RC) pair(s) which can be used to describe the non-instantaneous polarization effect of the battery [18–20]. These electric components can be combined into different structures, which can be summarized as three common models: *Rint* model, *Thevenin* model, and Partnership for a New Generation of Vehicles (PNGV) model, as shown in Table 1.2.

From Table 1.2, it can be observed that these three ECMs have an inner expanding relationship. Compared with the *Rint* model, the *Thevenin* model can capture the dynamic or non-instantaneous characteristics of the battery due to the RC pair [21]. Moreover, the PNGV model has an original *Thevenin* model and a bulk capacitor, which is used to describe the OCV variation by accumulating the discharge current [20]. The accuracy of the ECMs can be further improved from different perspectives. For example, a physical ECM is proposed by having the War-

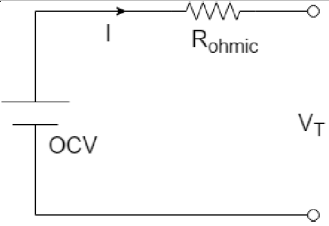
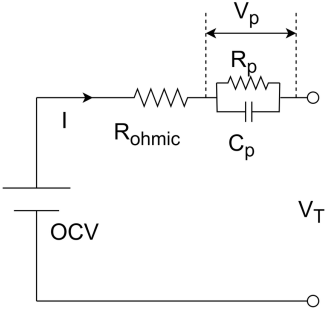
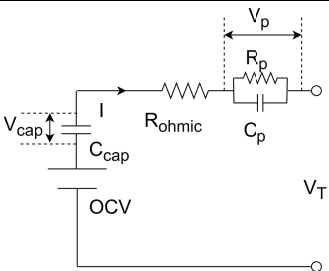
Model	Explanation
	<p><i>Rint</i> Model [15]; $V_T = OCV - I \cdot R_{ohmic}$; R_{ohmic} is the ohmic resistor, OCV is the open circuit voltage (OCV), V_T is the terminal voltage, I is the operational current</p>
	<p><i>Thevenin</i> Model [19]; $V_T = OCV - V_p - I \cdot R_{ohmic}$; R_p and C_p are used to represent the polarization effect, V_p is the voltage across the RC pair. The first order RC model is the simplest structure with a light computation burden, more RC pairs can be added to achieve a high modelling accuracy.</p>
	<p>PNGV model [20]; $V_T = OCV - V_{cap} - V_p - I \cdot R_{ohmic}$; C_{cap} is the bulk capacitance, V_{cap} is the voltage across bulk capacitor</p>

Table 1.2 : The list of different ECMs

bug element, which can be obtained by Electrochemical Impedance Spectroscopy (EIS) measurement [22–24]. Normally, the EIS is measured offline by commercial equipment. Currently, there are some studies that proposed several online battery impedance measurement methods [25, 26].

1.2.3.2 Physics-based electrochemical models

Physics-based electrochemical models are the most accurate because they can clearly explain batteries' key behaviours at the microscopic level, based on the reactions of the battery. These type of models are developed through a series of

physical laws: Ohm's law, Farady's law, Fick's law of diffusion, and the Butler-Volmer equation [16]. The physics-based electrochemical models normally consist of a group of nonlinear Partial Differential Equations (PDEs). Although this type of models are accurate from the modelling perspective, it is hard to directly apply physics-based electrochemical models for real applications such as EVs due to its heavy computation burden [27]. Therefore, some studies have focused on how to simplify the physics-based electrochemical models. Two typical example models are introduced below: the pseudo-two-Dimensional (P2D) model and the Single Particle (SP) Model, as shown in Figure 1.3.

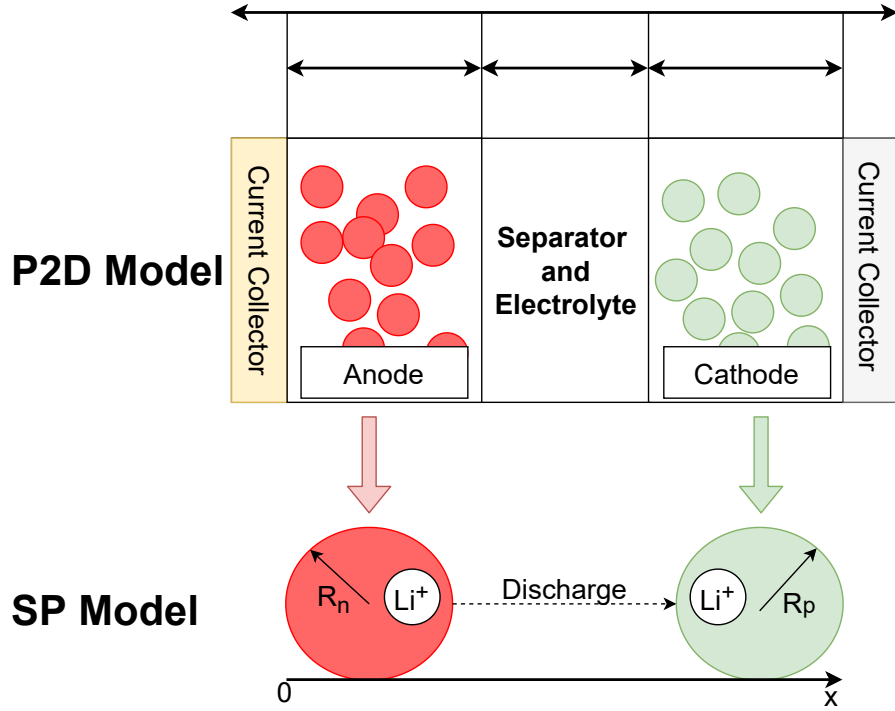


Figure 1.3 : Schematic of P2D model and SP model [3]

Doyle et al. proposed the P2D model for lithium-ion batteries [28]. The SP model, which is a simplified form of the P2D model, is the most mature simplified model of the physics-based electrochemical models [3]. A P2D model is more appropriate to analyse the mechanism of the lithium-ion battery, while the SP model is

more suitable for battery online SOC estimation [29].

1.2.3.3 Data-driven models

As computational ability and available battery operational data increases, it is possible to build purely data-driven battery models, which can automatically find the relationship among the variables of lithium-ion batteries without knowing the chemical characteristics of the batteries [27]. The process of building a battery model by the data-driven method is given in Figure 1.4. First, the real-time operational battery data (terminal voltage, current and temperature, etc) should be collected. Second, the collected data are trained with a proper algorithm, such as neural network [17], support vector machine [17], and extreme learning machine [30]. Finally, the battery terminal voltage can be estimated by using current and temperature. Data-driven models can achieve a high estimation accuracy theoretically. However, the models are easily influenced by training datasets.

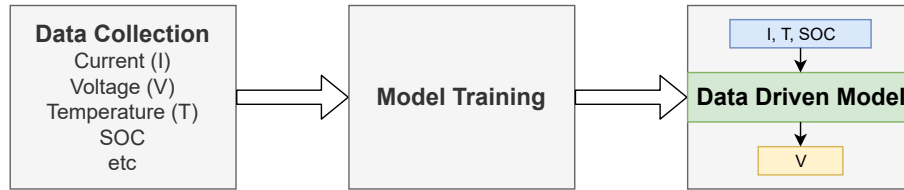


Figure 1.4 : Illustration of data driven model procedure

1.3 Introduction of Battery Management of System

The first BMS was built for online state monitoring of lead-acid batteries in 1991 [31]. This BMS only has very limited functions which are battery data acquisition and a brief SOC online estimation [10]. The BMS has achieved a great improvement as it now be embedded with battery models, observers, algorithms to achieve a high-precision battery states estimation. Moreover, the present BMS is a multi-function

system which has a data acquisition function, a states estimation function, a battery balancing function and a safety protection function, as shown in Figure 1.5.

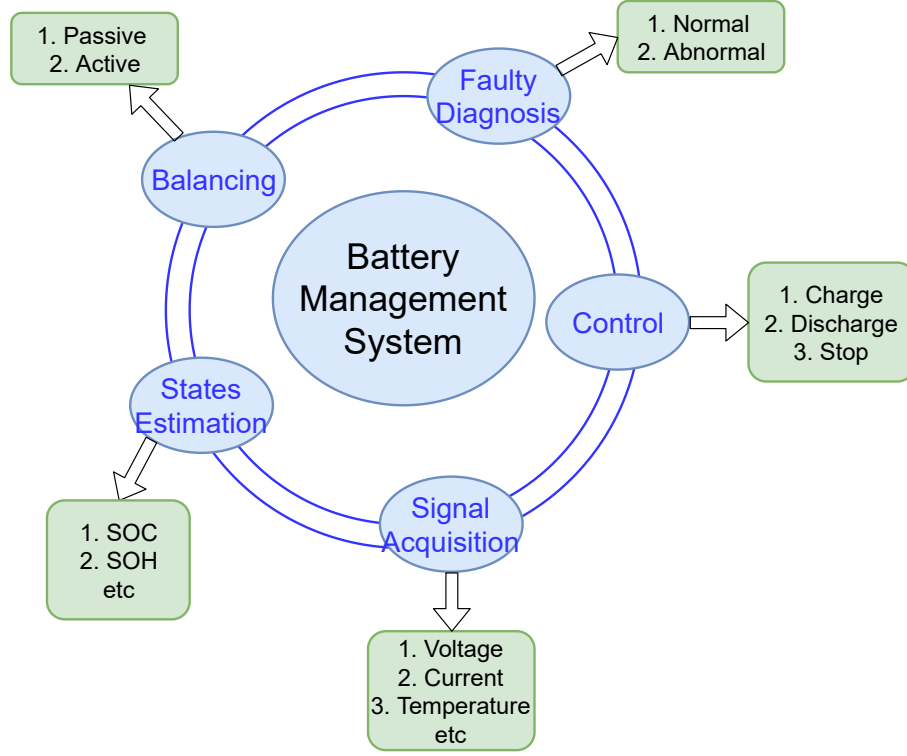


Figure 1.5 : Key functions of the BMS

1.3.1 Signal Measurement

The battery signal measurement is the fundamental step of the BMS [32]. Typically, three important battery signals can be directly measured by sensors: voltage, current, and temperature. Moreover, the battery EIS is also an important signal that should be measured since it is a useful indicator for further battery states estimation [25, 32]. The EIS is calculated based on the measured voltage and current rather than direct measurement.

1.3.2 States Estimation

To guarantee a safe and efficient battery operation, it is important for the BMS to monitor the battery states [32, 33].

1.3.2.1 *State of Charge (SOC)*

SOC, which is the ratio of the remaining to the full-charged capacity of the battery, can indicate how long the battery will last. The SOC cannot be directly measured by physical sensors but needs to be estimated based on measurable current, voltage and temperature signals of the battery. Accurate SOC estimation can help users to make the correct decision on when to charge the battery. Moreover, SOC is used with the control function of the BMS to avoid overcharge or over-discharge to guarantee a safe operation. Many methods have been proposed for SOC estimation, and they can be categorised into four groups: coulomb counting method, open-circuit voltage method, model-based method, and data-driven method.

1.3.2.2 *State of Health (SOH)*

SOH, which describes the battery health condition, is defined as the ratio of the present battery maximum capacity to the nominal maximum capacity, which is provided by the manufacturer. It is common knowledge that battery performance will degrade over repeated charging/discharging cycles. Normally, a battery is regarded as a fail battery when the SOH is less than 80%. The SOH can be estimated by battery parameters, such as battery impedance.

Accurate SOH estimation is vital for a safe operation. It can be estimated offline easily since the battery can be fully charged and discharge to check its present maximum capacity. It is necessary to estimate SOH online based on useful parameters. However, it is hard to measure battery impedance online.

1.3.3 Balancing

Because of the low voltage range and power of lithium-ion battery cells, they can normally be connected in series and parallel to form into a battery pack to reach the required voltage and power requirement [34]. However, it is a common issue that cells have intrinsic and extrinsic differences resulting in cell imbalance. A common imbalance is SOC difference between cells.

Battery imbalance brings many problems such as energy loss, reduced battery life-time and even safety risks. For example, the discharge operation will be stopped once the cell with the lowest SOC reaches the cut-off voltage and the charge operation will be stopped once the cell with the highest SOC reaches the cut-off current, as shown in Figure 1.6. Otherwise, there will be a safety issue if overcharge or over-discharge happens.

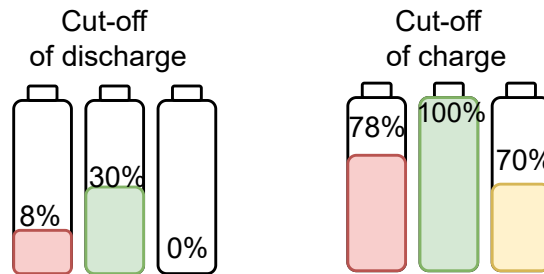


Figure 1.6 : Energy and capacity loss of the lithium-ion batteries under imbalance

To solve the unbalanced cells issue, various methods or topologies have been proposed [4]. These methods can be categorised into three groups, as shown in Figure 1.7. The first method is to release the redundant energy of the cell using passive components. The second method is to transfer the energy from high SOC cells to low SOC cells using active components. The third method is to use the cell-converter module to separately control charging/discharging current of every cell so that the SOC can finally achieve balance.

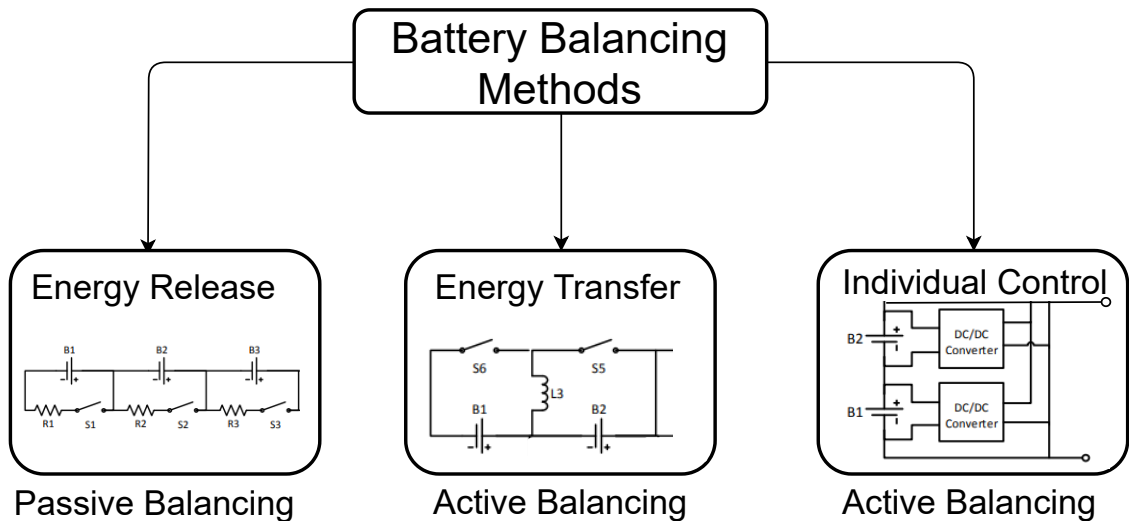


Figure 1.7 : Battery balancing methods [4]

1.4 Research Objectives

This thesis aims to develop an efficient, accurate, and robust online battery signals (states) estimation and monitoring system which uses fewer physical sensors and simpler measurement strategies to estimate the important battery information to guarantee a safe and reliable battery operation. The main research objectives of this thesis are given as follows:

- i. Propose an OCV measurement method to reduce the SOC-OCV measurement time for achieving a high efficient offline parameter identification measurement.
- ii. Propose an easily-implemented online battery impedance measurement method to the BMS.
- iii. Propose a sensorless battery surface temperature estimation method to reduce the cost and increase the reliability of the BMS.
- iv. Propose an optimal machine learning model for online battery SOC estimation.

1.5 Thesis Organization

An introduction to the battery storage system, including the lithium-ion battery and the BMS are given in the previous sections. According to the overview, there is space to improve the efficiency and reliability of the battery storage system from the measurement, modelling, and states estimation perspectives. This thesis is organised as follows:

- *Chapter 2:* This chapter presents a simple and effective rapid OCV measurement method based on the equivalent electric circuit relaxation model. First, two conventional OCV measurement methods and previous fast OCV measurement methods are reviewed. Second, by analyzing the relaxation model, a relationship between the current passing through the battery and its polarization voltage is observed. Third, by applying a proper one-cycle biopolar-current pulse (OCBCP) to the battery, the relaxation time for OCV measurement is largely reduced. Fourthly, this chapter shows that the proposed method shows a potential in online initial OCV correction for the online SOC estimation.
- *Chapter 3:* This chapter presents the switched resistor circuit (SRC) based online battery EIS measurement method. First, the principle and usage of the EIS, the conventional offline EIS measurement method, and previous online EIS measurement methods are reviewed. Second, by proving the previous converter-based duty-cycle perturbation method has a critical large output ripples issue, a SRC based perturbation method with reduced output voltage ripples is proposed and elaborated. The experimental impedance results obtained by the proposed method correspond with a high-accuracy laboratory battery impedance analyzer.
- *Chapter 4:* This chapter proposes a sensorless temperature estimation method for lithium-ion batteries using a recurrent neural network (RNN) with a gated

recurrent unit (GRU). The conventional surface temperature measurement methods and previous sensorless surface temperature estimation methods are reviewed. Compared with previous methods, the proposed method exploits information of the past battery surface temperature and measurements and yields better estimation accuracy.

- *Chapter 5:* First, a detailed theoretical analysis of different recurrent neural network models are elaborated. Second, a systematic experiment-based evaluation across a typical driving profile is applied to these advanced RNNs. Third, an optimal RNN model is proposed and this can achieve a high SOC estimation accuracy and light computation burden.
- *Chapter 6:* A brief summary of the thesis contents and its contributions are given in the final chapter. Recommendations for future research are given in addition.

Chapter 2

A Rapid OCV Measurement Method for Battery Modelling

2.1 Introduction

Lithium batteries have been used extensively in renewable energy systems, smart grid and electric vehicles because of their high energy density, long lifetime, and low self-release rate [35]. Overcharge or over-discharge of lithium-ion batteries may cause serious safety issues.

Based on the introduction of the chapter 1, it is known that the lithium-ion batteries are necessary to be well managed by the BMS to guarantee a safe operation [23,36,37]. One of the most important features needed to be monitored is the state of charge (SOC), which is an indicator of the available energy in the battery. However, SOC can only be estimated instead of directly measured by sensors [11,23]. A lookup table between the battery open-circuit voltage (OCV) and SOC has been widely adopted for online SOC estimation. However, it is time-consuming to obtain an accurate SOC-OCV correlation since the battery requires several hours to reach an inner-equilibrium state. In order to improve the SOC-OCV measurement efficiency, an rapid OCV measurement method will be introduced in this chapter.

Various methods have been proposed to estimate SOC including ampere-hour counting, model-based open circuit voltage (OCV) methods and machine learning method [36, 38–44, 44–47]. Ampere-hour counting is an efficient method for SOC calculation. However, it suffers from accumulating error from the current sensor during the battery operation [43]. Data driven method requires large amount of

offline training data to build a model otherwise it is hard to guarantee an accurate online estimation result [27]. Therefore, the model-based OCV method has been widely adopted due to its high accuracy and simplicity [36, 38, 39, 42, 43, 45]. Model-based OCV method utilizes an equivalent electric circuit model to calculate OCV combined with measured signals and refers to a SOC-OCV look-up table to estimate SOC [11, 42]. Since the online SOC estimation precision depends on the accuracy of the equivalent battery model and online measurement signals. Therefore, different closed-loop algorithms have been proposed to improve the estimation precision such as proportional integral [42, 48], extended Kalman filter [36, 39, 45], unscented Kalman filter [49], particle filter [50], and H-infinity filter [51]. Figure. 2.1 shows a common online SOC estimation procedure for the model-based OCV method.

2.2 Related Works and Research Gap

For model-based methods, an accurate SOC-OCV correlation is fundamental to ensure an accurate SOC estimation [11]. Normally, there are two methods to obtain SOC-OCV correlation: *low-current OCV test* and the *incremental OCV test* [11, 52]. The low-current method uses a very small current (e.g., C/20, C/25) to discharge or charge the battery so the related terminal voltage can be approximately assumed as OCV because the concentration polarization induced by the small current rates is small. The incremental OCV method uses a current pulse (e.g., 5% SOC, 10% SOC) to discharge/charge the battery followed by a long rest period after that the OCV with the corresponding SOC can be measured. This step is repeated until the battery is fully discharged/discharged. Finally, extra data points for the OCV curve can be obtained within the SOC intervals using the interpolation method.

Although these two methods are both correct theoretically and commonly adopted, the measured SOC-OCV curves obtained by these two methods have slight differ-

ences. As the basis of the model-based online SOC estimation, the inaccurate SOC-OCV relationship will have influence on online SOC estimation accuracy. Therefore, several works have comprehensively evaluated these two SOC-OCV test methods under various operational conditions [11, 52]. All these experimental results show that the SOC-OCV correlation measured by the incremental OCV method can have a higher online SOC estimation accuracy and estimation robustness [11, 52].

However, both of these two methods need twenty to thirty hours to get one group of SOC-OCV correlation data under a standard condition (new battery, 25°C). Moreover, since the battery SOC-OCV correlation is related to aging and temperature, it will require hundreds of hours to get a full picture of SOC-OCV relationships [53]. It is important to explore how to improve the measurement efficiency and shorten the measurement time without losing the accuracy.

There are some methods proposed to directly reduce the OCV measurement time or predict the equilibrium state OCV based on the measured voltage after a short relaxation time [35, 54–58]. To predict the OCV, a physical-based OCV model has been developed [55]. It tests OCV characteristics on an electrode level so it is accurate but this method is complex. In addition, the physical or electro-chemical based models usually have a heavy computational burden [57]. Some prediction-based methods use mathematical functions to perform curve fitting of the polarization voltage during the relaxation time from which related relaxation models can be obtained [54]. Because the parameters of relaxation function are not constant with the increase of relaxation time, Pei [35] updated this model with time varying parameters. Considering that mathematical model may be efficiently challenging for embedded implementation, Li *et al.* [56] proposed a mathematical and electrical combined model to predict the OCV. The key idea of aforementioned methods are to predict the equilibrium state OCV based on measured data and relaxation models. Thus, the prediction highly relies on the model accuracy. To improve the prediction

accuracy, Meng *et al.* [57] used a correction window to generate a feedback signal to adjust the prediction result. Yang *et al.* [58] proposed a method to actively reduce the polarization voltage by applying two sets of current.

There are several limitations to the method proposed in [58]. Firstly, there is a lack of discussion about how to eliminate the hysteresis voltage induced by the extra current pulses, especially a huge SOC loop (20%) is induced by the proposed current pulses in this work [58]. Secondly, the proposed experimental time for reducing polarization voltage in some scenarios is very long. For example, the proposed experimental time at 20% SOC is around 3200 seconds (or 53.3 minutes) during the discharge test. Thirdly, this method needs extra experiments to obtain parameters such as time constants and initial polarization voltage to calculate related amplitude and duration every time. Hence it cannot be implemented online in a short-time to re-correct the OCV due to its heavy computational burden.

To overcome these problems, this chapter proposes a simple and effective rapid OCV measurement method based on the equivalent electric circuit relaxation model. Firstly, by analyzing the relaxation model, there is a relationship between the current passing through the battery and its polarization voltage. Secondly, by observing this relationship and applying a proper one-cycle bipolar-current pulse (OCBCP) to the battery, it can reduce the relaxation time for OCV measurement. Thirdly, the proper OCBCP is proposed based on a trade-off between current duration, battery health, and the induced hysteresis voltage. Fourthly, this procedure shows a potential application for future online OCV re-correction. To highlight, not only does this chapter deduce an electric theoretical expression to accelerate the rate of change of polarization voltage, but it also provides a clear testing guideline for users without complex calculations.

The reminder of this chapter is organized as follows. The proposed rapid OCV

measurement method using OCBPC is given in Section 2.3. Specifically, The characteristics of the second-order equivalent electric circuit model are analyzed in Section 2.3.1 and Section 2.3.2. The experimental setup and the experimental data of the relaxation test are detailed in Sections 2.3.3 and 2.3.4. The result discussion is given in Section 2.4. Finally, the summary of the chapter is given in Section 2.5.

2.3 Proposed Rapid OCV Measurement Method Using OCBCP

As mentioned previously in [11], the incremental OCV measurement method shows a more accurate SOC estimation result compared with the low current method. In the incremental OCV test, the amplitude of current pulse is set to $0.5C$, and the current pulse width is decided by the required release capacity (e.g. 12 minutes for 10% SOC, 6 minutes for 5% SOC) then followed by a long rest period, as shown in Figure 2.1.

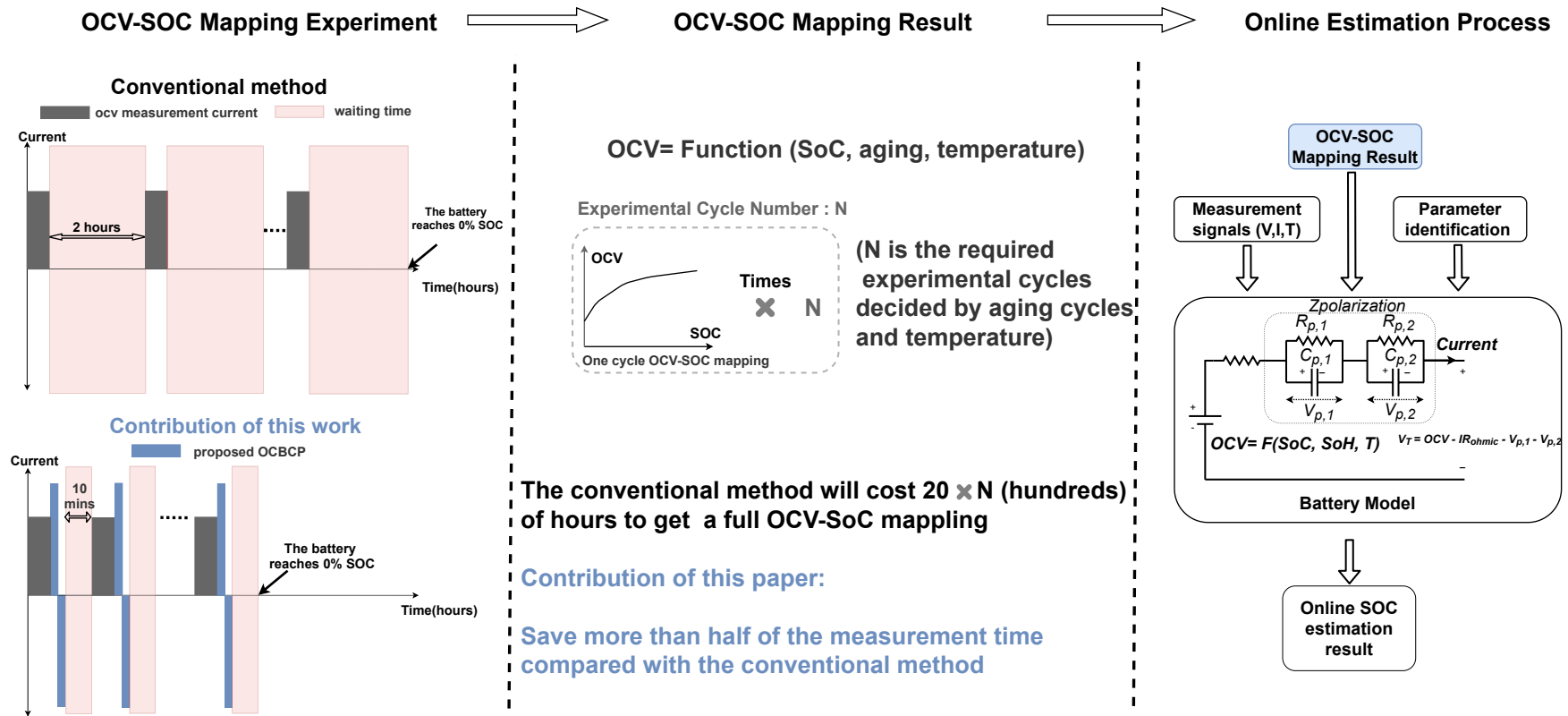


Figure 2.1 : Online SOC estimation process, problem of the conventional incremental OCV test method and the contribution of this work.

During the rest period, which can be called a relaxation process, the measured open terminal voltage is not equal to the equilibrium state OCV because of the overpotential, which is generated by the previous discharge or charge process. To measure the full SOC range of OCV, the battery needs to be idled for relaxation after each current pulse. There are different relaxation times proposed in [11, 57], but the minimum duration required is 1.5 hours. Typically, the second-order battery model is used to describe the battery's dynamic status for online estimation. In this chapter, the second-order battery model is proposed to mimic the battery relaxation behavior, as shown in Figure 2.2.

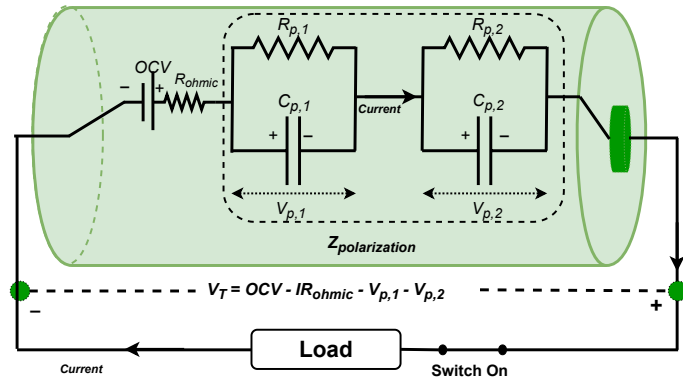
2.3.1 Physical Description of the Battery Model

The first part of this model is called OCV, which indicates the difference between the electrode potentials when the battery is in equilibrium. The second component is R_{ohmic} (ohmic resistance) that can represent the electrolyte and connection resistance, which will induce an immediate voltage change once the current is stopped. The third component is $Z_{polarization}$ (polarization impedance), which can be further divided into two parts: $Z_{p,1}$ (charge transfer) which is caused by charge transfer reactions on the surface of the electrode, and $Z_{p,2}$ (diffusion) which is caused by concentration polarization.

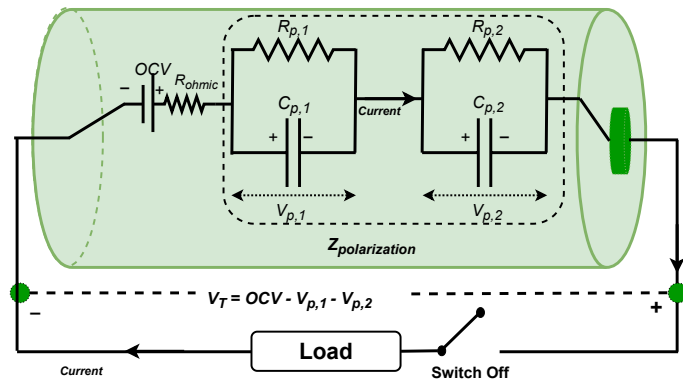
As shown in Figure 2.2, there are two working conditions of the battery, namely, operation mode and relaxation mode. In operation mode, there is a current flowing through the battery. Therefore, the terminal voltage is not equal to OCV due to the battery impedance, and their relationships during the operation model is discussed in (2.1).

$$V_T = OCV - V_{p,1} - V_{p,2} - IR_{ohmic} \quad (2.1)$$

where V_T is the terminal voltage of the battery, I is the current flowing through



(a)



(b)

Figure 2.2 : The second-order battery model. (a) The operation mode model when the switch is on; (b) The relaxation model model when the switch is off.

the battery, $V_{p,1}$ is the polarization voltage across the first RC pair, $V_{p,2}$ is the polarization voltage across the second RC pair.

From Figure 2.2 and (2.1), it can be known that the voltage induced by the ohmic resistor will suddenly drop to zero once the current is cut off. However, the voltage across RC pairs cannot disappear immediately. Therefore, the battery enters into relaxation mode, in which the energy stored in capacitors will release to resistors until they are fully exhausted. For an RC pair, the voltage response converges to steady state in about four to five time constants ($t=4\tau$, $\tau=RC$) [22]. Hence, the relationship between the open circuit voltage and the terminal voltage in the relaxation mode can be expressed as (2.2).

$$V_T(t) = \begin{cases} \text{OCV} - V_{p,1}(t) - V_{p,2}(t), & 0 < t \leq T_1 \\ \text{OCV} - V_{p,2}(t), & T_1 < t \leq T_2(t) \\ \text{OCV}, & T_2 < t \end{cases} \quad (2.2)$$

where T_1 is the time when the energy of the first RC pair has released, and T_2 is the time when the energy of the second RC pair has released.

2.3.2 Second-Order Relaxation Model Analysis

The conventional state-space equation of the battery model, which has been widely used in model-based OCV methods for online SOC estimation [11], is expressed as follows.

$$\begin{cases} \frac{dV_{p,1}}{dt} = \frac{I(t)}{C_{p,1}} - \frac{V_{p,1}(t)}{C_{p,1}R_{p,1}} \\ \frac{dV_{p,2}}{dt} = \frac{I(t)}{C_{p,2}} - \frac{V_{p,2}(t)}{C_{p,2}R_{p,2}} \end{cases} \quad (2.3)$$

Since the research goal of this chapter is to eliminate the polarization voltage instead of SOC estimation, (2.3) is rewritten from the polarization perspective to (2.4) and (2.5) for better analysis as follows.

$$V_{p,1}(t) = V_{p,1}(t_0)e^{-\frac{t}{R_{p,1}C_{p,1}}} + \frac{e^{-\frac{t}{R_{p,1}C_{p,1}}}}{C_{p,1}} \int_{t_0}^t e^{\frac{t}{R_{p,1}C_{p,1}}} I(t) dt \quad (2.4)$$

$$V_{p,2}(t) = V_{p,2}(t_0)e^{-\frac{t_0}{R_{p,2}C_{p,2}}} + \frac{e^{-\frac{t}{R_{p,2}C_{p,2}}}}{C_{p,2}} \int_{t_0}^t e^{\frac{t}{R_{p,2}C_{p,2}}} I(t) dt \quad (2.5)$$

where $V_{p,1}(t_0)$ and $V_{p,2}(t_0)$ are the initial polarization voltages across two RC pairs, $V_{p,1}(t)$ and $V_{p,2}(t)$ are the polarization voltages after time t , and $I(t)$ is the current flowing through the battery. To be directly used in micro-controllers for battery management systems, this continuous-time model needed to be converted into discrete-time ordinary difference equations, which assumes that the battery inputs and outputs are measured or sampled at a regular rate with period Δt seconds. To convert (2.4) and (2.5) to the discrete format, the first step is setting $t_0 = k\Delta t$ and $t = (k+1)\Delta t$, then assuming the current flowing through the battery is constant over the sampling time Δt [22]. Finally, the discrete-time ordinary difference equations can be described as

$$V_{p,1}[k+1] = V_{p,1}[k]e^{-\frac{\Delta t}{R_{p,1}C_{p,1}}} + \left(1 - (e^{-\frac{\Delta t}{R_{p,1}C_{p,1}}})\right) I[k]R_{p,1} \quad (2.6)$$

$$V_{p,2}[k+1] = V_{p,2}[k]e^{-\frac{\Delta t}{R_{p,2}C_{p,2}}} + \left(1 - (e^{-\frac{\Delta t}{R_{p,2}C_{p,2}}})\right) I[k]R_{p,2} \quad (2.7)$$

where $I[k]$ is the current flowing through the battery, $V_{p,1}[k]$ and $V_{p,2}[k]$ are the voltage across the RC pairs.

When the current is cut off ($i[k] = 0$), the battery enters into the relaxation mode. The polarization voltage relaxation rate in the conventional relaxation mode has been set as the reference equations, which can be written as

$$V_{p,1}[k+1] = V_{p,1}[k]e^{-\frac{\Delta t}{R_{p,1}C_{p,1}}} \quad (2.8)$$

$$V_{p,2}[k+1] = V_{p,2}[k]e^{-\frac{\Delta t}{R_{p,2}C_{p,2}}} \quad (2.9)$$

By observing (2.8) and (2.9), it can be found that in the relaxation mode, the polarization voltage at k is only decided by the time constant of the polarization pairs ($\tau_p = R_p C_p$) and the beginning polarization voltage ($V_p[k], k=0$). For a battery, which is under a standard incremental OCV-SOC test, the τ_p and $V_p[0]$ are stable when the battery enters into the relaxation mode. Therefore, for incremental OCV tests, the relaxation speed is an unchangeable value. It needs at least several hours to let the polarization voltage decreasing to zero, as discussed in (2.2).

However, (2.6) and (2.7) indicate that an extra current flowing through the battery at time k can influence the polarization voltage at next sampling time $k+1$. Based on the discussion above a current compensation based acceleration method is presented below.

2.3.3 Experimental Setup

There are two key experiments, namely, battery relaxation test and verification test. The first experiment aims to explore the relationship between polarization voltage and relaxation time. The second experiment, which is to verify the effectiveness and accuracy of the proposed fast OCV measurement method, will be elaborated in Section 2.4.

2.3.3.1 *Experimental Platform*

The experimental platform consists of a battery tester (ZKETECH) and a PC with ZKETECH software, which can command the tester and monitor signals (current and terminal voltage) of the cells. An NI 6009 data logger is used to provide another measurement of the terminal voltage for cross-checking, as shown in Figure 2.3.

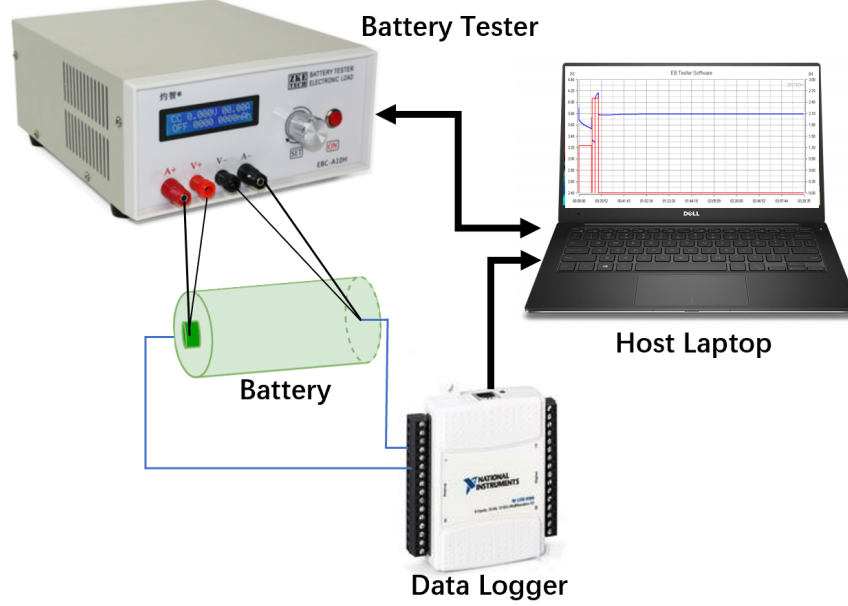


Figure 2.3 : Battery experimental platform.

Table 2.1 : Specifications of the batteries in the experiment

Sample Type	Material	Battery Voltage (V)	Capacity (Ah)
NCR18650	NCA	2.5-4.2	3.35
INR18650	NCM	2.5-4.2	2.5

2.3.3.2 Battery Information

Commercial lithium-ion 18650 cells are used in the experiments. Specifications of the tested battery cells are given in Table 2.1.

2.3.3.3 Battery Relaxation Test

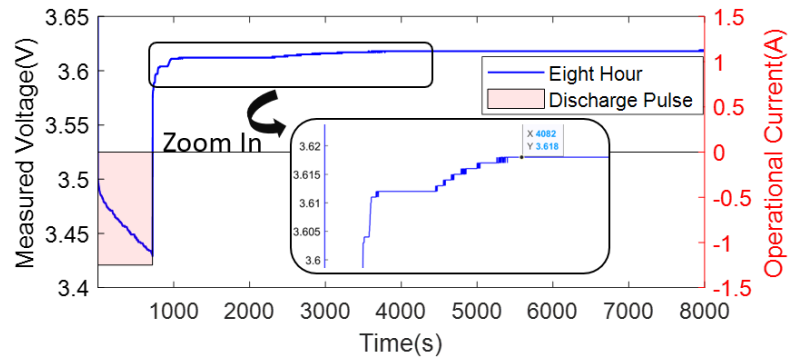
To understand the characteristics of relaxation behaviors, experiments are conducted by applying one discharge current pulse ($C/2$, 12 minutes, 10% SOC) to a new battery cell and measuring its terminal voltage. Then, the battery is allowed to

rest for eight hours and recording its open terminal voltage in the room temperature (25°C). For the sake of precision, there are three identical batteries to be tested by this experimental procedure. To exclude aging issues, all batteries are new, and the capacity has been verified before the test. Tests start from fully relaxed batteries (the open circuit voltage is 3.662 V). Figure 2.4 shows how terminal voltage changes when the battery is discharged at $C/2$ current and how the measured OCV changes with time after current stopping.

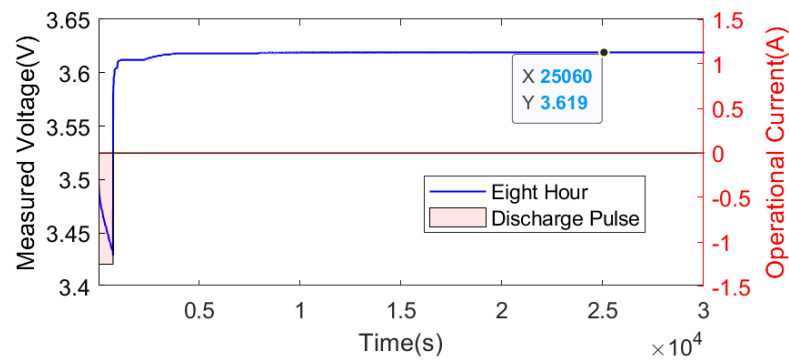
In the early stage of the relaxation (within 4000 s), the measured OCV rises fast. As the relaxation time increases, the rate of voltage rise slows down. As shown in Figure 2.4(a), the voltage increases from 3.582 V to 3.618 V in the first relaxation hour, and the voltage keeps at 3.618 V in next relaxation hour. As Figure 2.4(b) shows, the measured OCV only increases 1 mV after 6 hours. Therefore, the voltage value after two relaxation hours is regarded as the fully relaxed voltage. For model identification, the two hours measured voltage data after stopping discharge is adopted to build the battery relaxation model and investigate the relaxation characteristic of the battery.

2.3.4 OCBCP based OCV acceleration measurement method

The mathematical algorithm can be used to reduce the measurement waiting time [35, 54, 56, 57]. However, these algorithms use the historical data to predict OCV instead of reducing the polarization voltage across the RC pair to obtain a true OCV. Moreover, the second-order model, which has been widely adopted for online battery computation [36], is rarely used to investigate the offline relaxation behavior from an electrical view. By using the least-squares algorithm to analyse the measured data, a second-order relaxation model can be built for polarization voltage analysis. By considering the characteristics of the RC pairs in the equivalent circuit, a second-order model based OCBCP acceleration method is proposed in this section.



(a)



(b)

Figure 2.4 : Terminal voltage during discharging by 12 mins under $C/2$ and measured open circuit voltage after stopping discharge for different times. (a) After 2 hour; (b) After 8 hour.

2.3.4.1 Battery Relaxation Model Parameters Identification

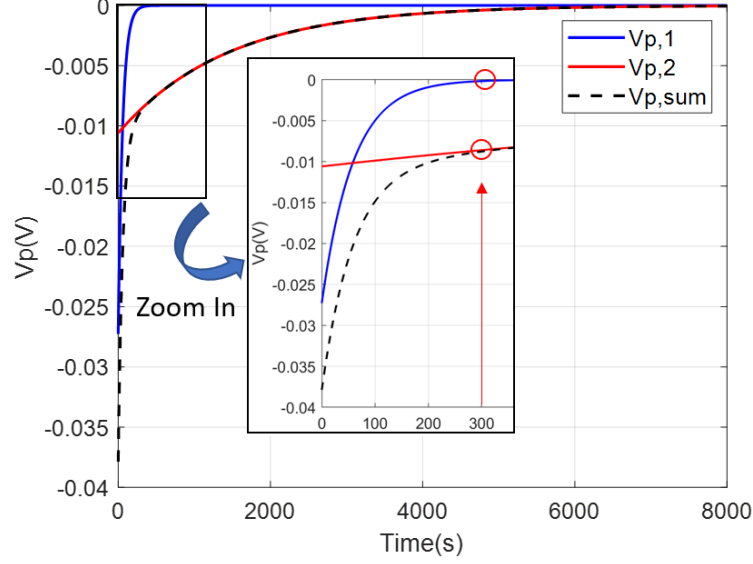


Figure 2.5 : Polarization voltage variations with time.

Based on the discussion of the lithium-ion battery, the 2-hour relaxation data is utilized to identify parameter vector θ of the second-order battery model

$$\theta = (V_{p,1}, V_{p,2}, C_{p,1}, R_{p,1}, C_{p,2}, R_{p,2}) \quad (2.10)$$

$$V_T = OCV + V_{p,1}(t_0)e^{-t/\tau_{p,1}} + V_{p,2}(t_0)e^{-t/\tau_{p,2}} \quad (2.11)$$

The nonlinear least-square curve fitting definition is expressed in (2.12). And the Levenberg-Marquard algorithm and Matlab curve fitting toolbox are adopted to calculate the identification results, which are listed in Table 2.2.

$$\min_{\theta} \|\mathbf{e}(\theta)\|_2^2 = \min_{\theta} (e_1(\theta)^2 + e_2(\theta)^2 + \dots + e_N(\theta)^2) \quad (2.12)$$

To separately explain the characteristics of two RC pairs, two polarization voltages ($V_{p,1}$ and $V_{p,2}$) during relaxation mode are simulated utilizing the estimated parameters in Table 2.2. As shown in Figure 2.5, $V_{p,1}$ reaches to around 0 mV at 300s. Therefore, the second period in (2.2) is the dominant part of the long idling period because the diffusion process of the second RC pair ($R_{p,2}$ and $C_{p,2}$) is very slow. In other words, the energy stored in this capacitor ($C_{p,2}$) needs a long time to release to the resistor ($R_{p,2}$). Hence, actively releasing the energy stored in the $C_{p,2}$ is a good choice to reduce the OCV measurement time.

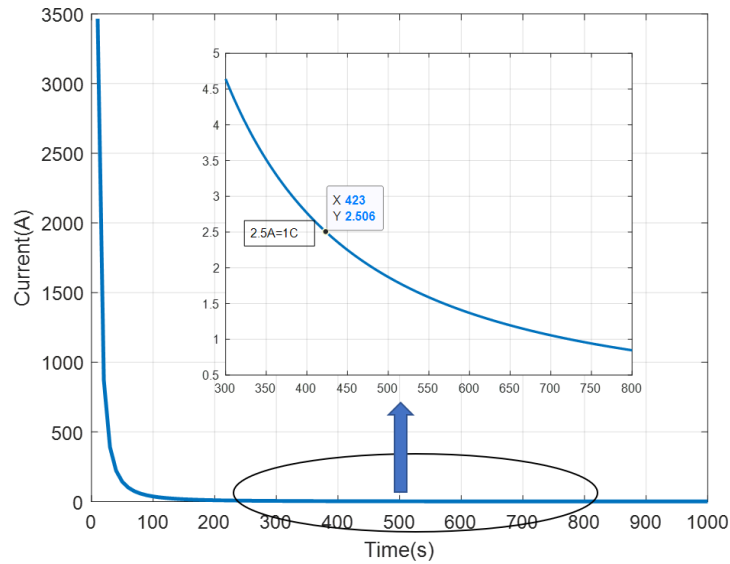


Figure 2.6 : The relationship between current pulse amplitude and duration of the polarization voltage zero-crossing point.

Table 2.2 : Battery Identification Results (OCV from 3.662V to 3.619V)

Data Source	$R_{ohmic}(\Omega)$	$R_{p,1}(\Omega)$	$C_{p,1}$ (F)	$R_{p,2}(\Omega)$	$C_{p,2}$ (F)	R-square	RMS modeling error (V)
Relaxation Test (2 hours data)	0.076	0.022	2674.5	0.0151	95695.4	0.9758	0.0006

2.3.4.2 OCBCP Acceleration Method

Injecting and extracting the same amount of capacity to/from the battery, the available capacity of the battery remains the same, as explained by

$$\int_0^{t_1} I_{ch} dt + \int_{t_1}^{t_2} I_{dis} dt = 0 \quad (2.13)$$

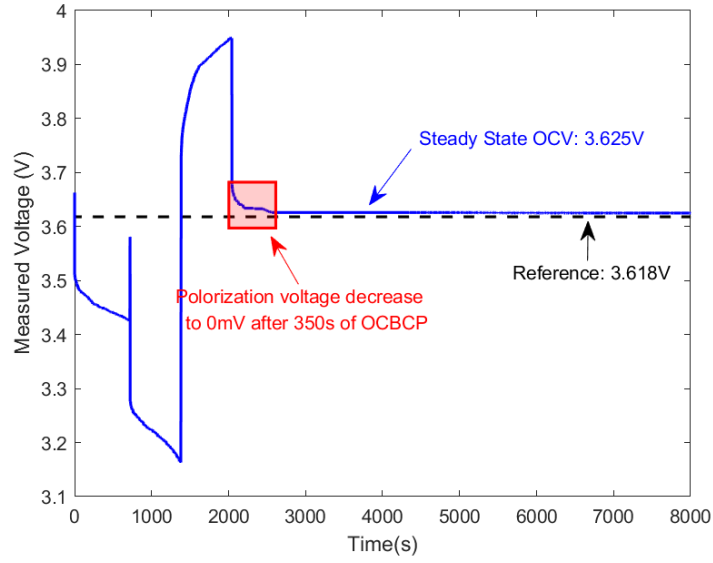


Figure 2.7 : The measured terminal voltage of battery by discharging 10% SOC followed by the calculated one-cycle bipolar-current pulse (1C,880s).

where I_{ch} is the charge current flowing into the battery, t_1 is the time of this charge current, I_{dis} is the discharge current flowing from the battery, and $t_2 - t_1$ is the time of this discharge current. The reminding capacity and SOC of the battery will not change with this bipolar-current pulse, but a smaller polarization voltage can be obtained.

The reason that a smaller polarization voltage can be obtained by adding OCBCP is depicted as

$$V_p(T) = \begin{cases} -|V_p(T_0)|e^{-\frac{T}{R_p C_p}}, & \text{after discharge} \\ +|V_p(T_0)|e^{-\frac{T}{R_p C_p}}, & \text{after charge} \end{cases} \quad (2.14)$$

The top term of (2.14) refers to the polarization voltage after the discharge process, the second term refers to the polarization voltage after the charger process. The following equations have the same structure.

$$V_p(T_1) = \begin{cases} -|V_p(T_0)|e^{-\frac{T_1}{R_p C_p}} - R_p|I|(1 - e^{-\frac{T_1}{R_p C_p}}) \\ +|V_p(T_0)|e^{-\frac{T_1}{R_p C_p}} + R_p|I|(1 - e^{-\frac{T_1}{R_p C_p}}) \end{cases} \quad (2.15)$$

$$V_p(T_2) = \begin{cases} -|V_p(T_1)|e^{-\frac{T_2}{R_p C_p}} + R_p|I|(1 - e^{-\frac{T_2}{R_p C_p}}) \\ +|V_p(T_1)|e^{-\frac{T_2}{R_p C_p}} - R_p|I|(1 - e^{-\frac{T_2}{R_p C_p}}) \end{cases} \quad (2.16)$$

$$T_1 = T_2 = T/2 \quad (2.17)$$

where $V_p(T_0)$ (V_p refers to $V_{p,1}$ or $V_{p,2}$) is the voltage of the RC pair at the beginning of the relaxation process, I is the amplitude of the current pulse, $V_p(T)$ is the polarization voltage after time T in the conventional relaxation condition, $V_p(T_1)$ is the polarization voltage after the first current pulse (I, T_1), $V_p(T_2)$ is the polarization voltage after the second current pulse ($-I, T_2$), R_p is the resistor value of the RC pair, C_p is the capacitor value of the RC pair, T_1 and T_2 are half of T .

Substituting (2.15) and (2.17) into (2.16), $V_{p,2}(T_2)$ can be updated as

$$V_p(T_2) = \begin{cases} -|V_p(T_0)|e^{-\frac{T}{R_p C_p}} + R_p|I|(1 - e^{-\frac{T}{2R_p C_p}})^2 \\ +|V_p(T_0)|e^{-\frac{T}{R_p C_p}} - R_p|I|(1 - e^{-\frac{T}{2R_p C_p}})^2 \end{cases} \quad (2.18)$$

$V_p(T_0)$ has a negative value due to the previous discharge operation, but it will have a positive value if the battery is charged. Since the principle and calculation steps are the same, only negative $V_p(T_0)$ (after discharge operation) is analyzed here for simplicity. When the $V_p(T_0)$ is negative, the second term in (2.18) is a positive

value. In this situation, if a proper current amplitude ($|I|$) and duration (T) could be chosen in (2.18), the polarization voltage (V_p) can reach to 0 mV much quicker than the conventional condition. It can be explained as

$$V_p(\hat{T}, \hat{I}) = -|V_p(T_0)|e^{-\frac{\hat{T}}{R_p C_p}} + R_p |\hat{I}|(1 - e^{-\frac{0.5\hat{T}}{R_p C_p}})^2 = 0 \quad (2.19)$$

As the amplitude and duration of current pulse increase, the value of V_p is changing from negative to positive. There is a zero crossing point of V_p , which represents that the polarization of this RC pair is zero. One current amplitude (I) has a corresponding duration (T) for zero crossing. Therefore, there are lots of amplitude and duration combinations that can accelerate the polarization voltage approaching to zero. $V_p(\hat{T}, \hat{I})$, \hat{T} and \hat{I} in (2.19) are used to refer these different combinations. And the relationship between the amplitude and duration of the zero-crossing point is given by Figure 2.6. Also, three things need to be considered to decide an OCBCP.

1) Current Rate: Large current is harmful to the battery. For example, the battery under test is INR18650-25R, whose datasheet shows that the standard charge current is 0.5C, and the rapid charge current is 1.6C. It is safer to keep the value of the current pulse to less than 1.6C (4A). So the current amplitude is chosen as 1C (2.5A), as shown in Figure 2.6.

2) Two RC Pairs: The two RC pairs in the relaxation model have different time constant values, as shown in Table 2.2. For a RC pair, the voltage reaches the steady state after current interruption at about four to five time constants [22]. Therefore, the polarization voltage of the first RC pair ($\tau_1=58.84$) can reach 0 mV at around 250 s regardless of the value of the initial relaxation voltage. Therefore, compensating the second RC pair and letting the first RC pair to self-release are enough to reduce the relaxation time. Besides, this consideration is simpler as compared with [58].

3) Low/high SOC Range: When the experiment is carried out at low/high SOC

range, the battery will reach to lower/upper voltage limit. Therefore, pulse testing regulation is proposed. For example, for a discharging process (at 80% SOC), the second pulse can be done at constant voltage mode until the charged capacity equals the released capacity of the first current pulse.

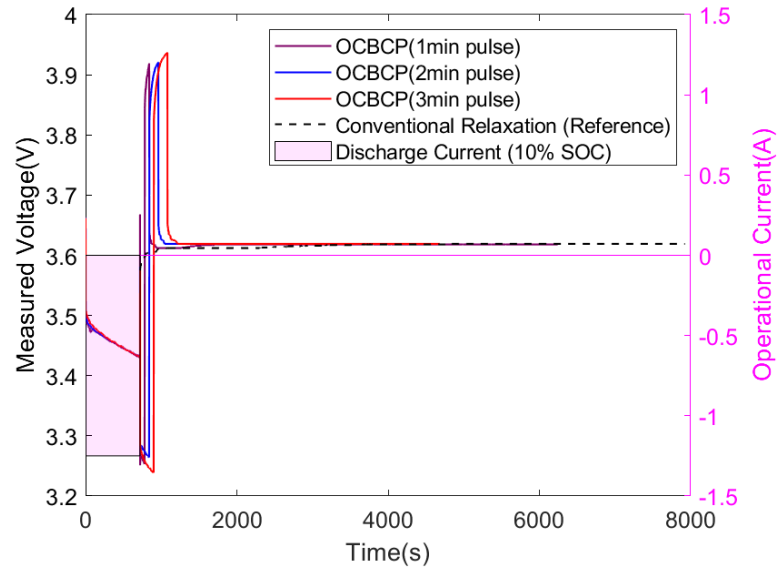
The current amplitude is chosen as 1C (2.5A). To make the polarization voltage become 0mV, the pulse time can be obtained by solving (2.19), and the calculated results are $T_1=T_2=T/2=440\text{s}$ and $T=880\text{s}$.

In Figure 2.7, the measured OCV directly reaches the real OCV just after 330s (approximately equals $5 \times \tau_1$). Therefore, this experiment result can verify the effectiveness of adding two current pulses. However, the OCV after this OCBCP is 3.625 V instead of 3.618 V due to hysteresis phenomenon, and the details can be found in [59].

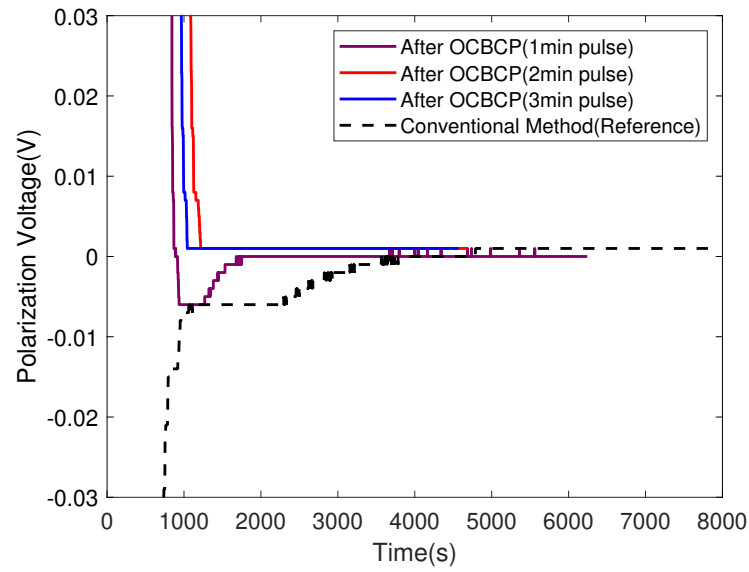
2.3.4.3 Improved Current Pulses Considering Hysteresis Voltage

To obtain an accurate OCV after the acceleration process, it is necessary to reduce the influence of hysteresis. The discharged/charged capacity during T_1 and T_2 are 0.305Ah (12.2% SOC). Compared with the increased capacity (10% SOC) per current pulse during the incremental OCV test, the changed capacity by this compensation pulse is relatively large. Hence, this large SOC loop induces a series hysteresis effect. It is necessary to find out an OCBCP which can reduce polarization voltage with a minimum hysteresis voltage.

Based on the analysis above, three sets of current pulses have been tested on batteries, and they are: 3A for one minute per pulse (2% SOC per current pulse), 2.5A (1C) for two minutes per pulse (3.3% SOC per current pulse) and 2.5A (1C) for three minutes per pulse (5% SOC per current pulse). The results are shown in Figure 2.8.



(a)



(b)

Figure 2.8 : Comparison of the polarization voltage curves after the proposed three sets of OCBCPs and the reference. (a) The measured voltage; (b) The polarization voltage (measured voltage minus the OCV).

Figure 2.8(a) shows the measured voltage during the experiment and after experiment. As shown, the OCV after the OCBCP step is 3.618 V, which is the same as the value measured by the conventional test, as shown in Figure 2.2. The experimental results prove that the hysteresis phenomenon is insignificant in small SOC loops. Figure 2.8(b) illustrates the relaxation time of these three OCBCPs. As shown, even the duration of three current pulses are not the calculated zero crossing time of (2.19), the polarization voltage still can reach to zero very fast. Because the decrease rate of polarization voltage is an exponential curve, the larger voltage drop slope of the second RC is utilized during the full self-release of the first RC, can be explained as

$$\frac{dV_p}{dt} = \frac{|V_p(0)|}{R_p C_p} e^{-\frac{t}{R_p C_p}} \quad (2.20)$$

2.4 Discussion of Results

2.4.1 Verifying the Experiment Procedure

The first part of this experiment is to use the conventional incremental OCV test procedure to build a standard reference.

1) The battery is fully charged to 100% SOC via the standard CC-CV charging profile. And the battery is rested for 2 hours to eliminate the polarization effects.

2) The battery is discharged by a current pulse (12 minutes, $C/2$, 10% SOC increment) followed by a 2-hour relaxation period at every 10% SOC.

3) The battery is charged by the same procedure as above but with an opposite current pulse.

The second part is adopting the proposed acceleration method, the comparison of these two experiment is shown in Figure 2.9 and Figure 2.10.

1) The battery is fully charged to 100% SOC via the standard CC-CV charging profile. And the battery is rested for 2 hours to eliminate the polarization effects.

2) To discharge the battery under the conventional incremental method every 10% SOC followed by the proposed acceleration OCBCP (3 minutes, 1C, +5% SOC and -5% SOC). During the pulse time, once the terminal voltage reaches to the upper voltage, the pulse changes to constant voltage charge mode until the charged capacity is equal to 5% SOC.

3) The battery is charged by the same procedure as above but with an opposite current pulse.

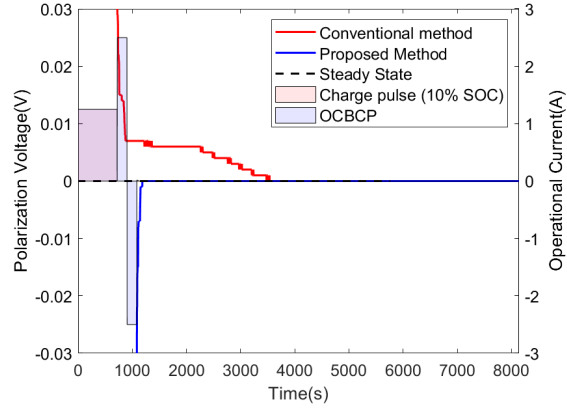
2.4.2 Validation Results

2.4.2.1 Validation Results at Incremental OCV Tests

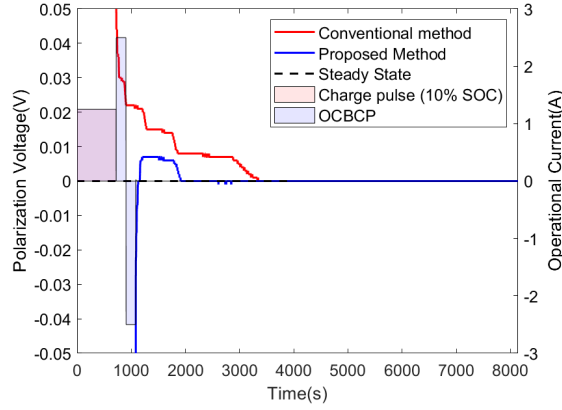
From [57], it can be known that the polarization phenomenon level is different with the change of SOC. Therefore, it is necessary to verify that the proposed OCBCP can properly reduce the required relaxation time for the whole SOC range. The experimental comparisons between the conventional incremental OCV tests and the proposed rapid OCBCP incremental OCV tests at different SOC levels are shown in this section.

Figure 2.9 and Figure 2.10 show comparisons of two polarization voltage curves (conventional method and proposed method) of the INR-18650 and NCR-18650 batteries at 30%, 50% and 80% SOC levels in charge and discharge conditions. The experimental results indicate that the proposed rapid OCBCP method can accelerate the polarization voltage decrements to 0 mV in most cases. However, in some scenarios, the polarization voltage after the rapid OCBCP only can reach quickly to -1 mV or 1 mV in a short time, then gradually approach to 0 mV. It is because the energy in the second RC pair is not fully released during OCBCP period and it needs extra time to self-release, as discussed in (2.19) and Figure 2.8.

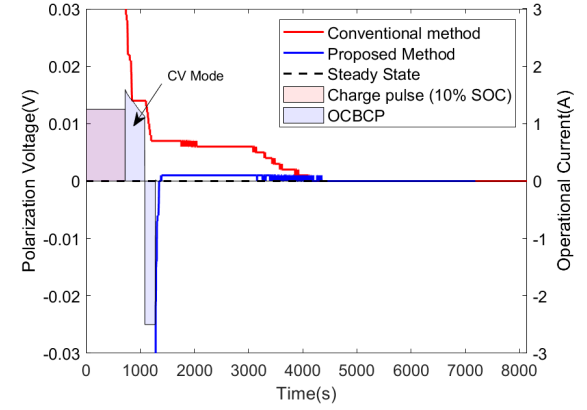
As aforementioned, the time duration of operational current pulse (charge/discharge) for the OCV measurement is 12 minutes (720 s). To calculate the relaxation time, the time of reaching to 0 mv polarization voltage needs to deduct from the operational current time (720 s). The detailed relaxation time comparison between the conventional incremental OCV method and the proposed rapid OCBCP incremental OCV method is given by Table 2.3.



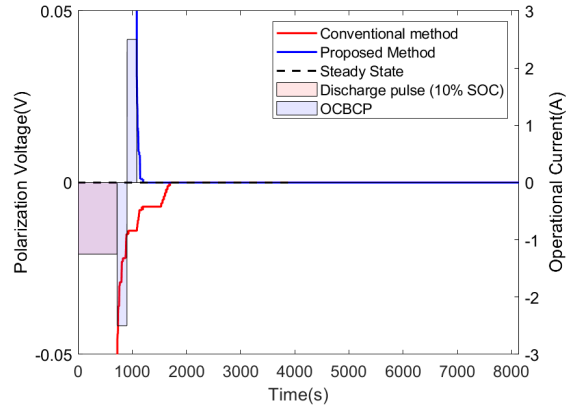
(a) INR charging: 30% SOC



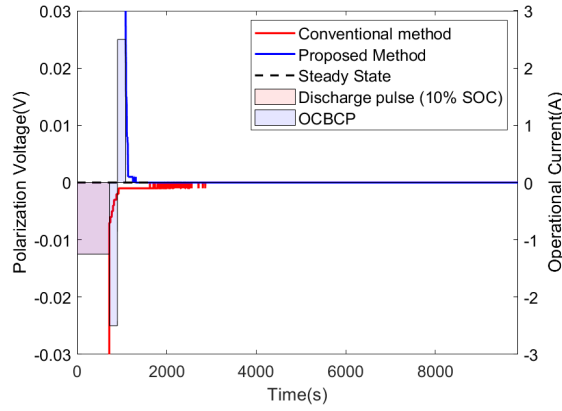
(b) INR charging: 50% SOC



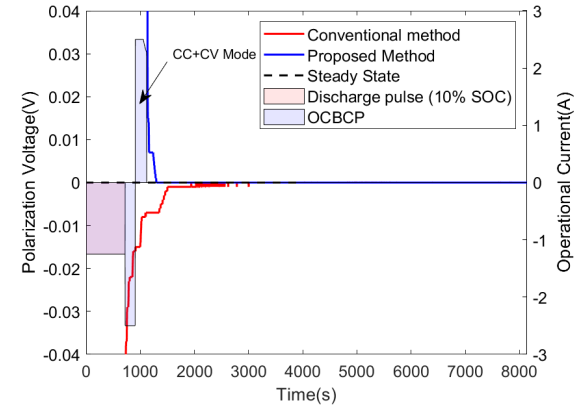
(c) INR charging: 80% SOC



(d) INR discharging: 30% SOC

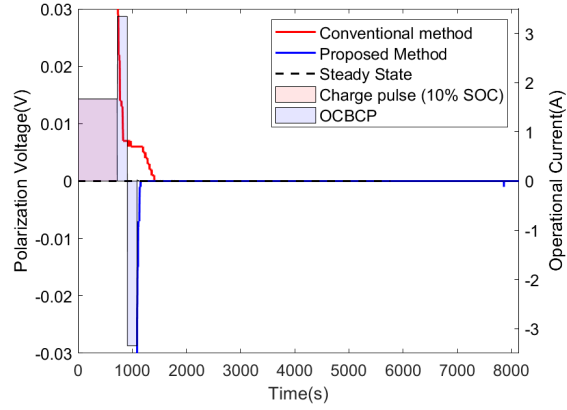


(e) INR discharging: 50% SOC

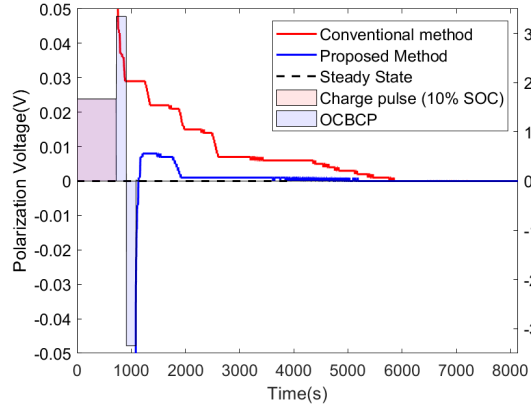


(f) INR discharging: 80% SOC

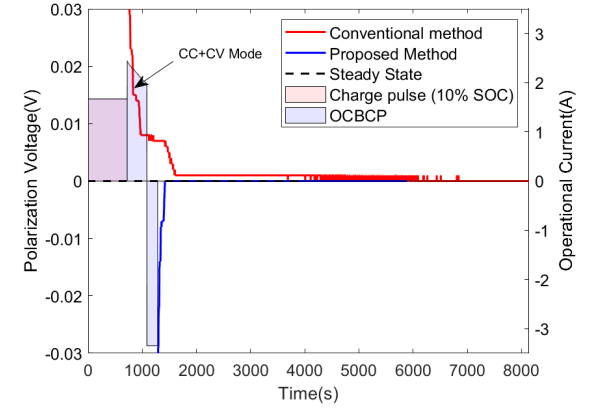
Figure 2.9 : Comparisons of polarization voltage curves of INR-18650 battery between the conventional incremental OCV method and the rapid OCV method under different settings.



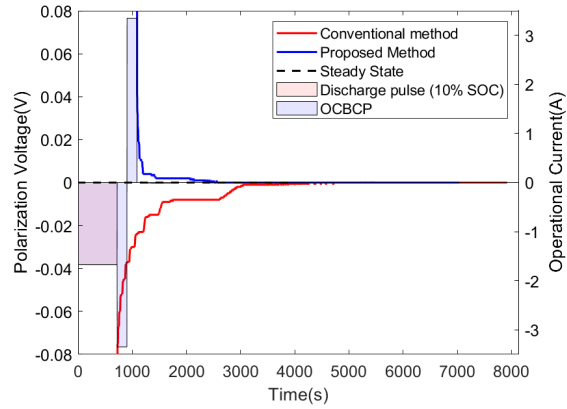
(a) NCR charging: 30% SOC



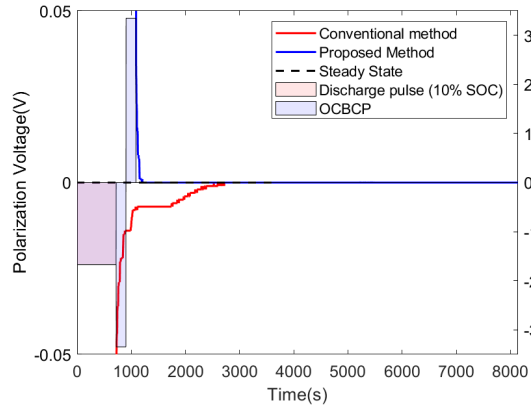
(b) NCR charging: 50% SOC



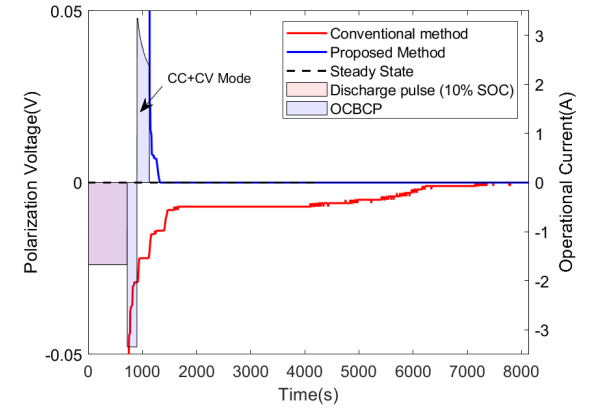
(c) NCR charging: 80% SOC



(d) NCR discharging: 30% SOC



(e) NCR discharging: 50% SOC



(f) NCR discharging: 80% SOC

Figure 2.10 : Comparisons of polarization voltage curves of NRC-18650 battery between the conventional incremental OCV method and the rapid OCV method under different settings.

2.4.2.2 Validation Results at Dynamic Conditions

It has been verified that the proposed rapid OCBCP can accelerate the relaxation process of the battery after a pulse with constant current, it is beneficial to prove that the proposed rapid OCBCP method also shows a good performance after dynamic load profiles. To mimic the dynamic load condition, a ten-minute current profile, which consists of charging and discharging current with different current rates, is applied to a fully relaxed battery with a 68% SOC (3.656V OCV), and the detail information of this dynamic profile is given in Figure 2.11. For the reference experiment, only the dynamic profile is applied to the battery. To validate the proposed method that can accelerate the polarization speed, the battery is operated with the dynamic profile followed by the OCBCP. The comparison between the conventional OCV performance and the proposed fast OCV performance after a dynamic profile has been given by Figure 2.11, which indicates that the polarization voltage can reach to 0 mV after 128 seconds of OCBCPs. Utilizing the rapid OCBCP method, it is possible to implement an OCV correction online to improve the SOC estimation accuracy.

2.5 Summary

This chapter proposed a rapid OCV measurement method, which utilizes OCBCP to reduce the initial polarization voltage and shorten the time for the battery to reach its equilibrium state for SOC estimation. First, by analyzing the OCV characteristics, the two-hour relaxation data has been chosen to build the relaxation model. Second, the second-order relaxation model has been analysed from an electric perspective for further current and polarization voltage utilization. Third, after investigating the effects of amplitude and time of the current on polarization voltage reduction, it is found that proper OCBCPs can reduce the initial relaxation voltage to accelerate the polarization voltage reach to 0V quicker. Fourth, a proper OCBCP

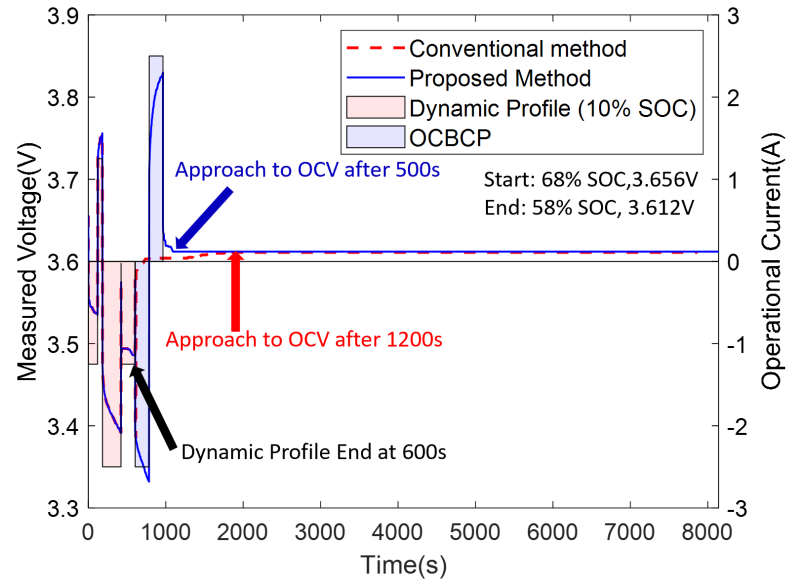


Figure 2.11 : Comparison of the conventional OCV performance (reaches to OCV at 1800s) and rapid OCV method performance (reaches OCV at 1100s) after the same dynamic current profile

Table 2.3 : Relaxation Time Comparison

		INR18650		NCR18650	
	SOC	Proposed	Conventional	Proposed	Conventional
		Method	Method	Method	Method
Charge	30%	440 s	2791 s	414 s	685 s
	50%	1197 s	2623 s	4463 s	5130 s
	80%	3613 s	3947 s	708 s	6148 s
Discharge	30%	481 s	979 s	1790 s	4023 s
	50%	585 s	2143 s	486 s	2028 s
	80%	650 s	2292 s	599 s	6627 s

was chosen based on a trade-off between time with reduced voltage value, battery health, and hysteresis voltage. The proposed method does not need extra calculation for different SOC points. Moreover, the effectiveness of the proposed method has been verified, which can save 30% to 90% relaxation time compared with that of the conventional incremental OCV method. Furthermore, the proposed OCBCP shows good performance under dynamic condition. Therefore, it has good potential for online OCV self-correction to estimate an accurate initial SOC. However, the rapid OCV measurement method proposed in this chapter was developed with new battery cell under the room temperature. For future work, the proposed technique should be extended to the aging battery under different temperature conditions.

Chapter 3

Battery Impedance Measurement Method

3.1 Introduction

According to chapter 1, it is known that a typical equivalent electric battery model, which can be used for online SOC estimation, consists of an open circuit voltage (OCV) and several electric components such as resistors and capacitors. As a fundamental step of building a battery equivalent circuit model, a rapid OCV measurement method is proposed in chapter 2. The next step of the battery modeling is to obtain the value of the electric components of the battery model. There are different methods to obtain the parameter values of the electric components [60,61]. Electrochemical impedance spectroscopy (EIS) is a common approach for parameter identification [61].

Moreover, EIS not only can be used for parameter identification of the battery modeling, and it also is a good indicator for battery online state estimation. For example, state of health (SOH) indicates the remaining lifetime of the battery cell. The impedance of the battery tends to increase with the decreasing of SOH [6,26,62], as given by Figure 3.1. For better battery modeling and state estimation, an online battery impedance measurement method is proposed in this chapter.

3.2 EIS Measurement Techniques

The related battery impedance-frequency relationship can be obtained by perturbing the battery with a small sinusoidal voltage or current at different frequencies. This technique is called EIS, which is a powerful tool to investigate the physico-

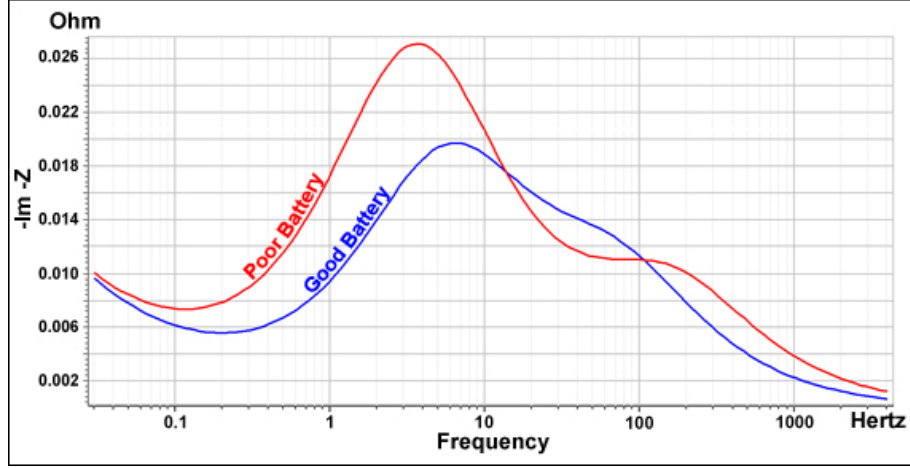


Figure 3.1 : EIS acquired at healthy and weak batteries [5]

chemical process occurring within the battery, evaluate battery performance, and monitor the battery states [26, 63, 64].

3.2.1 Single-Frequency Measurement

The battery is a nonlinear device. However, the battery can be assumed as a linear system in a sufficiently small current and voltage range. By utilizing this characteristic, the battery impedance ($Z_{bat}(f)$) can be measured by perturbing the battery with a small-step current at a specific frequency f and measuring the related voltage response, as given by

$$Z_{bat}(f) = \frac{V_{bat}(f)}{I_{bat}(f)} e^{j\theta_z} \quad (3.1)$$

where $V_{bat}(f)$ is the peak amplitude of battery voltage, $I_{bat}(f)$ is the peak amplitude of the battery current, and θ_z is the phase between the battery voltage and current. For a 18650 lithium battery cell, the perturbation current is around 200 to 400 mA, which is small enough to avoid non-linearity and large enough for noise immunity [63].

3.2.2 Multi-Frequency Measurement

Since the single-frequency measurement is relatively slow, the multi-frequency technique is also commonly adopted. A number N of persistent concurrent multiple sine waves at frequencies f_k are applied as an excitation, as follows

$$I_t = \sum_{k=1}^N \sin(2f_k \pi t) \quad (3.2)$$

The Fourier transform of the measured voltage and current can be used to calculate the impedance by adopting (3.1). A key consideration is that all frequencies should be integer multiples of the lowest frequency to ensure the periodicity.

3.3 Related Works and Research Gap

Conventional EIS measurement is usually conducted offline by sophisticated and complex laboratory equipment [64], which limits the adoption of EIS in real applications. To solve this problem, some online battery impedance measurement methods have been proposed [6, 25, 26, 63]. These methods can be classified into two categories: external signal injection and converter-based perturbation [6, 25, 26, 63, 65]. Specifically, the first category mainly uses the external source to generate small current or voltage signals to perturb the battery. For example, the battery is excited by the motor controller to measure its online impedance [26]. This method provides accurate results, but it has a limited working condition, which requires a motor system. The second category is controlling the duty-cycle of the power converter to perturb the battery [6, 25, 65]. Since power converters are usually an integral part of battery systems such as control of battery current and managing charging and discharging operations [63, 65], the second category methods have a wide application scenarios. Therefore, these methods have gained more attention due to their ease of use [65].

A converter-based single frequency perturbation method for online battery impedance measurement has been presented [25,63]. This method uses a sinusoidal perturbation current and voltage on the batteries at a selected frequency by sinusoidally perturbing the duty cycle of the power converter. These single-sine-frequency measurement methods can only obtain the impedance at a specific frequency [25]. Therefore, it takes a long measurement time to get the impedance plot at different frequencies. Since the battery impedance depends on the state of charge (SOC) [26], the results may be inaccurate due to the possible change of SOC during the long measurement time. To overcome this issue, various converter-based multi-frequency perturbation methods are proposed [6,65,66]. These methods obtain online battery impedance under different frequencies simultaneously by injecting a multi-sine excitation, square excitation or pseudorandom binary sequence excitation to the batteries.

However, the converter-based duty cycle perturbation methods have a critical shortcoming that the perturbation on duty-cycle will result in unavoidable ripples at the output voltage [25]. For example, in [25], the output voltage ripple value is around 7% and 9% of the DC output voltage when the perturbation frequencies are 1000 Hz and 100 Hz, respectively. The scenario will be worsen for the multi-frequency measurement method, which injects a square waveform perturbation to the duty-cycle [6,66]. It is known that the square waveform signal consists of infinite sine waveforms, but the amplitude of the signal (i.e. battery perturbation current and voltage) will become smaller with the increase of the harmonic frequency order [6]. Hence, a larger perturbation step is therefore needed to be applied to the duty cycle to increase the measurement accuracy at high harmonic frequencies. However, a larger perturbation duty cycle will inevitably induce larger output ripples based on the operational principle of the power converter. Moreover, the square waveform perturbation step also induces large current spikes to the battery [6,66], and it will accelerate the battery degradation and cause extra temperature rise [67].

Output voltage ripples is usually one of the key switching power supply specifications. This is particularly important for noise sensitive applications such as communications and medical equipment [68]. As suggested by Texas Instruments [69], the output voltage ripples usually designed to be less than 1% of the output voltage. As aforementioned, the output ripples in converter-based duty-cycle perturbation method is around 7%, which is far beyond this tolerable ripple range. As generally known, to solve the output ripple problem, the first method is to use the a capacitor with large capacitance and low equivalent series resistance (ESR), the second method is to add an LC filter, and the third method is to increase the switching frequency. However, all these methods are not suitable for this battery impedance measurement case. It is because the ripples are induced by the perturbation frequency rather than switching frequency, and the battery impedance measurement range can start from mHz to kHz [62,64]. It presents a significant challenge to size a filter to cover this wide frequency spectrum.

To overcome this output ripple problem, a ripple cancellation method is presented. In [6], the outputs of two power converters are connected in series, and each converter has a battery at its input. Two converters are injected with a perturbation individually but the two signals are out of phase with each other. Therefore, this method requires at least a multiple of two sets of battery and power converter working together to achieve output ripple cancellation [6]. However, the output voltage ripple issue remains an unsolved problem for the single power converter system (i.e. one converter per battery pack), which has been widely used. For example, a data center which adopts a single power converter approach [70], in which the power converter needs to be disconnected from the DC bus and connected to a isolated load when the battery is operated under the impedance measurement mode.

Considering the limitation of previous converter-based impedance measurement methods, this chapter presents a switched resistor circuit (SRC) based online bat-

tery impedance measurement method with suppression of output voltage ripples and battery current spike. In the proposed method, a SRC, which consists of a resistor and a controlled MOSFET, is added to the input side of the converter. By moving the perturbation source from the duty-cycle of the converter to the input-side of the converter, the output voltage ripples will be reduced due to the principle of the converter system transfer function. Moreover, by simply switching the MOSFET of the SRC with 50% duty-cycle at a specific frequency, corresponding small square perturbation current/voltage signals will be superimposed over the battery DC steady-state values. As generally known, the square waveform is composed of an infinite sinewaves with its odd-integer harmonic frequencies. Therefore, the proposed method can measure the battery impedance under different frequencies in one perturbation cycle by using discrete-time Fourier (DTF) technique. Therefore, the proposed method can achieve output voltage ripple reduction and multi-frequencies impedance measurement simultaneously.

This chapter is organized as follows. The theoretical review of the power converter is given in Section 3.4. The converter-based duty-cycle perturbation battery impedance measurement method is reviewed in Section 3.5. The proposed SRC perturbation method for output voltage ripples reduction is elaborated from theoretical, simulation and experiment perspectives in Section 3.6. The multi-frequencies impedance measurement of the proposed SRC perturbation method in online battery impedance and experimental results are reported in Section 3.7. Finally, Section 3.8 gives the conclusion.

3.4 Review of Converter Normal Operation

The boost converter (see Figure 3.2) is used in this chapter as it is the most commonly used topology in converter-based online impedance measurement due to its circuit simplicity and smooth input current capability [6, 25, 66].

When the boost converter is operated under an ideal continuous conduction mode (CCM), the input resistance of the converter system is given as below

$$R_C = (1 - D_{dc})^2 R_O \quad (3.3)$$

where R_O is the output equivalent resistance and D_{dc} is the DC duty cycle.

As shown in Figure 3.2, the current flowing through the battery can be expressed as

$$\begin{cases} I_{B,dc} = \frac{OCV}{Z_B + R_C} \\ V_{B,dc} = OCV - I_{B,dc} Z_B \end{cases} \quad (3.4)$$

where $I_{B,dc}$ is the battery current, $V_{B,dc}$ is the terminal voltage of the battery, OCV is the open circuit voltage of the battery, Z_B is the internal impedance of the battery, and R_C is the input impedance of the converter system seen from the battery side.

Finally, the output voltage of the power converter ($V_{O,dc}$) is given below

$$V_{O,dc} = \frac{V_{B,dc}}{1 - D_{dc}} \quad (3.5)$$

From Figure 3.2 and above analysis, it can be known that the battery current, battery voltage and output voltage are similar to DC values when the converter system is operated under a steady state CCM condition.

3.5 Review Converter-Based Duty-Cycle Perturbation Battery Impedance Measurement Method

For the converter-based online battery impedance method in [6, 25, 66, 71], the duty-cycle is perturbed at a given frequency (f_p) around its steady-state value (D).

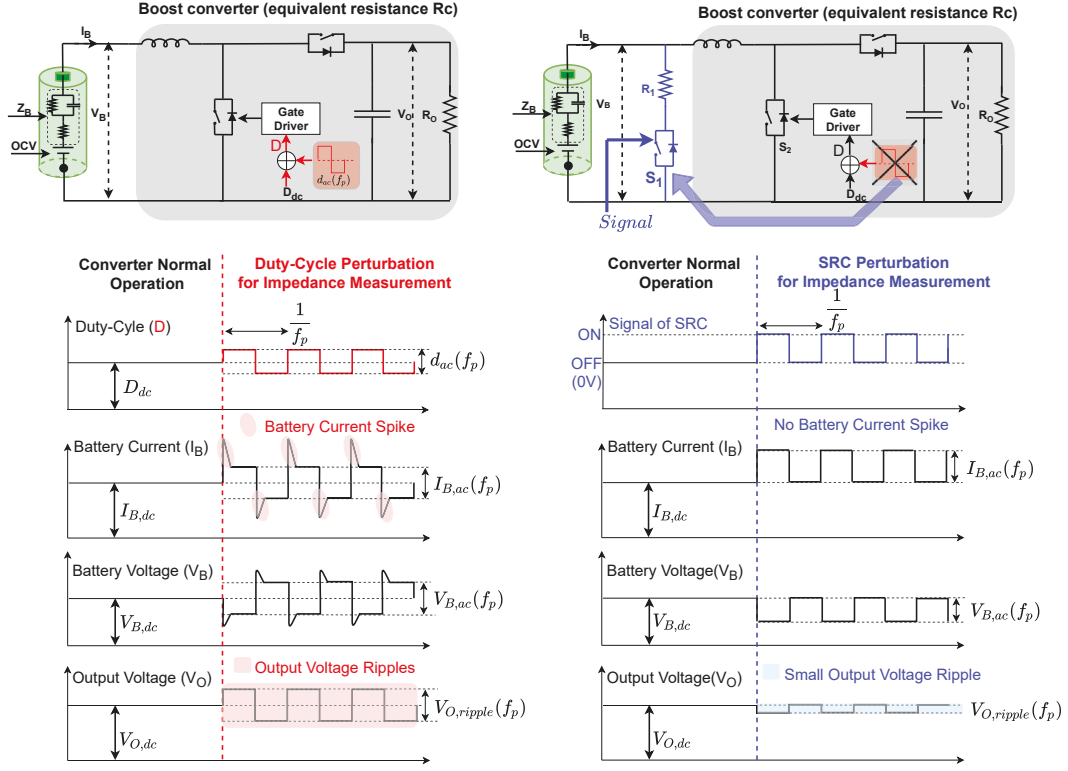


Figure 3.2 : Illustration diagrams for battery impedance measurement methods: conventional duty-cycle perturbation method [6] (left), the proposed SRC perturbation method (right)

This duty-cycle perturbation will result in small signal ac perturbations of the battery current and voltage around their corresponding steady-state dc values ($I_{B,dc}$ and $V_{B,dc}$). As illustrated in Figure 3.2, a square wave perturbation signal (d_{ac}), which is under f_p frequency, is added to the DC duty-cycle of the boost converter, the detailed duty-cycle perturbation information is given below

$$D = D_{dc} + \hat{d}_{ac} = \begin{cases} D_{dc} + \frac{d_{ac}}{2}, & 0 \leq t \leq \frac{1}{2f_p} \\ D_{dc} - \frac{d_{ac}}{2}, & \frac{1}{2f_p} < t \leq \frac{1}{f_p} \\ D_{dc}, & \text{otherwise} \end{cases} \quad (3.6)$$

Based on the principle of the converter transfer function, this small square wave

duty-cycle perturbation will inevitably result in output voltage ripples to the power converter, as shown in Figure 3.2. As reported by [25], the output voltage ripples are around 9% of the steady-state DC output voltage, which exceeds the general output voltage ripple requirement (should be less than 1%) [69]. Moreover, the duty-cycle perturbation will also result in large current spike to the battery due to the converter transient characteristic. And these spikes may accelerate the battery degradation.

3.6 Proposed Switched Resistor Circuit Perturbation Method for Output Voltage Ripples Reduction

In order to alleviate the aforementioned output voltage ripple problem, a switched resistor circuit (SRC) based online impedance measurement method is proposed in this chapter, as shown in Figure 3.2. An auxiliary branch named SRC, which consists of a resistor (R_1) and a switch (S_1), is added to the input side of the converter.

3.6.1 Principle of the SRC Perturbation Method

When the switch (S_1) of SRC is turned off, the power converter is under the normal operation and the input impedance of the converter system seen from the battery side is the R_C , which has been defined in Section 3.4. When the switch of the SRC (S_1) is turned on, the resistor (R_1) of the SRC is connected with R_C in parallel. In this case, the system equivalent resistance seen by the battery is updated to R'_C , which is given by

$$R'_C = \frac{R_C R_1}{R_C + R_1} \quad (3.7)$$

Figure 3.2 shows that if S_1 is controlled by a 50% duty cycle under a perturbation frequency (f_p), the SRC acts as a variable resistor switching between R_C and R'_C

with f_p . It can be called impedance measurement mode, in which the DC current and voltage of the battery are superimposed with small square perturbation signals, expressed as follow:

$$\hat{R}_C(f_p) = \begin{cases} R_C, & 0 \leq t \leq \frac{1}{2f_p} \\ R'_C, & \frac{1}{2f_p} < t \leq \frac{1}{f_p} \end{cases} \quad (3.8)$$

where $\hat{R}_C(t)$ is the variable resistor representing the impedance of the converter system.

$$\begin{cases} I_B(f_p) = \frac{OCV}{Z_B + \hat{R}_C(f_p)} \\ V_B(f_p) = OCV - I_B(f_p)Z_B \end{cases} \quad (3.9)$$

3.6.2 SRC Parameter Selection

For a simple demonstration of the perturbation step selection, a 18650 lithium battery is used as an example. For a common 18650 cell, its voltage range normally is between 2.5V and 4.2V, and the nominal voltage is 3.6V [72]. The impedance of this type of battery cell normally is 30-100 m Ω . For a EIS measurement, it requires at least 15 mV perturbation voltage to evaluate the battery impedance. Based on the EIS measurement voltage and internal impedance value, it can be calculated that a 150 to 400 mA perturbation current is required. To meet this requirement, a 10 Ω resistor can be chosen for the SRC. Since the maximum current is around 400 mA, the instantaneous power of this resistor is 1.6 W. It should be noted that the measurement time is very short, so the total consumption energy will be less than 2J in this work. Finally, a 10 Ω with 3 W resistor and a typical IRF540N MOSFET ($r_{DS} = 0.077\Omega$) are selected for the SRC in this chapter.

3.6.3 Theoretical Verification of Output Voltage Ripple Reduction in Proposed SRC Perturbation Method

When a perturbation is applied to the duty-cycle, unavoidable ripples will be added to the output voltage. To have smaller power converter output voltage ripples, a smaller perturbation step is preferred. But if the duty cycle perturbation step is too small, it cannot generate enough perturbation current for battery impedance measurement. The proposed SRC perturbation mitigates both issues, and this section explains through small-signal analysis the capability of the proposed SRC perturbation method compared with conventional duty-cycle perturbation method under the same battery perturbation current.

The small-signal ac linear circuit model of the boost converter operating under CCM is used for system analysis, as shown in Figure 3.3. In Figure 3.3, r_C is the capacitor ESR. The small-signal ac components of duty-cycle, switching current and inductor current represented by d , i_s and i_l , respectively. And r , which is the equivalent converter resistance, is derived using the conduction losses of the boost converter [73], as

$$r = r_L + D_{dc}r_{DS} + (1 - D_{dc})r_F \quad (3.10)$$

where r_L is the inductor equivalent series resistance (ESR), r_{DS} is the MOSFET ON resistance, and r_F is the diode forward resistance.

The small-signal model can be used to find the transfer function and transient performance from the disturbance duty-cycle (d_{ac}) to the output voltage ($v_{o,ac}$) and disturbance input voltage ($v_{B,ac}$) to output voltage ($v_{o,ac}$).

The duty cycle to output voltage transfer function T_p can be derived as

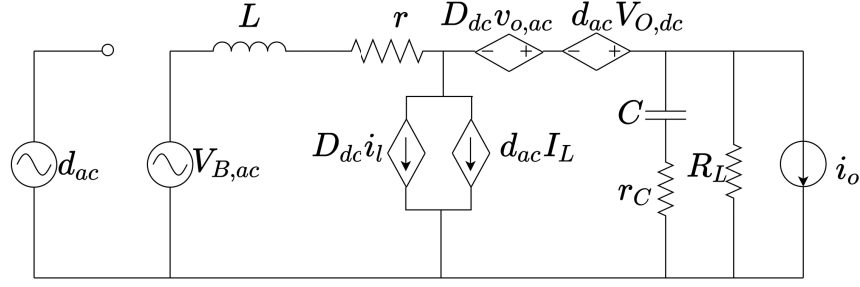


Figure 3.3 : Small-signal model of boost converter operating in CCM (Reproduced with permission from [7],IEEE, 2019)

$$T_p(s) = \left. \frac{v_{o,ac}(s)}{d_{ac}(s)} \right|_{v_{B,ac}=0} = T_{px} \frac{(s - \omega_{zp})(s + \omega_{zn})}{s^2 + 2\zeta\omega_n s + \omega_n^2} \quad (3.11)$$

where

$$T_{px} = \frac{-r_C V_{O,dc}}{(R_L + r_C)(1 - D_{dc})} \quad (3.12)$$

$$\omega_{zp} = \frac{R_L(1 - D_{dc})^2 - r}{L} \quad (3.13)$$

$$\omega_{zn} = \frac{1}{Cr_C} \quad (3.14)$$

$$\omega_n = \sqrt{\frac{(1 - D_{dc})^2 R_L + r}{LC(R_L + r_C)}} \quad (3.15)$$

$$\zeta = \frac{C[r(R_L + r_C) + R_L r_C(1 - D_{dc})^2] + L}{2\sqrt{LC(R_L + r_C)[r + (1 - D_{dc})^2 R_L]}} \quad (3.16)$$

and $T_p(0)$ is

$$T_p(0) = \frac{V_O[(1 - D_{dc})^2 R_L - r]}{(1 - D_{dc})[(1 - D_{dc})^2 R_L + r]} \quad (3.17)$$

The input (battery terminal voltage)-to-output voltage transfer function, which shows the variation of the output voltage of small perturbations in the input, is expressed as follows

$$M_v(s) = \left. \frac{v_{o,ac}(s)}{v_{B,ac}(s)} \right|_{d_{ac}=0} = M_{vx} \frac{s + \omega_{zn}}{s^2 + 2\zeta\omega_n s + \omega_n^2} \quad (3.18)$$

where

$$M_{vx} = \frac{r_C R_O (1 - D_{dc})}{L (r_C + R_L)} = \frac{(1 - D_{dc})}{L} (r_C \parallel R_L) \quad (3.19)$$

and $M_v(0)$ is

$$M_v(0) = \frac{(1 - D_{dc}) R_L}{(1 - D_{dc})^2 R_L + r} \quad (3.20)$$

As aforementioned in Section 3.6.2, it can be known that amplitude of the $v_{B,ac}(s)$ and is around 15mV for battery perturbation. For duty-cycle perturbation method, the d_{ac} is suggested to be 0.02 [25]. By applying these values for calculation, the comparison of theoretical transient response of M_v and T_p can be obtained and the results are shown in Figure 3.4.

Figure 3.4(a) shows that the stable output voltage ripples is 0.246 V, and the spike voltage is 0.3472 V. Figure 3.4(b) shows that the stable output voltage ripples is 0.028 V, and the spike voltage is 0.04269 V. When the duty-cycle perturbation is negative, the induced output ripple will be -0.3472 V. Therefore, the total output ripples of the duty-cycle perturbation method will be 0.6944 V, which is around 10% of the DC output voltage and this value cannot meet the standard ripple requirement (less than 1%) [69]. The theoretical analysis shows that the output ripple of the proposed SRC perturbation method (0.028 V) is around 16-times smaller than the duty cycle perturbation method (0.6944 V).

Table 3.1 : Parameters of the theoretical analysis and simulation for ripple analysis

Design Parameter	Value
Battery OCV	3.5V
R_{b0}	0.0322 Ω
R_{b1}	0.026 Ω
C_{b1}	375.94 F
Duty Cycle D	0.5
Inductor L	4.7 μ H
Capacitor C	220 μ F
Inductor ESR r_L	0.0028 Ω
Capacitor ESR r_C	0.311 Ω
MOSFET ON Resistance r_{DS}	0.077 Ω
Diode Forward Resistance r_F	0.072 Ω
Operation frequency	150kHz
Perturbation frequency	200Hz
Output resistor R_O	10 Ω

3.6.4 Simulation Verification of Output Voltage Ripple Reduction in Proposed SRC Perturbation Method

To further prove this theoretical conclusion, the proposed SRC perturbation method and duty-cycle perturbation method are simulated, and the regular converter operation is also simulated for comparison. The specifications of the converter used in this simulation have been given in Table I, with the additional components for the SRC as follows: a $R_1=10\Omega$, a MOSFET with 50% duty cycle. In this simulation, a typical electrical battery model, which consists of one ohmic resistor (R_{b0}) and one RC pair (R_{b1}, C_{b1}), is used to represent the lithium battery, as shown by the battery model in Figure 3.2.

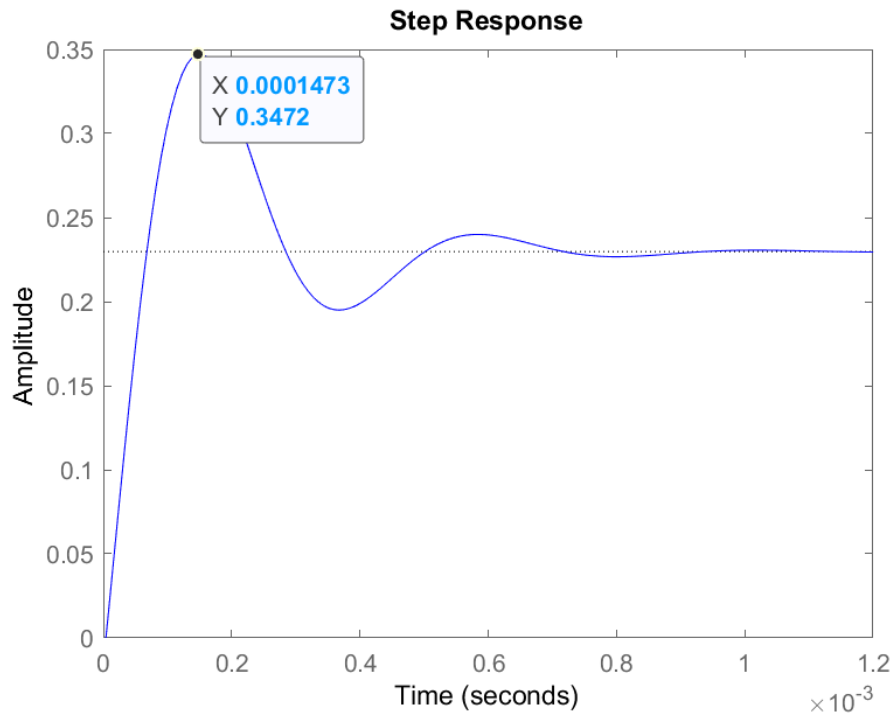
Figure 3.5(a) shows the waveforms of the dc duty-cycle (D_{dc}), battery current ($I_{B,dc}$), battery voltage ($V_{B,dc}$), and output voltage ($V_{O,dc}$) when the converter is operated under the normal power delivery condition (without any perturbation). Figure 3.5(b) shows the waveforms of the dc duty cycle (D_{dc}) with a small duty-cycle perturbation (d_{ac}), the battery current (I_B), battery voltage (V_B) and output voltage (V_O) when the duty-cycle perturbation (d_{ac}) is applied to the converter.

First, the output voltage ripples induced by the converter operational switching frequency is only 15mV, which is 0.23% of the corresponding DC output voltage. After adding a 0.02 perturbation signal to the duty cycle, the output ripple value is increased to 849mV, which is approximately 13% of the corresponding DC output voltage. As aforementioned, the required perturbation current for 18650-size battery cell is around 150 to 400 mA. A smaller perturbation duty-cycle step (such as 0.01) can bring smaller output ripples [6]. However, the generated perturbation current for the battery is only 0.1 A, which cannot meet this current range. The detailed comparisons are listed in Table 3.2.

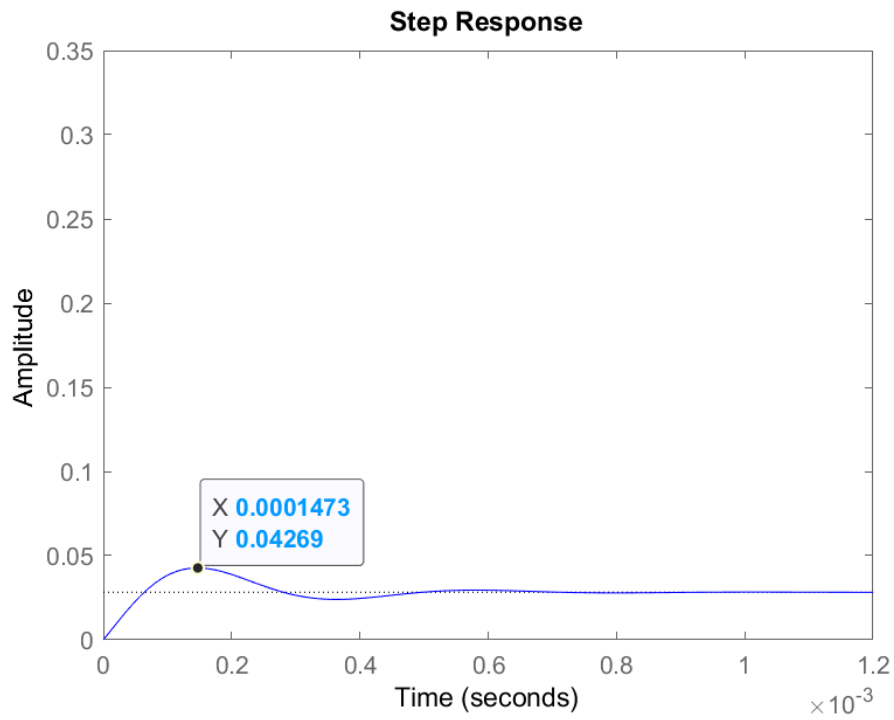
Moreover, it should be noted that the induced output voltage ripples cannot be

simply solved by adding a large capacitor to the output of the power converter. Because a large output capacitor will reduce the converter dynamic response speed, so it will have a negative performance on the control transient performance.

On the contrary, Figure 3.5(c) shows the waveforms of the duty cycle to the switch of SRC, battery current (I_B), battery voltage (V_B) and output voltage (V_O). The ripples of the output voltage of the proposed SRC method is only 50 mV, which is around 0.7% of the corresponding DC output voltage. Compared with 849 mV (13%) of the conventional duty-cycle perturbation method (see Figure 3.5(b)), the output ripples are significantly reduced by the proposed method. Moreover, it can be observed in Figure. 3.5(b) and Figure 3.5(c) that the large spike of battery current/voltage in the conventional duty-cycle method during the transient switching is automatically eliminated in the proposed method due to the adoption of the 10Ω resistor.

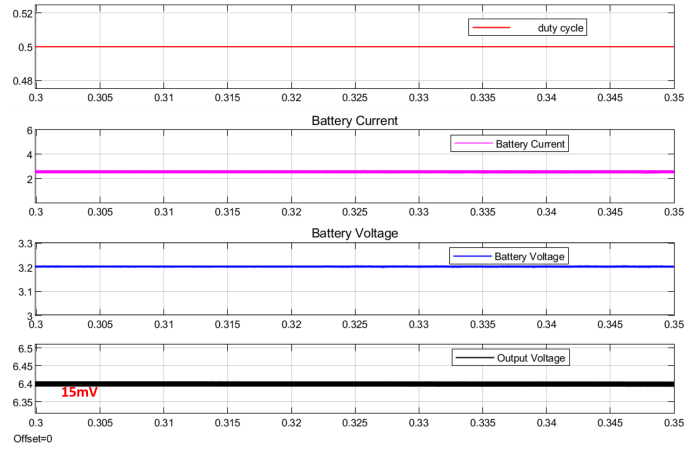


(a)

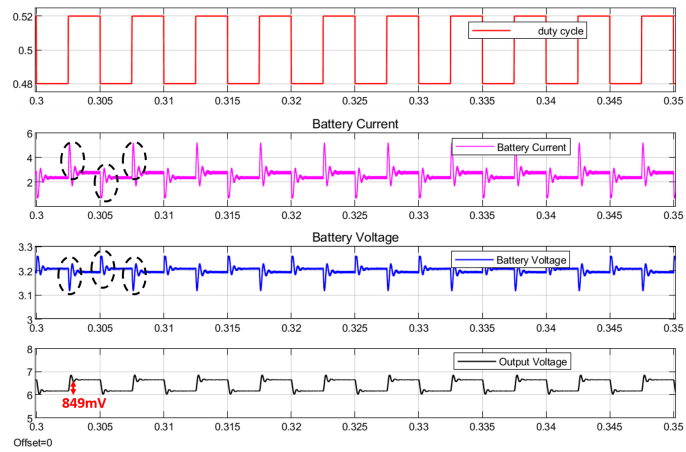


(b)

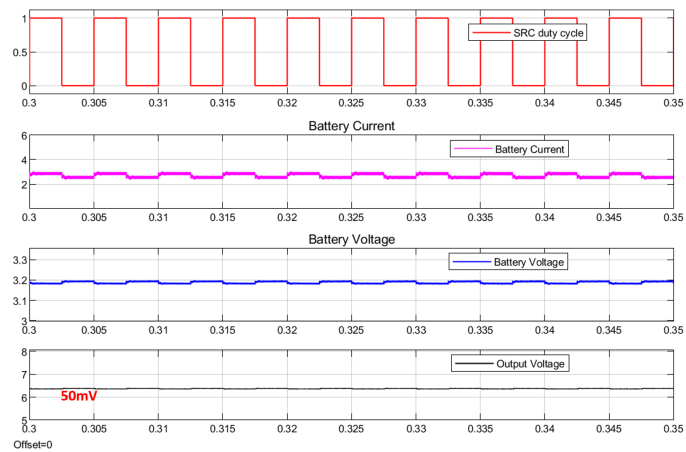
Figure 3.4 : (a) Step response of $v_{o,ac}$ due to $\frac{d_{ac}}{2}=0.02$ (b) Step response of $v_{o,ac}$ due to $v_{B,ac}=0.015$.



(a)



(b)



(c)

Figure 3.5 : (a) Waveforms of converter under normal power delivery mode (no perturbation) (b) Waveforms of the converter under impedance measurement mode with duty-cycle perturbation (c) Waveforms of the converter under impedance measurement mode with the proposed SRC perturbation method.

Table 3.2 : Battery perturbation signals and output voltage ripples comparison

	\hat{d}_{ac}	Perturbed Current(A)	Perturbed Voltage(V)	Output Ripples (V)	THD
No Perturbation	0	0	0	0.015	0.1%
Duty Cycle Method	0.01	0.1095	0.00355	0.471	2.77%
	0.015	0.1648	0.00533	0.681	4.14%
	0.02	0.2201	0.00712	0.849	5.48%
Proposed SRC method	0	0.2786	0.009	0.050	0.25%

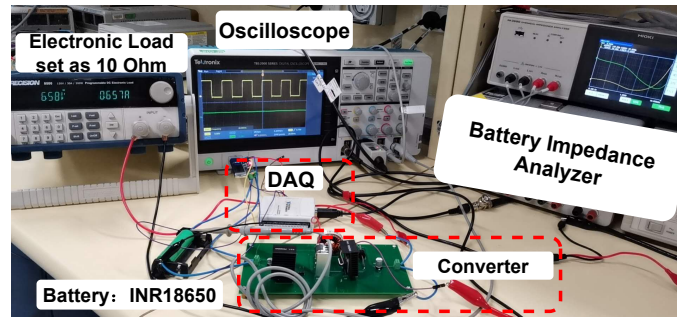


Figure 3.6 : Experimental bench.

3.6.5 Experimental Verification of Output Voltage Ripples Reduction in Proposed SRC Method

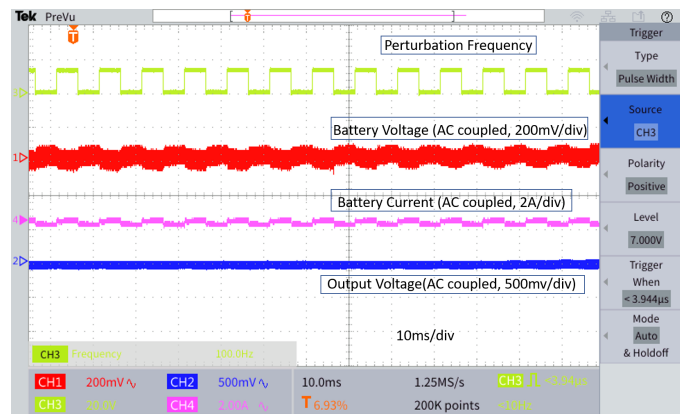


Figure 3.7 : The experimental waveforms of the proposed SRC perturbation method.

As discussed in Sections 3.6.3 and 3.6.4, the output ripples of the proposed method is around 16 times smaller than the duty-cycle perturbation method both in theoretical analysis and simulation. Therefore, the final experimental verification results will be given in this section, as shown in Figure 3.6, and the experimental platform specifications are shown in Table 3.3.

Figure 3.7 shows the sample waveforms for the PWM voltage of the SRC, battery voltage, battery current and the output voltage of the power converter of the proposed SRC perturbation method under 100Hz perturbation frequency. It can be

Table 3.3 : Main Specification of the Experimental Prototype

Design Parameter	Value
Battery	INR18650
Duty Cycle D	0.5
SRC Resistor R_1	10Ω , 3W
SRC switching Duty Cycle D_1	50%
Inductor L	$4.7\mu\text{H}$
Capacitor C	$220\mu\text{F}$
Operation frequency	150kHz

found that the proposed SRC method has smaller output ripples as compared with the duty-cycle perturbation method. In [6], the duty-cycle perturbation has induced large output voltage ripples which are around 0.38V. But in the proposed method, the output voltage ripples induced by the SRC perturbation is only around 0.02V, which is around 19 times smaller than the conventional duty-cycle perturbation method.

3.7 Battery Impedance Measurement Validation

After validating experimentally the low ripple battery impedance measurement in Section 3.6, this section will validate that the proposed SRC perturbation method can accurately measure online battery impedance.

3.7.1 Battery Multi-frequencies Impedance Calculation Algorithm

As illustrated in Figure 3.2, the voltage and current signals under the impedance measurement mode consist of DC components and small periodic odd-square waves alternating at f_p , which are composed of infinite sine waves with odd-integer har-

monic frequencies. By applying the Fourier expansion to the square functions of voltage and current over time t , the square perturbations can be represented as:

$$x(t) = \frac{4A}{\pi} \left(\sin(\omega t) + \frac{1}{3} \sin(3\omega t) + \frac{1}{5} \sin(5\omega t) + \dots \right) \quad (3.21)$$

where A is the amplitude of the signal (battery voltage and current) and ω is equal to $2f_p\pi$.

The data acquisition (DAQ), which has an analog-to-digital converter (ADC), is used to sample battery current and voltage. The discrete-time Fourier transform (DTF) is utilized to convert the voltage and current from the time domain to the frequency domain, which can be expressed as:

$$X_f = \sum_{n=0}^{N-1} x_n \cdot e^{-\frac{j2\pi}{N} f_p n} = \sum_{n=0}^{N-1} x_n \cdot \left[\cos \frac{2\pi f_p n}{N} - i \cdot \sin 2 \frac{f_p n}{N} \right] \quad (3.22)$$

where X_f is the value of the voltage or current at frequency f_p , N is the sampled number of voltage or current, n is the present voltage or current of the calculation moment (from 0 to $N - 1$), x_n is the current or voltage at n . After DTF processing, the impedance plot under the perturbation frequency and its odd-harmonic frequencies can be calculated by

$$Z_{\text{bat}}(f_p, 3f_p, 5f_p \dots) = \frac{V_B(f_p)}{I_B(f_p)} e^{j\theta_z(f_p)} \quad (3.23)$$

where $V_B(f_p)$ and $I_B(f_p)$ are the amplitudes of battery voltage and current at frequency f_p respectively, and $\theta_z(k)$ is the phase difference between voltage and current at frequency f_p .

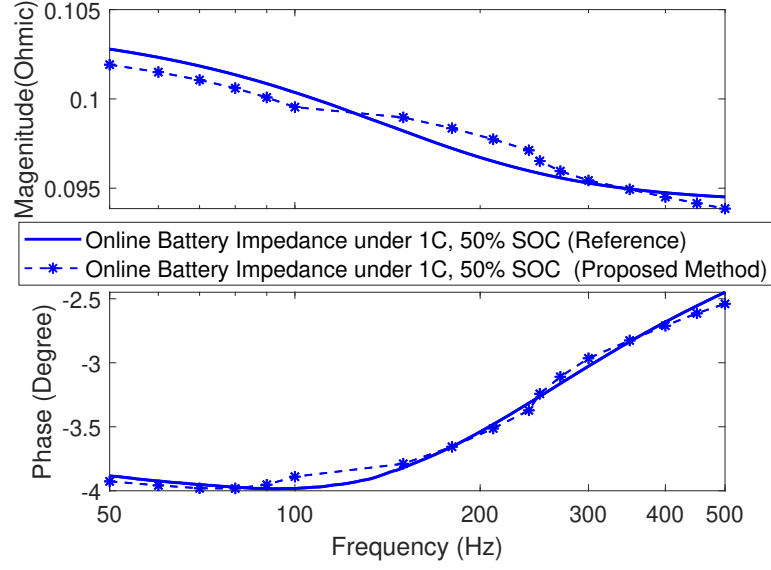


Figure 3.8 : Online battery impedance under 50% SOC, 1C discharge current rate.

3.7.2 Online Battery Impedance Test at 50% SOC, 1C Discharge Current Rate

When the battery works in the online measurement mode, the battery is connected with the power converter to deliver the power to the load. Therefore, the perturbation current is superimposed over a dc current passing through the battery. The battery current and voltage are sampled and stored by a DAQ named NI 6009 with a 14-bit, 48kS/s sampling rate. A commercial battery impedance analyzer (Hoiki IM3590) is connected to the battery terminal to conduct a reference experiment on a 50 % SOC battery with 1C superimposed dc current. Because the excitation signal of the commercial battery impedance analyzer is a sinewave, it needs a long measurement time (up to several minutes) to obtain the impedance under low-frequency region. This long measurement time can induce a SOC change to the battery. Therefore, the measured impedance will be inaccurate. To avoid this issue, the measurement frequency is chosen from 50 to 500 Hz, which contains important battery information and has a very short measurement time. For higher

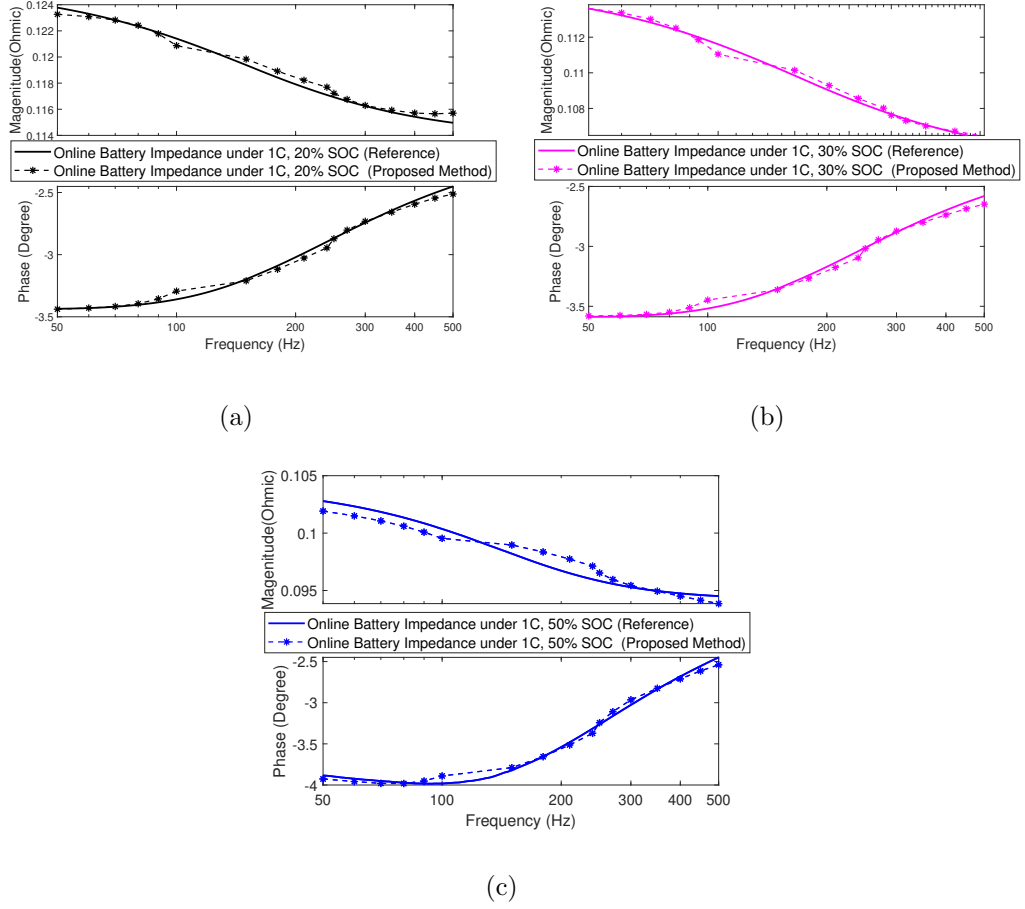


Figure 3.9 : Online battery impedance results (50Hz to 500Hz) under different SOC values (a) under 1C, 20% SOC (b) under 1C, 30% SOC (c) under 1C, 50% SOC.

measurement reliability, a simple filter is adopted to check the each data point is keeping at its surrounding data points region. The filter design method is reported by [74, 75].

To validate the correctness of the proposed method, six perturbation frequency values at 50Hz, 60Hz, 70Hz, 80Hz, 90Hz, and 100Hz are selected to implement in this experiment. One example under 100Hz perturbation frequency is given in Figure 3.7. The impedance at these six frequencies and their harmonic frequencies (from 50Hz to 500Hz) can be obtained by applying DTF elaborated in Section 3.7.1. Theoretically, only 0.0846 second ($\frac{1}{50} + \dots + \frac{1}{100}$) is needed to measure the all signals. From the

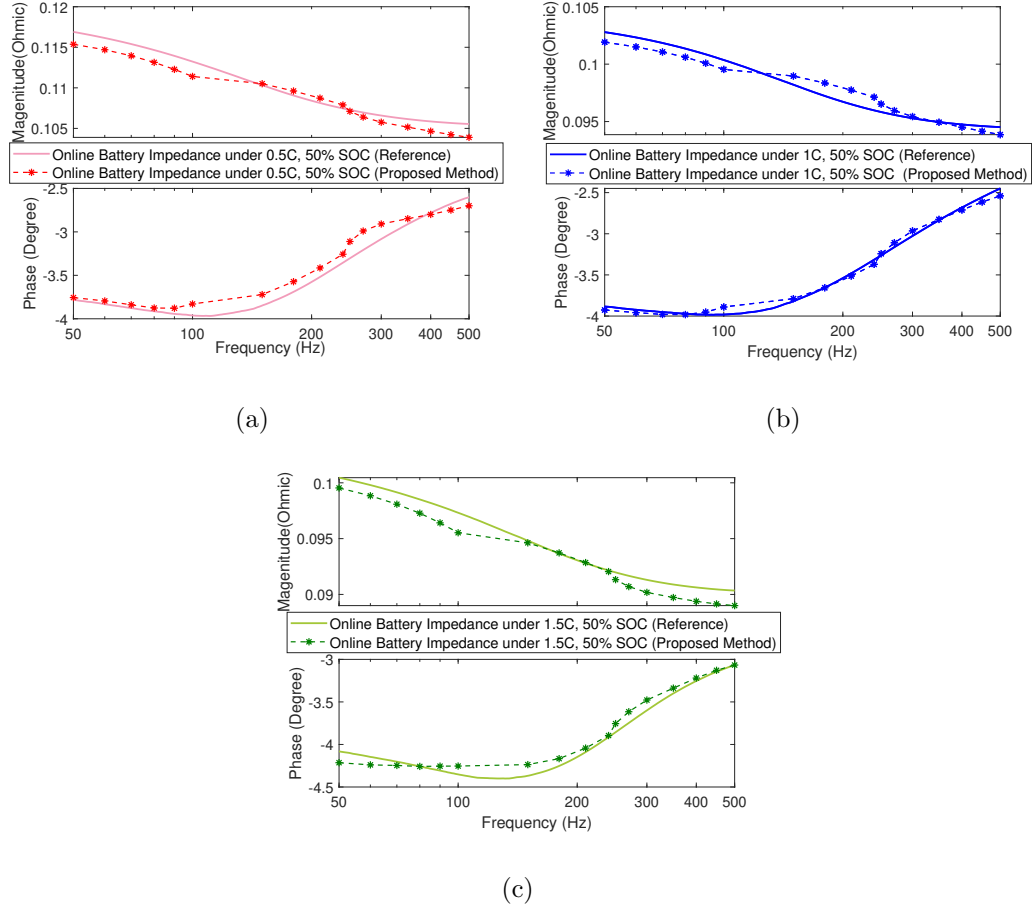


Figure 3.10 : Online battery impedance results (50Hz to 500Hz) under different discharge current rates (a) under 0.5C, 50% SOC (b) under 1C, 50% SOC (c) under 1.5C, 50% SOC.

DFT perspective, more data points can achieve a higher measurement accuracy. Therefore, ten-cycle data under one frequency is set as an experimental unit, and the total test time is 0.846 second. Figure 3.8 shows the battery impedance results measured under 50% SOC, 1C dc discharge current by the impedance analyzer (as the reference) and the proposed SRC perturbation method. As seen from this figure, the proposed SRC perturbation method is able to measure the impedance of a battery with a high correlation with a commercially available high precision impedance analyzer.

3.7.3 Online Battery Impedance Tests at Various Battery SOC

The battery is tested under different SOC values to confirm the capability of the proposed impedance measurement method. As it can be seen from the Figure 3.9, the comparison of the online battery impedance obtained under 20%, 30%, and 50% SOC values by the impedance analyzer (as the reference) and the proposed SRC perturbation method, respectively. The experimental results show a good match, the overall measurement error between the reference and the proposed method is less than 5%. Moreover, the overall trend of the experimental results show that the magnitude of battery impedance in the low SOC region is larger than the middle SOC range. And it can be found that with the increase of the frequency, the phase of the battery impedance shows an increase trend.

3.7.4 Online Battery Impedance Tests at Various Discharge Current Rate

Since the charge transfer polarization decreases with the increase of current [76], it is necessary to confirm that the proposed method can work correctly at different load conditions. In this section, the battery is tested under different operation currents, which are 0.5C, 1C, and 1.5C dc current rates, respectively.

Figure 3.10 shows the comparison of the online battery impedance obtained under 0.5C, 1C, and 1.5C discharge currents by the reference method and the proposed method, respectively. The results show a good match, the overall measurement error is less than 5%. The overall trend is that the battery impedance decreases with the increase in the current rate. More specifically, there is a 4.5 m Ω increment from 0C to 0.5C, a 16 m Ω increment from 0.5C to 1.0C, a 2.4m Ω increment from 1.0C to 1.5C.

In [6], the authors state that impedance is not affected by the current rate. However, it shows otherwise from the results of this work, which show the battery

impedance is significantly dependent on the discharge dc current rate. And the conclusion of this work is consistent with the definition of Butler-Volmer equation, which indicates that both charge transfer and diffusion polarizations are related to the current [76].

3.8 Summary

In this chapter, an efficient online battery impedance measurement method with reduced converter output voltage ripples has been proposed. This work consists of two main contributions. The cause of the output ripples in the conventional duty-cycle perturbation method has been analyzed. Based on the analysis and proof, a low ripple solution by changing the perturbation source from the main switch of the converter to the input of the converter through a small switched resistor circuit (SRC) has been proposed and verified in the first part of the paper. Theoretical analysis, simulation and experimental results show that the output ripples of the proposed SRC perturbation method is 16 times smaller than the conventional duty-cycle perturbation method. The second part of this chapter uses a SRC-integrated boost converter to validate that the proposed approach has a high impedance measurement accuracy, and the results show that the overall measurement impedance error is less than 5% under different discharge current rates and battery SOC values as compared with a commercial impedance analyzer.

Chapter 4

Sensorless Battery Surface Temperature Estimation

4.1 Introduction

As the discussion in chapter 1, temperature acquisition, which belongs to the signals measurement system, is one of the most important battery management system functions [77, 78]. To achieve thermal monitoring, avoid over-temperature, and update temperature-dependent parameters, the battery temperature should be well monitored. The battery needs to work under an allowable temperature range, which is normally between -20°C and 50°C . Moreover, the lithium-ion battery is sensitive to temperature variations, so it is necessary to update battery parameters with the temperature change. For example, the available battery capacity becomes smaller with the decreasing ambient temperature. In general, the temperature measurement is used for three conditions: stand-still storage, charging, and discharging. Typically, the battery surface temperature can be directly measured by temperature sensors. Commonly used temperature sensors for battery temperature measurement are Negative Temperature Coefficient (NTC) (metal oxide) or Positive Temperature Coefficient (PTC) (semiconductor type) [34]. The resistance will change as a function of the temperature, so the voltage drop across the sensor is an indicator of the temperature. This type of sensor is relatively cheap, but it will lose its linear characteristic in high and low-temperature regions. Moreover, digital interfaced sensors are also common. This type of sensor can be easily connected to a micro-controller.

However, the sensors installation, cabling, and signal acquisition will increase

the cost and decrease the system reliability as these additional components are also prone to failure [78].

4.1.1 Related Works and Research Gap

Some sensorless battery temperature estimation methods have been proposed [77–80]. For example, an equivalent circuit-based method has been proposed in [79]. In this method, a reduced-order battery thermal circuit and a Kalman filter were adopted to estimate the temperature. This method, however, requires the comprehensive pre-knowledge of the cell thermal characteristics, thermal boundary conditions, and heat generation rates. Other typical methods, which use the electrochemical impedance spectroscopy of the battery to estimate the battery surface temperature, have been proposed [78, 80]. These methods utilized the relationship between the temperature and battery impedance, which can be calculated by injecting a small ac current to the battery and observing its corresponded voltage response. However, this category methods will increase the complexity of the hardware design.

The neural network-based method, which can treat the battery as a black box and only utilize the available sampled data to estimate the temperature has offered an alternative solution. Recently, a sensorless surface temperature estimation method using the traditional feedforward neural network (FNN) has been proposed [77]. Nevertheless, there are two problems associated with this work. First, the battery surface temperature under the present time is influenced by the temperature of the past sample time. But the FNN lacks the ability to memorize previous information. Second, this model only validated the temperature estimation accuracy under constant-current constant-voltage (CCCV) charging conditions or constant current (CC) discharging conditions at room temperature. The challenging tasks to estimate the battery temperature are the dynamic load and changing temperature.

To overcome these issues, a recurrent neural network with gated recurrent unit

(GRU-RNN), which can make use of important historical information, is proposed in this chapter for estimating the battery surface temperature, as shown in Figure 4.1. Noted that the battery thermal model is a complex nonlinear system and battery surface temperature is a time-sequence task. Compared to the previous FNN method, the proposed GRU-RNN method can exploit information of the past temperature and measurement signals because its internal structure has memorised gates. The main contribution of this work are given as:

(1) This chapter builds the theoretical gap between the battery temperature distribution and RNN by proving that the battery temperature distribution is a time-sequence task.

(2) A GRU-RNN mode, which is good at time-sequence task modeling, is first proposed to estimate battery surface temperature.

(3) The proposed GRU-RNN model can achieve high accuracy under real EV operational driving profiles with various ambient temperature.

4.2 Battery Temperature Distribution is a Time-Sequence Task (Theoretical Analysis)

A commonly adopted expression for the heat generation (Q) in a lithium-ion battery is

$$Q = I(V_B - OCV) + IT_c \frac{\partial OCV}{\partial T_c} \quad (4.1)$$

which is a simplified equation proposed by Bernardi *et al.* [81]. The first term at the right side is the heat generated by the ohmic resistance, charge transfer overpotential, and mass transfer limitations [79]. I and V_B are the current and terminal voltage of the battery, which can be directly measured online by physical sensors. OCV , which is the open-circuit voltage of the battery under an inner-

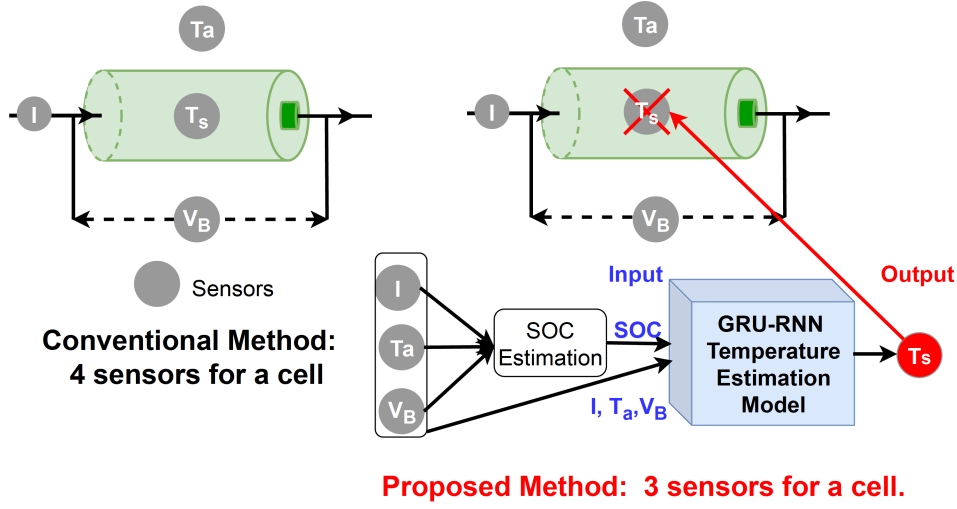


Figure 4.1 : Conventional battery surface measurement method (left), which has four sensors: voltage sensor, current sensor, battery surface temperature sensor, and ambient temperature sensor; the proposed sensorless surface temperature estimation method (right), which only has three sensors: voltage sensor, current sensor, and ambient temperature sensor

equilibrium-state, has a one-to-one relationship with battery state of charge SOC ($OCV = f(SOC)$). Because the variation of OCV within a short sample time is small. The second term is the entropic heat, which can be neglected for a simplified calculation due to its small value.

A battery thermal model is used to express the relationship between heat generation and battery temperature [79]. The heat generated inside the battery (Q) will cause the temperature rise both in the core (T_c) and surface (T_s) of the battery, as given in differential equations below:

$$\begin{aligned} C_c \frac{dT_c}{dt} &= Q - \frac{T_c - T_s}{R_{cs}} \\ C_s \frac{dT_s}{dt} &= \frac{T_c - T_s}{R_{cs}} - \frac{T_s - T_a}{R_{sa}} \end{aligned} \quad (4.2)$$

in which C_c and C_s are the battery heat capacity of the core and surface, T_c and T_s

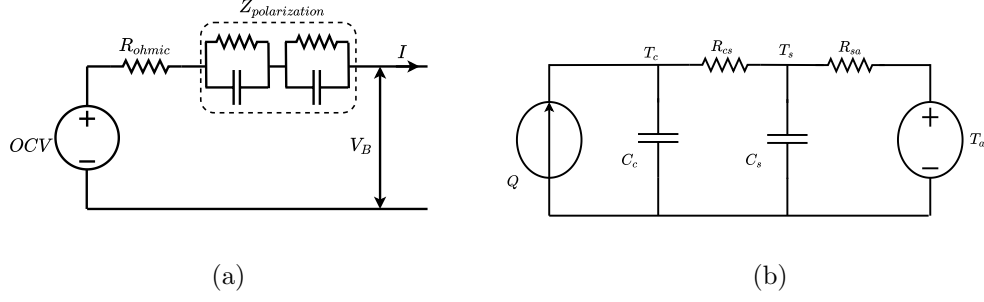


Figure 4.2 : (a) Battery equivalent electric model. (b) Battery equivalent thermal model.

are the battery temperature of the core and surface, T_a is the ambient temperature, R_{cs} is the core-to-surface resistance of the battery, and R_{sa} is the surface-to-ambient resistance of the battery.

Based on above analysis, it can be known that the battery surface temperature under the present moment ($T_{s,k}$) is related to inherent chemical characteristics of the battery (C_c , C_s , R_{cs} , and R_{sa}), operational signals under the present moment ($V_{B,k}$, I_k , OCV_k , and $T_{a,k}$), and the temperature of the previous sample time ($T_{s,k-1}$). SOC_k is used to represent OCV_k for heat analysis ($OCV_k = f(SOC)_k$). Therefore, the RNN, which can learn sequentiality and remember previous information, should be adopted [82].

4.3 Proposed GRU-RNN Sensorless Battery Temperature Estimation Method

Figure.4.3 illustrates the basic working principle the GRU-RNN, which has a feedback loop and allowing past information to persist [83]. The output of the system (T_s) is decided by the input and the historical information, which can be called the hidden state (h).

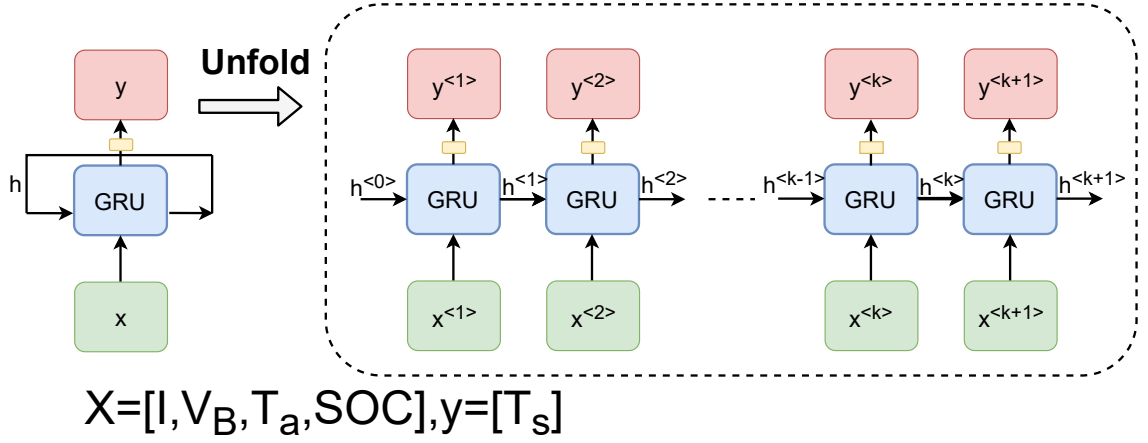


Figure 4.3 : Illustration diagram of GRU-RNN principle: x is the input vector, GRU is the GRU cell, h is the hidden state, and y is the output vector

$$h^{<k>} = \begin{cases} 0, & k = 0 \\ f(h^{<k-1>}, x^{<k>}), & \text{otherwise} \end{cases} \quad (4.3)$$

where $x^{<k>}$ is the input vector ($V_{B,k}$, I_k , SOC_k , and $T_{a,k}$) at the time step k , f is the nonlinear function, $h^{<k-1>}$ and $h^{<k>}$ are old and new hidden state, respectively. To further explain the working principle, Figure 4.4(a) introduces the internal structure of GRU cell, and explains how the GRU cell memorises the historical information. The first step is to calculate the relevance of the previous cell state to the present cell state by using a sigmoid activation called relevance gate, which can be expressed as follows:

$$r^{<t>} = \sigma(W_r \cdot [h^{<k-1>}, x^{<k>}]) \quad (4.4)$$

The update gate ($z^{<k>}$) is used to decide the portion of the previous state should be retained:

$$z^{<k>} = \sigma(W_z \cdot [h^{<k-1>}, x^{<k>}]) \quad (4.5)$$

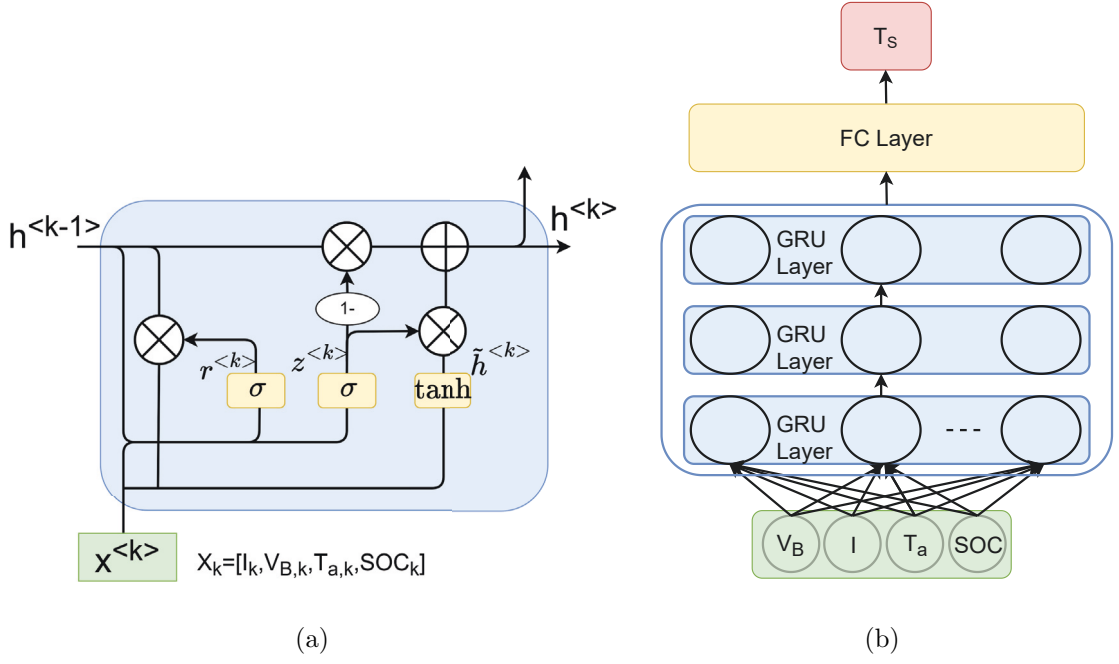


Figure 4.4 : (a) GRU cell structure. (b) Overall structure of the proposed GRU-RNN model

Similar to the relevance gate, the update gate is also a sigmoid activation, and the update method of the cell state is given below:

$$\tilde{h}^{<k>} = \tanh \left(W \cdot \left[r^{<k>} * h^{<k-1>}, x^{<k>} \right] \right) \quad (4.6)$$

$$h^{<k>} = (1 - z^{<k>}) * h^{<k-1>} + z^{<k>} * \tilde{h}^{<k>} \quad (4.7)$$

where $\tilde{h}^{<k>}$ is the candidate cell state, $h^{<k>}$ is a final filtered cell state, which is also the output value. For GRU cell, if the entry of $z^{<k>}$ is close to 1, the present state relies more on the candidate cell state, which is influenced by the present input, and the present state will depend more on the previous state if the entry is close to 0.

After explaining the advantages of the GRU-RNN for solving the sequence task, the whole structure of the proposed GRU-RNN model for battery surface temper-

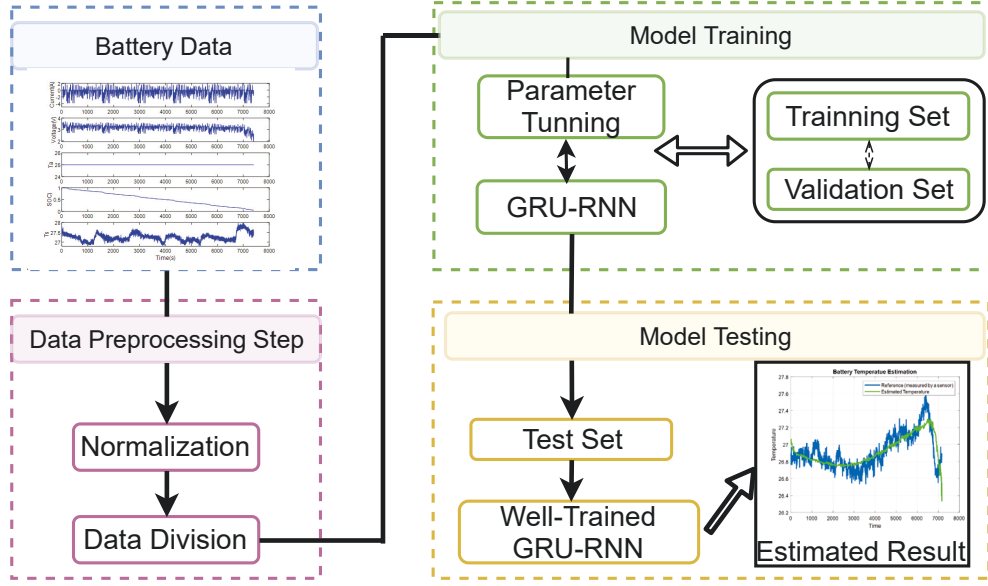


Figure 4.5 : Experimental procedure for GRU-RNN model training and temperature estimation.

ature estimation is given in Figure 4.4(b). The model starts with a sequence input layer, in which the measured signals including battery voltage, battery current, battery SOC, and ambient temperature formed an input vector $x^{<k>} = [V_{B,k}, I_k, SOC_k, T_{a,k}]$. Then, a following GRU layer is used to learn the dependence on previous input. In each step k , the GRU cell is updated by (7)-(10). Finally, a fully connected layer and a regression output layer are adopted to generate the final output: surface temperature ($T_{s,k}$). The details about how to optimize the hyperparameters of the GRU-RNN for training and how to evaluate the model performance are given in Section 4.4.3.

4.4 Experiment and Result Discussion

4.4.1 Platform for Data Collection

The experimental data of this chapter is a open data-set collected from the Center for Advanced Life Cycle Engineering (CALCE) of the University of Maryland [84].

A temperature sensor is mounted near the center of the cell surface using thermal paste and tape [84]. The experimental platform consists of a battery tester (Arbin BT2000), a climate chamber and a PC with Arbin software. The experimental cells are LiFePO_4 A123 18650 with 1.1 Ah nominal capacity and the operational voltage range is 2.0-3.6V.

4.4.2 Data Preparation and Experimental Procedure

To mimic the complicated and uncertain operations of EVs, two practical driving profiles are applied on batteries for testing: the Federal Urban Driving Schedule (FUDS) and the US06 Highway Driving Schedule [84]. In these tests, the battery cell is fully charged to 100% SOC at 3.6 V. And the specific dynamic profile is applied to the battery cell until reaching the batteries' cut-off voltage (2.0 V) over several cycles. Since the performance of the battery is highly influenced by the environmental temperature [84], it is necessary to repeat the experiment under different ambient temperature conditions (-10°C , 25°C , and 50°C). A typical data preparation method in machine learning field is adopted in this chapter. The whole data set is randomly divided into three inner groups, which are training (75%), validation (15%) and test (15%), respectively. Finally, the whole experimental procedure is explained in Figure 4.5.

4.4.3 Experiment: GRU-RNN Model Training and Evaluation

- i. **Model Training:** The hyperparameters setting decides the possible accuracy of the neural network. For a GRU-RNN model, the basic parameters are the number of layers and the number of hidden nodes per layer. Some advanced settings are the mini-batch size, the drop-out rate of the drop-out layer, and the learning rate of the model training. After carefully tuning these hyperparameters of the GRU-RNN, this chapter came out with a set of hyperparameters that provide the highest estimation accuracy with a high

computation efficiency, as shown in Table 4.1.

- ii. **Model Evaluation:** The model accuracy can be evaluated by three criterion: root mean square error (RMSE), mean absolute error (MAE) and max error (MAXE).

$$\text{RMSE} = \sqrt{\frac{1}{N} \sum_{k=1}^N \left(T_{s,k} - \hat{T}_{s,k} \right)^2} \quad (4.8)$$

$$\text{MAE} = \frac{1}{N} \sum_{k=1}^N \left| T_{s,k} - \hat{T}_{s,k} \right| \quad (4.9)$$

$$\text{MAXE} = \text{Max} \left| T_{s,k} - \hat{T}_{s,k} \right| \quad (4.10)$$

where N is the length of the dataset, $T_{s,k}$ and $\hat{T}_{s,k}$ are the real surface temperature measured by the temperature sensor and the model estimated surface temperature at time step k , respectively.

Table 4.1 : Hyperparameter setting.

GRU Layer	GRU node	Mini Batch	Optimizer	Learning Rate	Dropout Layer	Epoch
3	8	256	Adam	Initial 0.01; decrease rate=0.2 per 200 epoch	none	1000

¹ All experiments are conducted using Matlab 2020 on a computer with a single Intel(R) Core (TM)-i7-8550U CPU

4.4.4 Experimental Result Discussion

Figure 4.6 shows the measured, estimated temperature and estimated error with US06 and FUDS loading profiles under -10°C , 25°C and 50°C temperature conditions, respectively. For comparison, the detailed MAE, RMSE, and MAXE of the FNN and proposed GRU-RNN methods for two profiles under three ambient temperatures are described Table 4.2. It can be observed that the GRU-RNN model has achieved high accuracy result with the maximum MAE is 0.64°C while this value is 0.86°C in FNN under all six operational conditions. Especially for the US06 profile under -10°C , the GRU-RNN model shows the best performance, in which the MAE is 0.0749°C and the maximum error is only 0.2716°C . It should be noted that the estimation accuracy is reduced with the increase of the ambient temperature. Specifically, the average MAE of two profiles under -10°C ambient temperature is 0.1035°C , then the average MAE is 0.1049°C in 25°C ambient temperature and 0.1247°C in 50°C ambient temperature.

4.5 Summary

This chapter proposes a sensorless battery temperature estimation method using a GRU-RNN based on sensor-measured battery voltage, current and ambient temperature signals. First, this chapter analyzes that the temperature distribution of the battery is a sequence task, and explains why the GRU-RNN is superior to FNN in sequence task. Second, the proposed sensorless GRU-RNN model is practically evaluated using dynamic driving profiles (US06 and FUDS) under different temperatures (-10°C , 25°C , and 50°C). Finally, experimental results show that the proposed GRU-RNN provided good temperature estimations under varying temperatures, with RMSEs within 0.19°C , MAEs within 0.14°C and MAXEs within 0.65°C .

Table 4.2 : Temperature estimation results with the proposed GRU-RNN and FNN

Profiles		US06		FUDS	
	Model	GRU-RNN	FNN	GRU-RNN	FNN
-10°C	MAE($^{\circ}C$)	0.1321	0.3200	0.0749	0.1406
	RMSE($^{\circ}C$)	0.1670	0.3822	0.0928	0.1819
	MAXE($^{\circ}C$)	0.4956	0.8646	0.2716	0.5818
25°C	MAE($^{\circ}C$)	0.0749	0.0898	0.1349	0.1013
	RMSE($^{\circ}C$)	0.0956	0.1103	0.1626	0.1361
	MAXE($^{\circ}C$)	0.3342	0.3156	0.4580	0.4826
50°C	MAE($^{\circ}C$)	0.1109	0.1023	0.1385	0.1369
	RMSE($^{\circ}C$)	0.1374	0.1387	0.1845	0.1778
	MAXE($^{\circ}C$)	0.4479	0.4616	0.6425	0.6610

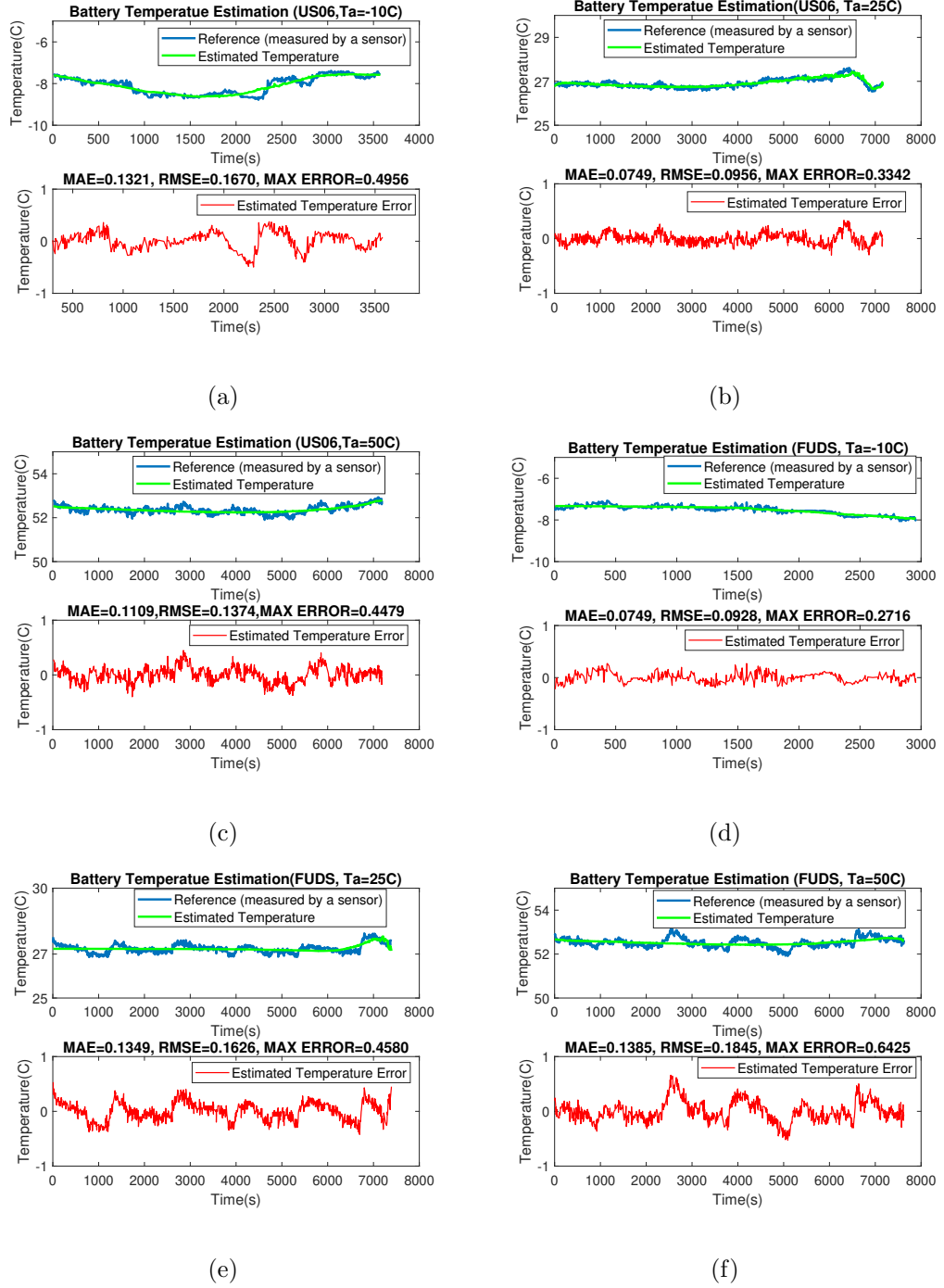


Figure 4.6 : Temperature estimation with GRU-RNN under different different loading profiles and temperature from: (a) US06 at -10°C ; (b) US06 at 25°C ; (c) US06 at 50°C ; (d) FUDS at -10°C ; (d) FUDS at 25°C ; (f) FUDS at 50°C

Chapter 5

Recurrent neural network based online SOC estimation

5.1 Introduction

As discussed in chapter 1, signal acquisition and state estimation are two important functions of the BMS. The signal acquisition function of BMS and a novel sensorless cell surface temperature estimation method are introduced in chapter 4. To continue improve the functionality of the BMS, related battery state estimation techniques will be introduced in this chapter. As aforementioned, the SOC estimation is one of the most important functions of BMS to ensure a safe and efficient operation. The battery SOC can be assumed to work like a fuel gauge in traditional fuel vehicles. Differing from traditional fuel gauges, however, the battery SOC must estimate rather than directly measure the remaining EV energy needs to determine the remaining useful energy of the battery [27].

Many lithium-ion battery SOC estimation methods have been proposed [27], which can be divided into four categories based on their working principles: (1) ampere-hour counting (AHC) method, (2) open-circuit voltage (OCV) method, (3) model-based (MB) method, and (4) data driven (DD) method.

The AHC method simply integrates the battery current over time. Although this method is easy to implement online, it needs to know the precise initial SOC, which is hard to obtain. Moreover, the measurement error from the current sensor is accumulated during the battery operation [47].

The second category is the OCV method, which utilizes the OCV-SOC rela-

tionship to estimate SOC. This method requires the battery to be idled for enough relaxation time to reach the internal equilibrium [85, 86]. Therefore, this method can be theoretically accurate but hard to implement practically.

The third category is the MB method, which uses electrical or electrochemical models to mimic battery performance. These methods have a correction feedback loop, which is the difference between the output of the battery models and on-line measured battery terminal voltage. By combining with this feedback, many algorithms can be employed to estimate SOC, such as PI [42, 48], sliding-mode observer [27], and Kalman filters [87, 88]. The MB methods are highly dependent on the accuracy of the battery model. However, the parameters of model components will change with battery degradation, temperature and current rate. Therefore, it still a challenge to obtain a stable and accurate model for online SOC estimation.

The fourth category is the DD method, which treats the battery like a black box to establish the relationship between the battery SOC and other measurable signals. Different methods are available to train the black box, such as support vector machines (SVM) [89] neural networks [44, 90–92], and multivariate adaptive regression splines (MARS) [93]. Unlike the MB methods, there is no need for comprehensive pre-knowledge of battery chemical characteristics in the DD methods. As the computation ability and achievement in machine learning increase, the neural network-based online SOC estimation method has gained more attention recently. In particular, the recurrent neural network (RNN) has generated interest for on-line SOC estimation due to its structure, which has advantages in sequence data processing [94–96]. Details of RNNs are elaborated in the remainder of this chapter.

5.1.1 Related Works for RNN-based SOC Estimation

This section introduces RNNs and discusses significant information found in recent publications.

An RNN has a closed-loop structure. Therefore, an RNN can automatically memorise and utilize past information. The key working principle of RNN is passing the output or an intermediate state of the previous time step as an input of the present time step. For example, SOC at time step $t-1$ is an input of the RNN at time step t . However, as pointed out by the neural network founder Benigo et al. [97], when the sequence gets longer, it is harder to train an RNN to capture long-term dependencies because of gradient vanishing or rare gradient explosion. More advanced RNNs were proposed to solve this limitation, such as the long short-term memory (LSTM), the gated recurrent unit (GRU), and the bidirectional RNN. These neural networks have advanced structures with gates, which can build the relationship between past to present data [44, 98]. The ability to retain past information makes the RNN model useful for time series or sequence tasks, such as speech recognition or the estimation of battery states [44, 99].

A combined SOC estimation method has been proposed in [90], which uses the LSTM-RNN to approximate the battery SOC, then uses an adaptive cubature Kalman filter (ACKF) to further improve estimation accuracy. The paper demonstrated that SOC estimation accuracy can be significantly improved by adopting ACKF compared with results from LSTM-RNN-only processes. Although this paper represents meaningful work, there is a problem with its experimental setting. Note that the accuracy of SOC estimation is highly dependent on the parameters of the RNN, which should be well designed. For [88], their parameter-setting process is comparatively simple and lacks sufficient tuning. Moreover, combining external filters with neural networks will increase the memory requirements and invite an extra computation burden for the embedded system.

Recently, a stacked bidirectional LSTM RNN (BiLSTM-RNN) model has been proposed in [92], and the authors have concluded that the BiLSTM-RNN structure is superior to other unidirectional RNNs by comparing SOC results. However,

there are two doubts about this conclusion. First, this model contains two stacked BiLSTM-RNN, which are equivalent to four unidirectional LSTM stacked layers. Since there is no experimental comparison between the two BiLSTM layers and four LSTM layers, it is unclear whether the accuracy improvement is caused by the bidirectional structure or the increase in layers. Second, the BiLSTM-RNN requires knowing the information at both the start and the end of the sequence. Unlike offline dataset testing, the online battery SOC estimation is a time-sequence task that lacks definite end data during the online battery operation. As a contributory work, [90] introduces a new neural network structure for battery SOC, yet some issues remain to be explained and empirically verified.

5.2 Models

As discussed in the introduction, different RNN models have been adopted to estimate battery SOC. However, there is a lack of fair comparison between the models. This section provides a comprehensive introduction to different RNNs, including the traditional RNN, LSTM-RNN, GRU-RNN and bidirectional RNN.

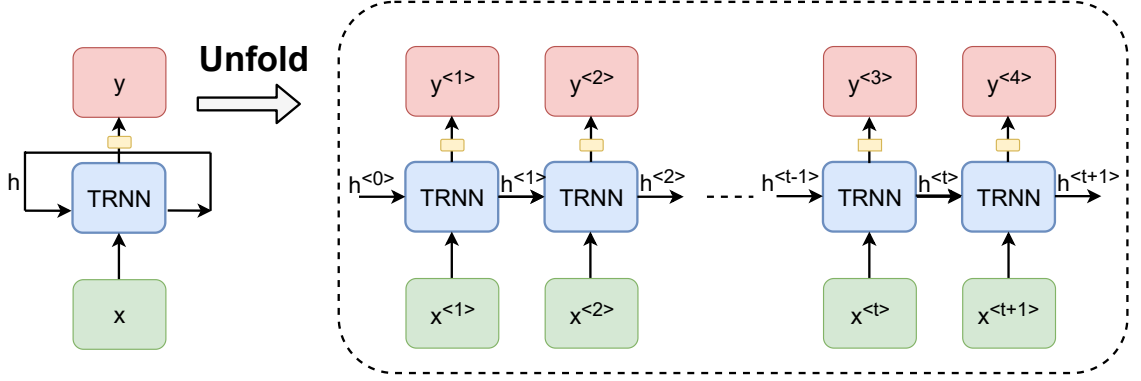
5.2.1 Traditional RNN

The first RNN was developed from the work of David Rumelhart in 1986. Figure 5.1(a) displays the basic architecture of an RNN, which has feedback loops that allow past information to persist [100]. Moreover, the present output of the system is decided by the present input and the historical memory, which can be called the hidden state (h), whose update function is expressed as follows:

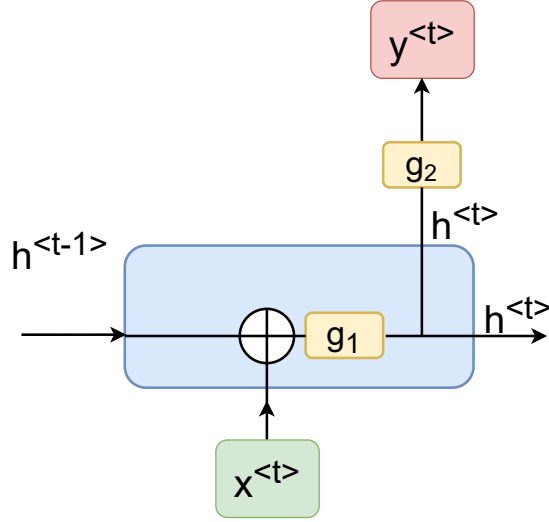
$$h^{<t>} = \begin{cases} 0, & t = 0 \\ f(h^{<t-1>}, x^{<t>}), & \text{otherwise} \end{cases} \quad (5.1)$$

where $x^{<t>}$ is the input vector (V, I, T) at the time step t , f is the nonlinear activa-

tion function, and $h^{<t-1>}$ and $h^{<t>}$ are the old and new hidden state, respectively.



(a)



(b)

Figure 5.1 : (a) Illustration diagram of RNN working principle; (b) Traditional RNN cell.

Figure 5.1(b) shows the internal structure of a traditional RNN cell, and its update function of the hidden state in (5.1) and the output function are given as follows:

$$h^{<t>} = g_1 (W_{hh} \cdot h^{<t-1>} + W_{hx} \cdot x^{<t>} + b_h) \quad (5.2)$$

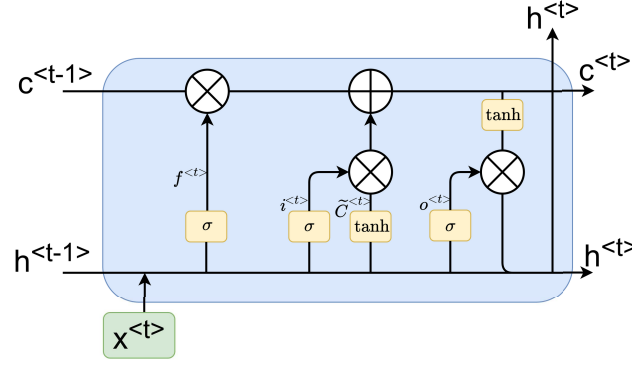


Figure 5.2 : LSTM cell structure

$$y^{<t>} = g_2 (W_{yh}h^{<t>} + b_y) \quad (5.3)$$

where W_{hh} , W_{hx} , W_{yh} are distinct weight matrix between layers, b_h and b_y are the bias parameter of the node, g_1 and g_2 are activation functions, and $y^{<t>}$ is the output (SOC) of the system.

One advantage of the RNN is that its computation can regard historical information. However, it is difficult to capture data from a long time ago when the input sequence lengthens due to gradient vanishing or rare gradient explosion [97]. This lengthening occurs because the multiplicative gradient exponentially decreases according to the numbers of layers. Advanced cell structures such as LSTM and GRU, which have adopted mechanisms called gates to reduce the gradient vanishing rate, have been proposed to overcome this problem.

5.2.2 LSTM-RNN

The LSTM-RNN, which is an improved RNN proposed by Hochreiter in 1997 [101], has a similar structure to the traditional RNN (see Figure 5.1(a)). The LSTM cell, however, has a different structure from a traditional RNN cell. As shown in Figure 5.2, three gates are used to decide whether the LSTM cell should

memorize the historical or input information. Moreover, the persistent information after calculation will be used to update the cell state ($\tilde{C}^{<t>}$), which behaves like a conveyor belt in LSTM-RNN.

The first step of the LSTM cell is to decide how much information should be deleted from the cell state. This decision is made by a sigmoid function called the forget gate ($f^{<t>}$), which can be expressed as follows:

$$f^{<t>} = \sigma (W_f \cdot [h^{<t-1>}, x^{<t>}] + b_f) \quad (5.4)$$

The second step is to decide how much information should be stored in the cell state. This step is divided into two parts: a sigmoid function named update gate decides which information should be updated. Next, a tanh function creates a candidate value ($\tilde{C}^{<t>}$) for further cell state operation:

$$\begin{aligned} i^{<t>} &= \sigma (W_i \cdot [h^{<t-1>}, x^{<t>}] + b_i) \\ \tilde{C}^{<t>} &= \tanh (W_C \cdot [h^{<t-1>}, x^{<t>}] + b_C) \end{aligned} \quad (5.5)$$

The third step is to update the cell state from the previous state ($C^{<t-1>}$) to the new state ($C^{<t>}$):

$$C^{<t>} = f_t * C^{<t-1>} + i^{<t>} * \tilde{C}^{<t>} \quad (5.6)$$

The fourth step of the cell computation is to decide what the output is, which is based on the cell state ($\tilde{C}^{<t>}$) but is a filtered version. This step is also divided into two parts: a sigmoid function named output gate decides which information should become the output, then a tanh function is used to process the cell state, and its output value is multiplied with the result of the output gate ($o^{<t>}$).

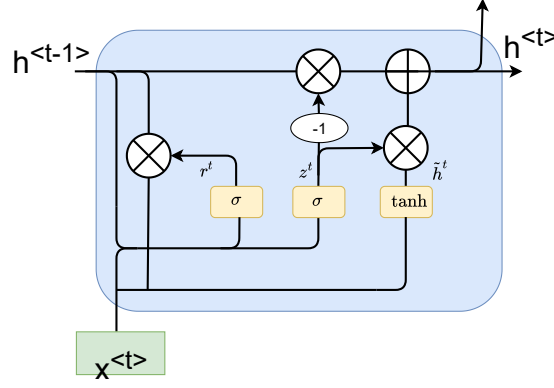


Figure 5.3 : GRU cell structure

$$\begin{aligned} o^{<t>} &= \sigma(W_o \cdot [h^{<t-1>}, x^{<t>}] + b_o) \\ h^{<t>} &= o^{<t>} * \tanh(C^{<t>}) \end{aligned} \quad (5.7)$$

Finally, a fully connected layer and an output regression layer are used to perform a transformation from the hidden state $h^{<t>}$ to the required SOC estimation value ($y^{<t>}$) at time t , which is demonstrated as follows:

$$y^{<t>} = W_{yh} h^{<t>} + b_y \quad (5.8)$$

5.2.3 GRU-RNN

Like the LSTM cell, GRU-RNN was introduced to overcome the gradient vanishing issue of the traditional RNN, but with a simpler cell structure than the LSTM [98]. The GRU cell also has gates to modulate the flow of the information inside the cell; however, there is no separate memory cell. Figure 5.3 shows a graphical illustration of a GRU cell, and the detailed explanation is given below.

The first step of the GRU cell is to calculate the relevance of the previous cell state to the current cell state using a sigmoid activation called ‘relevance gate’ ($r^{<t>}$), which can be expressed as follows:

$$r^{<t>} = \sigma (W_r \cdot [h^{<t-1>}, x^{<t>}]) \quad (5.9)$$

The update gate ($z^{<t>}$) used to decide the portion of the previous state should be retained:

$$z^{<t>} = \sigma (W_z \cdot [h^{<t-1>}, x^{<t>}]) \quad (5.10)$$

Like the relevance gate, the update gate is also a sigmoid activation, making the GRU retain the cell state for a long time. Moreover, the update method of the cell state is given below:

$$\tilde{h}^{<t>} = \tanh (W \cdot [r^{<t>} * h^{<t-1>}, x^{<t>}]) \quad (5.11)$$

$$h^{<t>} = (1 - z^{<t>}) * h^{<t-1>} + z^{<t>} * \tilde{h}^{<t>} \quad (5.12)$$

where $\tilde{h}^{<t>}$ is the candidate cell state and $h^{<t>}$ is a final filtered cell state, which is also the output value of GRU.

5.2.4 Bidirectional RNN

Conventional RNNs are unidirectional and can only process data from a positive time direction. In comparison, a bidirectional RNN (BiRNN) can process the sequence data from both the forward and backward propagation due to its inherent double recurrent hidden layer structure, as shown in Figure 5.4. It has been proven that the BiRNN can behave better than unidirectional RNN in some scenarios such as translation and speech recognition [102].

The forward layer output sequence, \vec{h}_t , is calculated using inputs in a positive sequence, while the backward layer output sequence, \overleftarrow{h}_t , is calculated by using the

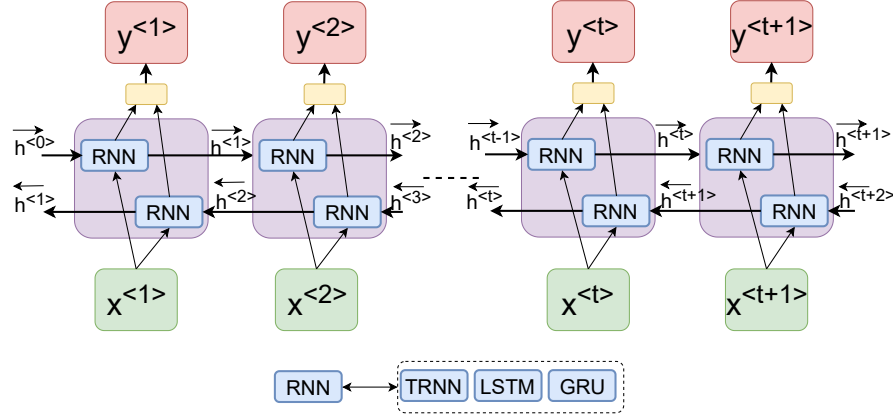


Figure 5.4 : Internal structure of BiRNN

reversed inputs. Finally, the BiRNN layer generates an output, $y^{<t>}$, which is given by

$$y^{<t>} = \sigma \left(\vec{h}^{<t>}, \overleftarrow{h}^{<t>} \right) \quad (5.13)$$

where the sigmoid function is used to merge these two output sequences. The forward and backward layers can be either LSTM or GRU structure, and the calculation process of LSTM and GRU have been elaborated above.

5.3 Experimental Setup

Figure 5.1(a) demonstrates the overall structure for how to utilize the battery data to train a neural network, which can be used for online battery SOC estimation. A detailed data process and algorithm setting are provided in this section.

5.3.1 Experimental Platform

The experimental data of this chapter is from the Center for Advanced Life Cycle Engineering of the University of Maryland [11]. The experimental platform consists of tested batteries, a battery tester (Arbin BT2000), a climate chamber, and a PC

with Arbin software, which can command the tester and record signals (current and terminal voltage) of the cells. The experimental samples are conventional 18650 NCM lithium-ion cells, whose specifications are given in Table 5.1.

Table 5.1 : Specifications of the batteries in the experiment

Sample Type	Material	Voltage Range / V	Capacity / Ah
INR18650	NCM	2.5-4.2	2.0

5.3.2 Experimental Data

To mimic the complicated and uncertain operations of EVs, a practical driving profile is applied on the battery for testing: the Federal Urban Driving Schedule (FUDS) [48]. According to the transferring principle defined by the US Advanced Battery Consortium (USABC), the dynamic profiles can be scaled down to the desired maximum demand based on the specifications of the test samples [48]. The operational time for one cycle of FUDS is 1372 s.

In the test, the battery cell is fully charged to 100% SOC and discharged to 80%, and then it is idled for relaxation. Moreover, the specific dynamic profile is applied to the battery cell until reaching the lithium-ion batteries' cut-off voltage, which is 2.5V. A selected example current/voltage/SOC curves of the battery under the FUDS profile at 45°C is shown in Figure 5.5.

A typical data preparation method in the machine learning field is adopted and briefly introduced in this chapter. The entire data set is randomly divided into three inner groups, which are training, validation and testing. Specifically, partial data (75%) is chosen to train the neural network, and the 15% data are used to validate the accuracy of the trained network during the training process. Once the model is

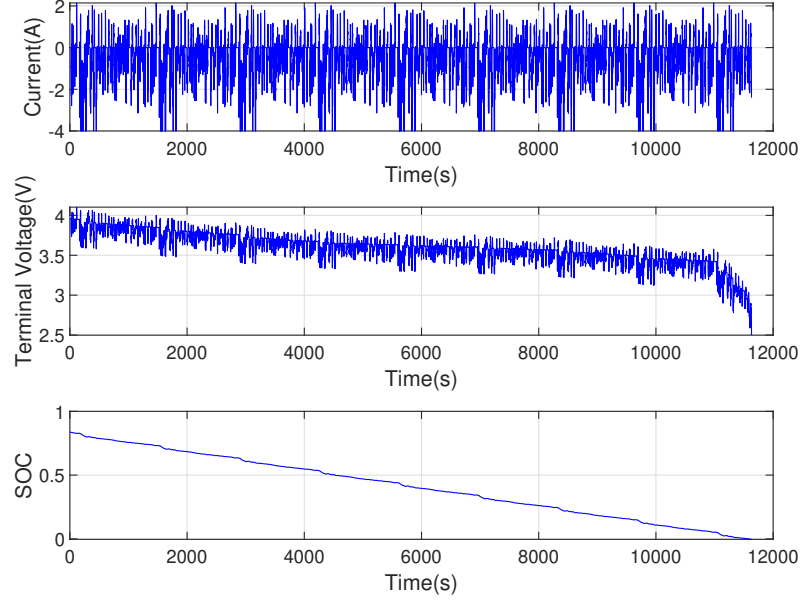


Figure 5.5 : FUDS drive cycle recorded at 45°C. The data are shown from the top to bottom: current, terminal voltage and SOC.

successfully trained, the remaining 15% data is used to test its estimation accuracy.

5.3.3 Experimental Procedure

- i. **Data Normalization:** The experimental dataset (one example is given in Figure 5.5) is a conventional raw dataset, which should be properly normalized before feeding into the neural network. A commonly used normalization equation is adopted in this work as follows:

$$x_{\text{norm}} = \frac{2(x - x_{\min})}{x_{\max} - x_{\min}} - 1 \quad (5.14)$$

where x_{\min} and x_{\max} are the minimum and maximum value of the battery dataset (voltage, current, temperature and SOC), and x is the related data at the present moment.

- ii. **Loss Function:** During the neural network training process, there is a loss function to measure the gap between the estimated battery SOC and real SOC. Also, the aim of the training process is to find a minimum point of this function. In this work, a conventional root-mean-square error (RMSE) is adopted as the loss function:

$$\text{RMSE} = \sqrt{\frac{1}{N} \sum_{t=1}^N \left(\text{SOC}_t - \widehat{\text{SOC}}_t \right)^2} \quad (5.15)$$

where N is the length of the dataset, SOC_t is the real SOC at moment t , and $\widehat{\text{SOC}}_t$ is the model estimated SOC at moment t .

- iii. **Network Setting:** This network setting decides the possible highest accuracy or loss of the neural network. For an RNN-based battery SOC estimation model, the most basic parameters are the type of RNN cell, the number of layers, and the number of hidden nodes per layer. Moreover, these three parameters have been extensively discussed in published works. However, some advanced settings, such as the batch size, have only been mentioned in a few papers. As this chapter aims to provide a comprehensive evaluation of RNNs on battery SOC estimation, all these parameter settings are elaborated with unbiased experimental results in Section 5.5.
- iv. **Network Evaluation:** Estimation accuracy is a vital factor for the trained neural network. Three criteria can be used to assess estimation accuracy: root mean square error (RMSE) and mean absolute error (MAE), and maximum MAE (MAXE).

$$\text{RMSE} = \sqrt{\frac{1}{N} \sum_{t=1}^N \left(\text{SOC}_t - \widehat{\text{SOC}}_t \right)^2} \quad (5.16)$$

$$\text{MAE} = \frac{1}{N} \sum_{t=1}^N |SOC_t - \widehat{SOC}_t| \quad (5.17)$$

$$\text{MAXE} = \text{Max} |SOC_t - \widehat{SOC}_t| \quad (5.18)$$

in which the accuracy validation is to compute the differences between the trained network estimated SOC and the real SOC. Normally, the smaller the error value, the higher the accuracy of the trained network.

5.4 Experimental Results and Discussion

All experiments are conducted using Matlab 2020 on a computer with a single Intel(R) Core (TM)-i7-8550U CPU. For a fair comparison, all networks are trained using the Adam solver for 1000 epochs.

5.4.1 Different Numbers of The Hidden Nodes

The hidden nodes of the RNNs refers to the dimensionality of the ‘hidden state’, which determines the ‘width’ of the RNNs. Deciding the number of hidden nodes is an essential part of evaluating the performance of the neural network. Using too few neurons in the hidden layers will result in an under-fitting problem, which means the hidden layers cannot adequately detect the signals from a complicated dataset. On the other contrary, having too many hidden nodes also can result in two problems: over-fitting and time-consumption. Various hidden node values are provided in different published works. For example, the authors have chosen 500 hidden nodes per layer in their LSTM-RNN structure [44]. Meanwhile, in [90], only 32 hidden nodes were selected for the LSTM-RNN model. Moreover, 150 and 64 hidden nodes have been selected in GRU-RNN and BiLSTM-RNN models, respectively [92].

Therefore, it is necessary to explore the effects of hidden nodes on model accuracy and determine an optimal hidden node value. Usually, the multiple consecutive

powers of 2 are widely used for choosing hidden nodes in the machine learning field [92], and this setting strategy is adopted in this chapter to set the number of hidden nodes of RNNs. This section provides the estimation accuracy comparison of LSTM-RNN, GRU-RNN, and BiLSTM-RNN under the same experimental setting. Note that one BiLSTM-RNN layer consists of two separate LSTM layers with different processing directions. Therefore, for a fair comparison, one BiLSTM-RNN equals two LSTM-RNNs or two GRU-RNNs. Table 5.2 lists the comparison results for each number of hidden neurons N_h of 32, 64, and 128. The results show that the LSTM-RNN model achieved the highest estimation accuracy under three conditions. Moreover, the BiLSTM-RNN did not shown a better performance when this type of model has the same layer value. In general, GRU-RNN, LSTM-RNN and BiLSTM-RNN have the best estimation performance with 64 hidden nodes.

Table 5.2 : Comparison results using different numbers of hidden nodes

Hidden Nodes	GRU-RNN			LSTM-RNN			BiLSTM-RNN		
	MAE (%)	RMSE (%)	MAXE (%)	MAE (%)	RMSE (%)	MAXE(%)	MAE (%)	RMSE (%)	MAXE (%)
32	1.91	2.28	5.91	1.75	2.10	5.64	2.38	2.88	9.18
64	1.87	2.24	5.93	1.72	2.06	5.35	2.29	2.77	7.82
128	1.93	2.30	5.69	1.71	2.07	5.06	2.33	2.81	8.66

Table 5.3 : Comparison results using different numbers of layers

Layers	GRU-RNN			LSTM-RNN			BiLSTM-RNN		
	MAE (%)	RMSE (%)	MAXE (%)	MAE (%)	RMSE (%)	MAXE (%)	MAE (%)	RMSE (%)	MAXE (%)
2	1.87	2.24	5.93	1.72	2.06	5.35	2.29	2.77	7.82
4	1.48	1.78	5.15	1.48	1.77	4.86	1.76	2.09	6.12

Table 5.4 : Comparison results using different numbers of mini-batch

Mini-Batch	GRU-RNN			LSTM-RNN			BiLSTM-RNN		
	MAE (%)	RMSE (%)	MAX-MAE (%)	MAE (%)	RMSE (%)	MAX-MAE (%)	MAE (%)	RMSE (%)	MAX-MAE (%)
128	1.47	1.80	5.32	1.45	1.73	4.62	1.71	2.05	5.51
256	1.48	1.78	5.15	1.48	1.77	4.86	1.76	2.09	6.12
512	1.50	1.81	5.48	1.49	1.79	4.61	1.78	2.11	5.47

5.4.2 Different Numbers of The Layers

The number of layers determines the ‘depth’ of the neural network model, and can directly affect the estimation performance. The different number of layers are summed to generate of a model for comparison. Section 5.5.1 has shown that neural network models with 64 hidden nodes have the best performance. Therefore, a layer with 64 hidden nodes is adopted for further comparison. This section provides the estimation accuracy comparison of the models with different numbers of LSTM-RNN, GRU-RNN and BiLSTM-RNN layers. The comparison results are given in Table 5.3. Note that two layers of LSTM-RNN and GRU-RNN are the same as one BiLSTM-RNN layer. From Table 5.3, it can be seen that a neural network with four layers has a higher estimation accuracy than a model with two layers.

5.4.3 Different Numbers of Mini-Batch

Some settings have been neglected in several previous works, such as the mini-batch [90,92]. In Sections 5.5.1 and 5.5.2, trained neural network models have default settings, which is explained as follows: the mini-batch is 256. The experimental results of Sections 5.5.1 and 5.5.2 have proven that a RNN with 4 layers and 64 hidden nodes has the best performance. In this section, three RNN models with 4 layers and 64 nodes are evaluated with different numbers of mini-batch, and the results are given in Table 5.4. It can be found that LSTM-RNN and BiLSTM-RNN have the best estimation performance when the mini-batch equals 128. For GRU-RNN, the model has the lowest MAE when the mini-batch equals 128. However, the model has the lowest RMSE and MAX-MAE when the mini-batch equals 256.

5.4.4 Result Discussion

After introducing the characteristics of different RNN-based SOC estimation methods, previous sections also offer brief experimental results, which can be found

in Tables 5.2, 5.3 and 5.4. The findings and summary of the experimental results are given in this section.

From the experimental results, it can be found that the performance of BiLSTM-RNN is not better than GRU-RNN and LSTM-RNN when they have the same numbers of layers. Moreover, the results show that the LSTM-RNN has the best estimation performance when the models have four layers with 64 hidden nodes and the model training mini-batch equals 128.

5.5 Summary

RNN, which has a time-sequence characteristic, has gain attention in sequence modelling and data processing. However, the structure of the traditional RNN dictates that it cannot capture long-term dependence features due to the vanishing gradient. More advanced RNNs, such as LSTM-RNN, GRU-RNN and BiRNN, have been proposed in different scenarios such as translation and speech recognition to overcome this problem. Since the SOC estimation process is a typical sequence-modelling task, many researchers have applied these advanced RNNs into battery SOC estimation, claiming that the model they adopted has more advantages than others. However, in the battery SOC estimation field, there is no detailed empirical evaluation of these advanced RNNs. In this chapter, detailed theoretical analysis and comparison of these advanced RNNs has been provided. Second, a systematic experiment-based evaluation under a practical driving profile (FUDS) has been applied to advanced RNNs. Third, a brief discussion about the SOC estimation of LSTM-RNN, GRU-RNN and BiLSTM-RNN under different settings is offered in this chapter.

Chapter 6

Conclusion

6.1 Conclusion

Motivated by the requirement of a high efficient, reliable, stable and safe operation with low cost for the lithium-ion batteries, this thesis proposed a series of techniques for lithium-ion batteries from parameter measurement, modelling, and states estimation perspectives.

Chapter 1 gave a brief introduction to the background, theory and management of lithium-ion batteries. The background section explained that the lithium ion battery is a necessary component for a green planet. The introduction to lithium-ion batteries described the working principle, different types, and equivalent models of lithium-ion batteries. The introduction to the BMS detailed the main functions of BMS: signal measurement, states estimation (SOC and SOH), cell balancing (passive balancing and active balancing).

Chapter 2 elaborated a rapid OCV measurement method, which utilizes OCBCP to reduce the initial polarization voltage and shorten the time for the battery to reach its equilibrium state for SOC estimation. A second-order relaxation model, which shows a good balance between accuracy and simplicity, was established for analyzing the relationship between current and polarization voltage. Furthermore, considering the safe operation of the battery and hysteresis voltage issue, a 1C bipolar-current pulse with six minutes' duration was chosen for implementation. The effectiveness of the proposed method was verified, and it save 30% to 90% relaxation time compared with that of the conventional incremental OCV method.

Chapter 3 proposed an efficient and accurate online battery impedance measurement method with reduced converter output voltage ripples. The cause of the large output ripples in the conventional duty-cycle perturbation method was analyzed. Based on the analysis and proof, a low ripple solution by changing the perturbation source from the main switch of the converter to the input of the converter through a small switched resistor circuit (SRC) was proposed and verified. Theoretical analysis, simulation and experimental results showed that the output ripples of the proposed SRC perturbation method are 16 times smaller than the conventional duty-cycle perturbation method. Moreover, a SRC-integrated boost converter was used to validate that the proposed approach can accurately measure the battery impedance. The experimental results showed that the overall measurement impedance error is less than 5% under different discharge current rates and battery SOC values as compared with a commercial impedance analyzer.

Chapter 4 proposed a sensorless battery temperature estimation method using a GRU-RNN based on sensor-measured battery voltage, current and ambient temperature signals. This chapter explained why recurrent neural networks can estimate battery temperature from the battery heat generation and temperature distribution perspective. The analysis showed that the heat generation and temperature distribution are a sequence task, which should be solved by an RNN. By considering the limitations of the RNN, a GRU-RNN, which has a simple internal structure and can handle the long-term sequential dependencies, was adopted and well-trained. Moreover, the proposed sensorless model was evaluated using dynamic driving profiles under different temperatures. Finally, the experimental results proved the high accuracy of the proposed method that the maximum error in the best and worst-case scenarios is 0.2716°C and 0.6425°C , respectively.

Chapter 5 gave a detailed theoretical analysis and comparison of several advanced RNNs (LSTM-RNN, GRU-RNN, and BiRNN). Moreover, a systematic experiment-

based evaluation under a practical driving profile has been applied to these advanced RNNs with different model settings for online SOC estimation. Third, a brief discussion about the influence of different RNNs and settings on SOC estimation accuracy was given in this chapter.

6.2 Future Work

There are several recommendations for future research.

- i. The rapid OCV measurement method in chapter 2 was developed with new battery cell under the room temperature. For future work, the proposed technique should be extended to the aging battery under different temperature conditions.
- ii. The proposed online battery impedance measurement method in chapter 3 was based on SRC at the input of the converter. It should be noted that the SRC shares the same structure of the passive balancing circuit. For future work, the passive balancing circuit will be used as SRC of the cell for the online impedance measurement. Therefore, the new measurement circuit will not increase the overall cost and size of the system.
- iii. The proposed sensorless surface temperature estimation method in chapter 4 was developed by the data of the single cell. Normally, the battery cells need to be connected in series and parallel to form into a battery pack, in which the battery surface temperature will be influenced by the thermal coupling among cells. In the future work, the GRU-RNN based temperature estimation in a battery pack will be comprehensively investigated.
- iv. This thesis has proved that the artificial intelligence based or neural network battery models can behave good both in surface temperature estimation task

and SOC estimation tasks. However, these models were evaluated by Intel CPU. For future work, the neural network battery model will be evaluated by the DSP, which is more practical for the real application.

Bibliography

- [1] EPA,
<https://www.epa.gov/ghgemissions/global-greenhouse-gas-emissions-data>,
 2017.
- [2] G. E. Outlook, <https://www.iea.org/reports/global-ev-outlook-2020>, 2020.
- [3] J. Li, N. Lotfi, R. G. Landers, and J. Park, “A single particle model for lithium-ion batteries with electrolyte and stress-enhanced diffusion physics,” *Journal of The Electrochemical Society*, vol. 164, no. 4, p. A874, 2017.
- [4] J. Qi and D. D.-C. Lu, “Review of battery cell balancing techniques,” in *2014 Australasian Universities Power Engineering Conference (AUPEC)*. IEEE, 2014, pp. 1–6.
- [5] B. University,
https://batteryuniversity.com/learn/article/battery_rapid_estimation_methods, 2017.
- [6] J. A. A. Qahouq and Z. Xia, “Single-perturbation-cycle online battery impedance spectrum measurement method with closed-loop control of power converter,” *IEEE Transactions on Industrial Electronics*, vol. 64, no. 9, pp. 7019–7029, 2017.
- [7] A. Ayachit and M. K. Kazimierczuk, “Averaged small-signal model of pwm dc-dc converters in ccm including switching power loss,” *IEEE Transactions on Circuits and Systems II: Express Briefs*, vol. 66, no. 2, pp. 262–266, 2018.
- [8] VOX, <https://www.vox.com/22175698/climate-change-treaty-trump-china-eu-uk-paris-agreement-biden>,

2020.

- [9] Aura, <https://www.cleanenergycouncil.org.au/resources/resources-hub/clean-energy-australia-report>, 2019.
- [10] L. Zheng, “Development of lithium-ion battery state estimation techniques for battery management systems,” Ph.D. dissertation, 2018.
- [11] F. Zheng, Y. Xing, J. Jiang, B. Sun, J. Kim, and M. Pecht, “Influence of different open circuit voltage tests on state of charge online estimation for lithium-ion batteries,” *Appl. Energy*, vol. 183, pp. 513–525, Dec. 2016.
- [12] IEA, [https://www.irena.org/-/media/Files/IRENA/Agency/Publication/2019/Sep/IRENA_Utility – scale – batteries2019.pdf](https://www.irena.org/-/media/Files/IRENA/Agency/Publication/2019/Sep/IRENA_Utility%20scale%20batteries2019.pdf), 2019.
- [13] F. Yang, X. Song, F. Xu, and K.-L. Tsui, “State-of-charge estimation of lithium-ion batteries via long short-term memory network,” *Ieee Access*, vol. 7, pp. 53 792–53 799, 2019.
- [14] C. Zou, “Modelling, state estimation & optimal charging control for a lithium-ion battery,” Ph.D. dissertation, 2016.
- [15] H. He, R. Xiong, and J. Fan, “Evaluation of lithium-ion battery equivalent circuit models for state of charge estimation by an experimental approach,” *energies*, vol. 4, no. 4, pp. 582–598, 2011.
- [16] J. C. Forman, S. Bashash, J. L. Stein, and H. K. Fathy, “Reduction of an electrochemistry-based li-ion battery model via quasi-linearization and pade approximation,” *Journal of the Electrochemical Society*, vol. 158, no. 2, p. A93, 2010.

- [17] J. Meng, G. Luo, and F. Gao, "Lithium polymer battery state-of-charge estimation based on adaptive unscented kalman filter and support vector machine," *IEEE Transactions on Power Electronics*, vol. 31, no. 3, pp. 2226–2238, 2015.
- [18] S. C. Hageman, "Simple pspice models let you simulate common battery types," *EDN*, vol. 38, no. 22, p. 117, 1993.
- [19] B. Wu and B. Chen, "Study the performance of battery models for hybrid electric vehicles," in *2014 IEEE/ASME 10th International Conference on Mechatronic and Embedded Systems and Applications (MESA)*. IEEE, 2014, pp. 1–6.
- [20] J. Feng, Y. He, and G. Wang, "Comparison study of equivalent circuit model of li-ion battery for electrical vehicles," *Research Journal of Applied Sciences*, vol. 6, no. 20, pp. 3756–3759, 2013.
- [21] C. Liu, W. Liu, L. Wang, G. Hu, L. Ma, and B. Ren, "A new method of modeling and state of charge estimation of the battery," *Journal of Power sources*, vol. 320, pp. 1–12, 2016.
- [22] G. L. Plett, *Battery Management Systems, Volume I: Battery Modeling*. Norwood, MA, USA: Artech House, 2015.
- [23] ———, *Battery Management Systems, Volume II: Equivalent-Circuit Methods*. Norwood, MA, USA: Artech House, 2015.
- [24] M. Greenleaf, H. Li, and J. P. Zheng, "Modeling of li $_{-}\{x\}$ fepo $_{-}\{4\}$ cathode li-ion batteries using linear electrical circuit model," *IEEE Transactions on sustainable energy*, vol. 4, no. 4, pp. 1065–1070, 2013.
- [25] W. Huang and J. A. A. Qahouq, "An online battery impedance measurement method using dc–dc power converter control," *IEEE Transactions on Industrial Electronics*, vol. 61, no. 11, pp. 5987–5995, 2014.

- [26] D. A. Howey, P. D. Mitcheson, V. Yufit, G. J. Offer, and N. P. Brandon, "Online measurement of battery impedance using motor controller excitation," *IEEE transactions on vehicular technology*, vol. 63, no. 6, pp. 2557–2566, 2013.
- [27] J. Meng, M. Ricco, G. Luo, M. Swierczynski, D.-I. Stroe, A.-I. Stroe, and R. Teodorescu, "An overview and comparison of online implementable soc estimation methods for lithium-ion battery," *IEEE Trans. Ind. Appl.*, vol. 54, no. 2, pp. 1583–1591, Mar. 2018.
- [28] M. Doyle, J. Newman, A. S. Gozdz, C. N. Schmutz, and J.-M. Tarascon, "Comparison of modeling predictions with experimental data from plastic lithium ion cells," *Journal of the Electrochemical Society*, vol. 143, no. 6, p. 1890, 1996.
- [29] J. Meng, G. Luo, M. Ricco, M. Swierczynski, D.-I. Stroe, and R. Teodorescu, "Overview of lithium-ion battery modeling methods for state-of-charge estimation in electrical vehicles," *Applied sciences*, vol. 8, no. 5, p. 659, 2018.
- [30] J. Du, Z. Liu, and Y. Wang, "State of charge estimation for li-ion battery based on model from extreme learning machine," *Control Engineering Practice*, vol. 26, pp. 11–19, 2014.
- [31] C. Albright, "Battery management system," Tech. Rep., 1993.
- [32] Y. Wang, J. Tian, Z. Sun, L. Wang, R. Xu, M. Li, and Z. Chen, "A comprehensive review of battery modeling and state estimation approaches for advanced battery management systems," *Renewable and Sustainable Energy Reviews*, vol. 131, p. 110015, 2020.
- [33] L. Lu, X. Han, J. Li, J. Hua, and M. Ouyang, "A review on the key issues for lithium-ion battery management in electric vehicles," *Journal of power sources*, vol. 226, pp. 272–288, 2013.

- [34] M. Lelie, T. Braun, M. Knips, H. Nordmann, F. Ringbeck, H. Zappen, and D. U. Sauer, “Battery management system hardware concepts: an overview,” *Applied Sciences*, vol. 8, no. 4, p. 534, 2018.
- [35] L. Pei, T. Wang, R. Lu, and C. Zhu, “Development of a voltage relaxation model for rapid open-circuit voltage prediction in lithium-ion batteries,” *J. Power Sources.*, vol. 253, pp. 412–418, May 2014.
- [36] P. Shen, M. Ouyang, L. Lu, J. Li, and X. Feng, “The co-estimation of state of charge, state of health, and state of function for lithium-ion batteries in electric vehicles,” *IEEE Trans. Veh. Technol.*, vol. 67, no. 1, pp. 92–103, Jan. 2018.
- [37] L. Y. Wang, M. P. Polis, G. G. Yin, W. Chen, Y. Fu, and C. C. Mi, “Battery cell identification and soc estimation using string terminal voltage measurements,” *IEEE Trans. Veh. Technol.*, vol. 61, no. 7, pp. 2925–2935, Sept. 2012.
- [38] G. Giordano, V. Klass, M. Behm, G. Lindbergh, and J. Sjöberg, “Model-based lithium-ion battery resistance estimation from electric vehicle operating data,” *IEEE Trans. Veh. Technol.*, vol. 67, no. 5, pp. 3720–3728, May 2018.
- [39] R. Xiong, H. He, F. Sun, and K. Zhao, “Evaluation on state of charge estimation of batteries with adaptive extended kalman filter by experiment approach,” *IEEE Trans. Veh. Technol.*, vol. 62, no. 1, pp. 108–117, Jan. 2013.
- [40] R. Xiong, J. Tian, W. Shen, and F. Sun, “A novel fractional order model for state of charge estimation in lithium ion batteries,” *IEEE Trans. Veh. Technol.*, vol. 68, no. 5, pp. 4130–4139, May 2019.
- [41] X. Chen, W. Shen, M. Dai, Z. Cao, J. Jin, and A. Kapoor, “Robust adaptive sliding-mode observer using rbf neural network for lithium-ion battery state of charge estimation in electric vehicles,” *IEEE Trans. Veh. Technol.*, vol. 65, no. 4, pp. 1936–1947, Apr. 2016.

- [42] J. Xu, C. C. Mi, B. Cao, J. Deng, Z. Chen, and S. Li, "The state of charge estimation of lithium-ion batteries based on a proportional-integral observer," *IEEE Trans. Veh. Technol.*, vol. 63, no. 4, pp. 1614–1621, May 2014.
- [43] J. Meng, D.-I. Stroe, M. Ricco, G. Luo, and R. Teodorescu, "A simplified model-based state-of-charge estimation approach for lithium-ion battery with dynamic linear model," *IEEE Trans. Ind. Electron.*, vol. 66, no. 10, pp. 7717–7727, Oct. 2019.
- [44] E. Chemali, P. J. Kollmeyer, M. Preindl, R. Ahmed, and A. Emadi, "Long short-term memory networks for accurate state-of-charge estimation of li-ion batteries," *IEEE Trans. Ind. Electron.*, vol. 65, no. 8, pp. 6730–6739, Aug. 2018.
- [45] W. Yan, B. Zhang, G. Zhao, S. Tang, G. Niu, and X. Wang, "A battery management system with a lebesgue-sampling-based extended kalman filter," *IEEE Trans. Ind. Electron.*, vol. 66, no. 4, pp. 3227–3236, Apr. 2019.
- [46] J. Chen, Q. Ouyang, C. Xu, and H. Su, "Neural network-based state of charge observer design for lithium-ion batteries," *IEEE Trans. Control Syst. Technol.*, vol. 26, no. 1, pp. 313–320, Jan. 2018.
- [47] K. S. Ng, C.-S. Moo, Y.-P. Chen, and Y.-C. Hsieh, "Enhanced coulomb counting method for estimating state-of-charge and state-of-health of lithium-ion batteries," *Appl. Energy*, vol. 86, no. 9, pp. 1506–1511, Sept. 2009.
- [48] M. Cacciato, G. Nobile, G. Scarcella, and G. Scelba, "Real-time model-based estimation of SOC and SOH for energy storage systems," *IEEE Trans. Power Electron.*, vol. 32, no. 1, pp. 794–803, Jan. 2017.
- [49] W. Wang, X. Wang, C. Xiang, C. Wei, and Y. Zhao, "Unscented kalman filter-based battery soc estimation and peak power prediction method for power

- distribution of hybrid electric vehicles,” *IEEE Access*, vol. 6, pp. 35 957–35 965, 2018.
- [50] Y. Wang, C. Zhang, and Z. Chen, “A method for state-of-charge estimation of LiFePO_4 batteries at dynamic currents and temperatures using particle filter,” *J. Power Sources*, vol. 279, pp. 306–311, Apr. 2015.
- [51] C. Chen, R. Xiong, and W. Shen, “A lithium-ion battery-in-the-loop approach to test and validate multiscale dual H infinity filters for state-of-charge and capacity estimation,” *IEEE Trans. Power Electron.*, vol. 33, no. 1, pp. 332–342, Jan. 2018.
- [52] M. Petzl and M. A. Danzer, “Advancements in OCV measurement and analysis for lithium-ion batteries,” *IEEE Trans. Energy Convers.*, vol. 28, no. 3, pp. 675–681, Sept. 2013.
- [53] A. Farmann and D. U. Sauer, “A study on the dependency of the open-circuit voltage on temperature and actual aging state of lithium-ion batteries,” *J. Power Sources.*, vol. 347, pp. 1–13, Apr. 2017.
- [54] L. Pei, R. Lu, and C. Zhu, “Relaxation model of the open-circuit voltage for state-of-charge estimation in lithium-ion batteries,” *IET Elect. Syst. Transp.*, vol. 3, no. 4, pp. 112–117, Dec. 2013.
- [55] C. Birkl, E. McTurk, M. Roberts, P. Bruce, and D. Howey, “A parametric open circuit voltage model for lithium ion batteries,” *J. Electrochem. Soc.*, vol. 162, no. 12, pp. A2271–A2280, 2015.
- [56] A. Li, S. Pelissier, P. Venet, and P. Gyan, “Fast characterization method for modeling battery relaxation voltage,” *Batteries*, vol. 2, no. 2, p. 7, 2016.
- [57] J. Meng, D.-I. Stroe, M. Ricco, G. Luo, M. Swierczynski, and R. Teodorescu, “A novel multiple correction approach for fast open circuit voltage prediction of

- lithium-ion battery,” *IEEE Trans. Energy Convers.*, vol. 34, no. 2, pp. 1115–1123, Jun. 2019.
- [58] J. Yang, W. Huang, B. Xia, and C. Mi, “The improved open-circuit voltage characterization test using active polarization voltage reduction method,” *Appl. Energy*, vol. 237, pp. 682–694, Mar. 2019.
- [59] F. Baronti, N. Femia, R. Saletti, C. Visone, and W. Zamboni, “Hysteresis modeling in li-ion batteries,” *IEEE Trans. Magn.*, vol. 50, no. 11, pp. 1–4, Nov. 2014.
- [60] H. Zhang, H. W. Mu, Y. Zhang, and J. Han, “Calculation and characteristics analysis of lithium ion batteries’ internal resistance using hppc test,” in *Advanced Materials Research*, vol. 926. Trans Tech Publ, 2014, pp. 915–918.
- [61] E. Samadani, S. Farhad, W. Scott, M. Mastali, L. E. Gimenez, M. Fowler, and R. A. Fraser, “Empirical modeling of lithium-ion batteries based on electrochemical impedance spectroscopy tests,” *Electrochimica acta*, vol. 160, pp. 169–177, 2015.
- [62] M. Kwiecien, J. Badedda, M. Huck, K. Komut, D. Duman, and D. U. Sauer, “Determination of soh of lead-acid batteries by electrochemical impedance spectroscopy,” *Applied Sciences*, vol. 8, no. 6, p. 873, 2018.
- [63] E. Din, C. Schaef, K. Moffat, and J. T. Stauth, “A scalable active battery management system with embedded real-time electrochemical impedance spectroscopy,” *IEEE Transactions on Power Electronics*, vol. 32, no. 7, pp. 5688–5698, 2016.
- [64] H. Dai, B. Jiang, and X. Wei, “Impedance characterization and modeling of lithium-ion batteries considering the internal temperature gradient,” *Energies*, vol. 11, no. 1, p. 220, 2018.
- [65] T. N. Gücin and L. Ovacik, “Online impedance measurement of batteries using the cross-correlation technique,” *IEEE Transactions on Power Electronics*, 2019.

- [66] Z. Xia and J. A. A. Qahouq, "Method for online battery ac impedance spectrum measurement using dc-dc power converter duty-cycle control," in *2017 IEEE Applied Power Electronics Conference and Exposition (APEC)*. IEEE, 2017, pp. 1999–2003.
- [67] K. Uddin, A. D. Moore, A. Barai, and J. Marco, "The effects of high frequency current ripple on electric vehicle battery performance," *Applied energy*, vol. 178, pp. 142–154, 2016.
- [68] K. Hwu and Y. Yau, "A ky boost converter," *IEEE Transactions on Power Electronics*, vol. 25, no. 11, pp. 2699–2703, 2010.
- [69] L. Zhao and J. Qian, "Dc-dc power conversions and system design considerations for battery operated system," *Texas Instruments*, 2006.
- [70] Y. Cao, H. Yang, T. Gao, S. Shao, and B. Zhang, "Switched-mode control of battery backup unit in data center for online impedance detection," in *2020 IEEE Applied Power Electronics Conference and Exposition (APEC)*, 2020, pp. 3332–3336.
- [71] S. R. Islam and S.-Y. Park, "Precise on-line electrochemical impedance spectroscopy strategies for li-ion batteries," *IEEE Transactions on Industry Applications*, 2019.
- [72] A. Kopczyński, Z. Liu, and P. Krawczyk, "Parametric analysis of li-ion battery based on laboratory tests," in *E3S Web of Conferences*, vol. 44. EDP Sciences, 2018, p. 00074.
- [73] D. Czarkowski and M. K. Kazimierczuk, "Energy-conservation approach to modeling pwm dc-dc converters," *IEEE Transactions on Aerospace and Electronic systems*, vol. 29, no. 3, pp. 1059–1063, 1993.

- [74] J. Sihvo, D.-I. Stroe, T. Messo, and T. Roinila, “Fast approach for battery impedance identification using pseudo-random sequence signals,” *IEEE Transactions on Power Electronics*, vol. 35, no. 3, pp. 2548–2557, 2019.
- [75] S. Golestan, M. Ramezani, J. M. Guerrero, F. D. Freijedo, and M. Monfared, “Moving average filter based phase-locked loops: Performance analysis and design guidelines,” *IEEE Transactions on Power Electronics*, vol. 29, no. 6, pp. 2750–2763, 2013.
- [76] B. Ratnakumar, M. Smart, L. Whitcanack, and R. Ewell, “The impedance characteristics of mars exploration rover li-ion batteries,” *Journal of power sources*, vol. 159, no. 2, pp. 1428–1439, 2006.
- [77] A. A. Hussein and A. A. Chehade, “Robust artificial neural network-based models for accurate surface temperature estimation of batteries,” *IEEE Transactions on Industry Applications*, vol. 56, no. 5, pp. 5269–5278, 2020.
- [78] C. G. Moral, D. Fernandez, J. M. Guerrero, D. Reigosa, C. Riva, and F. Briz, “Thermal monitoring of lifepo4 batteries using switching harmonics,” *IEEE Transactions on Industry Applications*, 2020.
- [79] R. R. Richardson and D. A. Howey, “Sensorless battery internal temperature estimation using a kalman filter with impedance measurement,” *IEEE Transactions on Sustainable Energy*, vol. 6, no. 4, pp. 1190–1199, 2015.
- [80] R. Schwarz, K. Semmler, M. Wenger, V. R. Lorentz, and M. März, “Sensorless battery cell temperature estimation circuit for enhanced safety in battery systems,” in *IECON 2015-41st Annual Conference of the IEEE Industrial Electronics Society*. IEEE, 2015, pp. 001 536–001 541.
- [81] D. Bernardi, E. Pawlikowski, and J. Newman, “A general energy balance for battery systems,” *Journal of the electrochemical society*, vol. 132, no. 1, p. 5, 1985.

- [82] J. Chung, C. Gulcehre, K. Cho, and Y. Bengio, “Empirical evaluation of gated recurrent neural networks on sequence modeling,” *arXiv preprint arXiv:1412.3555*, 2014.
- [83] D. E. Rumelhart, G. E. Hinton, and R. J. Williams, “Learning representations by back-propagating errors,” *nature*, vol. 323, no. 6088, pp. 533–536, 1986.
- [84] W. He, N. Williard, C. Chen, and M. Pecht, “State of charge estimation for li-ion batteries using neural network modeling and unscented kalman filter-based error cancellation,” *International Journal of Electrical Power & Energy Systems*, vol. 62, pp. 783–791, 2014.
- [85] J. Chiasson and B. Vairamohan, “Estimating the state of charge of a battery,” in *Proceedings of the 2003 American Control Conference, 2003.*, vol. 4. IEEE, 2003, pp. 2863–2868.
- [86] K.-S. Ng, C.-S. Moo, Y.-P. Chen, and Y.-C. Hsieh, “State-of-charge estimation for lead-acid batteries based on dynamic open-circuit voltage,” in *2008 IEEE 2nd International Power and Energy Conference*. IEEE, 2008, pp. 972–976.
- [87] J. Meng, G. Luo, and F. Gao, “Lithium polymer battery state-of-charge estimation based on adaptive unscented kalman filter and support vector machine,” *IEEE Transactions on Power Electronics*, vol. 31, no. 3, pp. 2226–2238, 2015.
- [88] H. He, R. Xiong, and J. Peng, “Real-time estimation of battery state-of-charge with unscented kalman filter and rtos μ cos-ii platform,” *Applied energy*, vol. 162, pp. 1410–1418, 2016.
- [89] J. C. A. Anton, P. J. G. Nieto, C. B. Viejo, and J. A. V. Vilan, “Support vector machines used to estimate the battery state of charge,” *IEEE Transactions on power electronics*, vol. 28, no. 12, pp. 5919–5926, 2013.

- [90] Y. Tian, R. Lai, X. Li, L. Xiang, and J. Tian, "A combined method for state-of-charge estimation for lithium-ion batteries using a long short-term memory network and an adaptive cubature kalman filter," *Applied Energy*, vol. 265, p. 114789, 2020.
- [91] J. Yang, B. Xia, Y. Shang, W. Huang, and C. C. Mi, "Adaptive state-of-charge estimation based on a split battery model for electric vehicle applications," *IEEE Trans. Veh. Technol.*, vol. 66, no. 12, pp. 10 889–10 898, Dec. 2017.
- [92] C. Bian, H. He, and S. Yang, "Stacked bidirectional long short-term memory networks for state-of-charge estimation of lithium-ion batteries," *Energy*, vol. 191, p. 116538, 2020.
- [93] J. C. Á. Antón, P. J. G. Nieto, F. J. de Cos Juez, F. S. S. Lasheras, C. B. Viejo, and N. R. Gutiérrez, "Battery state-of-charge estimator using the mars technique," *IEEE Transactions on Power Electronics*, vol. 28, no. 8, pp. 3798–3805, 2012.
- [94] E. Chemali, P. J. Kollmeyer, M. Preindl, R. Ahmed, and A. Emadi, "Long short-term memory networks for accurate state-of-charge estimation of li-ion batteries," *IEEE Transactions on Industrial Electronics*, vol. 65, no. 8, pp. 6730–6739, 2018.
- [95] F. Zhao, Y. Li, X. Wang, L. Bai, and T. Liu, "Lithium-ion batteries state of charge prediction of electric vehicles using rnns-cnns neural networks," *IEEE Access*, vol. 8, pp. 98 168–98 180, 2020.
- [96] R. Zhao, P. J. Kollmeyer, R. D. Lorenz, and T. M. Jahns, "A compact methodology via a recurrent neural network for accurate equivalent circuit type modeling of lithium-ion batteries," *IEEE Transactions on Industry Applications*, vol. 55, no. 2, pp. 1922–1931, 2019.

- [97] Y. Bengio, P. Simard, and P. Frasconi, “Learning long-term dependencies with gradient descent is difficult,” *IEEE transactions on neural networks*, vol. 5, no. 2, pp. 157–166, 1994.
- [98] F. Yang, S. Zhang, W. Li, and Q. Miao, “State-of-charge estimation of lithium-ion batteries using lstm and ukf,” *Energy*, vol. 201, p. 117664, 2020.
- [99] H. Soltau, H. Liao, and H. Sak, “Neural speech recognizer: Acoustic-to-word lstm model for large vocabulary speech recognition,” *arXiv preprint arXiv:1610.09975*, 2016.
- [100] D. E. Rumelhart, P. Smolensky, J. L. McClelland, and G. Hinton, “Sequential thought processes in pdp models,” *Parallel distributed processing: explorations in the microstructures of cognition*, vol. 2, pp. 3–57, 1986.
- [101] S. Hochreiter and J. Schmidhuber, “Long short-term memory,” *Neural computation*, vol. 9, no. 8, pp. 1735–1780, 1997.
- [102] A. Graves, N. Jaitly, and A.-r. Mohamed, “Hybrid speech recognition with deep bidirectional lstm,” in *2013 IEEE workshop on automatic speech recognition and understanding*. IEEE, 2013, pp. 273–278.